PREDICTIVE MODELING FOR MATERIAL MICROSTRUCTURE AFFECTED MACHINING

A Dissertation
Presented to
The Academic Faculty

by

Zhipeng Pan

In Partial Fulfillment
of the Requirements for the Degree
Doctor of Philosophy in the
George W. Woodruff School of Mechanical Engineering

Georgia Institute of Technology
May 2018

PREDICTIVE MODELING FOR MATERIAL MICROSTRUCTURE AFFECTED MACHINING

Approved by:

Dr. Steven Y. Liang, Advisor
School of Mechanical Engineering
Georgia Institute of Technology

Dr. Hamid Garmestani
School of Materials Science and Engineering
Georgia Institute of Technology

Dr. Thomas Kurfess
School of Mechanical Engineering
Georgia Institute of Technology

Dr. Donald S. Shih
Kumamoto University

Dr. Christopher Saldana
School of Mechanical Engineering
Georgia Institute of Technology

Date Approved: January 26, 2018

ACKNOWLEDGEMENTS

Firstly, I would like to thank my advisor, Professor Steven Y. Liang. It has been a great honor to work in his Precision Machining Research Consortium (PMRC) as a PhD student. He taught me how to do both fundamental scientific research and application orientated project. I really appreciate all his time, funding and expertise to make my PhD research so productive. His enthusiasm and dedication for research has been the best motivation for me during my PhD. His wide expertise in manufacturing and in-depth understanding for advanced manufacturing process modeling set up as the best role model for both my PhD study and future career development. He showed me strong dedication and readiness for academic research and student supervising.

I also want to thank my committee member Prof. Thomas Kurfess, Prof. Christopher J. Saldana, Prof. Hamid Garmestani and Prof. Donald S. Shih. The kind suggestions and generous idea helped me a lot in working on the thesis. Their insight and general knowledge greatly improved the quality of my research work.

In addition, I want to thank my colleagues, Dr. Yamin Shao, Dr. Manik Rojora, Yanfei Lu, Yixuan Feng, Dr. Haibo Liu, Dr. Caixue Yue, Dr. Xiaohong Lu, for their kind help. I enjoyed a great time working with them at Georgia Tech. I also would like to thank all the members in the PMRC. Specially, I want to thank Dr. Tsungpin Hung, Fuchuan Hsu to their kind experimental support from the Metal Industries Research & Development Centre.

Last but not least, I want to thank my wife Chong, my parents, and brother, for their continuous support and encouragement during my study.

CONTENTS

LIST OF TABLES

LIST OF FIGURES

SUMMARY

The precision machining has long been focused on the machined part geometrical consideration, such as dimensional accuracy and surface roughness. The machined part dimensional accuracy is strongly influenced by the tool wear and tool deflection. The surface roughness is a function of process parameters, such as cutting speed, feed rate, and tool geometry (edge radius, rake angle). With the rapid development of precision machining technology, the manufacturing end-product functionality requires the precision machining capability beyond machined part geometrical properties. Other aspects of the machining end-product, including the surface physical properties, metallurgical, chemical and biological characterizations are also part of the precision machining requirement. The surface residual stress profile could significantly influence the workpiece fatigue life and corrosion resistance. In additional to the mechanical states, the material microstructure attributes are closely related to the surface functionalities. For example, the surface micro-hardness is dominated by the grain size and phase composition for multiphase material. Other microstructure properties of the machined surface include the plastic deformation induced dislocation density, phase transformation, micro-cracks and inter-granular attack. To fully describe the precision machining process, the microstructure consideration is required. Compared with the traditional framework which only includes the thermal and mechanical considerations, the microstructure-based machining process model could provide a more in-depth understanding of the mechanical, thermal and microstructural interactions.

The microstructure consideration in the machining process covers phase transformation, dynamic recrystallization, grain morphology and dislocation density. The material microstructure evolution in the machining process is a combined effect from the thermal-mechanical interactions.

For example, the phase transformation is dependent on the temperature history, grain growth is determined by the strain, strain rate and temperature effect. In addition, the material microstructure properties would inversely affect the material mechanical properties and heat generation in the machining processes. Therefore, a thermal-mechanical-microstructural coupled framework would be more desirable for the machining process description. The material microstructure evolution in the machining process could be lead to the undesirable direction, such as increased grain size on the machined surface, or undesirable phase transformation effect. To avoid this, a comprehensive machining process design process would be required, which takes the machining process parameters, machine tool configuration and workpiece material properties into consideration. The current work aims to bring out a computational framework to assist the machining process design and optimization, which outputs the machined end-product microstructure states related surface integrity properties. The model would need a material microstructure structural evolution model, explicit correlation of the material mechanical properties with material microstructural states. This thesis, for the first time, concludes from the current state of the art research in machining with a consideration of the material microstructure properties, brings out the material microstructure affected machining framework.

Alternatively, the precision machining also includes the precise control the machined part dimensional accuracy, improved residual stress states and machined parts surface integrity. For the hard to machine material, especially Nickle based super alloy, advanced machining process would be required to solve the state of art challenges. An advanced thermal enhanced machining system is developed with improved machining efficiency and reduce energy cost. A novel co-axial laser-assisted milling system is developed, specifically for the hard-to-machine material with high

energy efficiency and large material removal rate. A comprehensive numerical based laser-assisted milling model is proposed for the process simulation and optimization.

NOMENCLATURE

α_i, h_i, m_i, c_i, n_i, k_d, β_d,	Johnson-Mehl-Avrami-Kolmogorov dynamic recrystallization model coefficients
A, B, n, C, m	Johnson-Cook material flow stress model coefficient
T_m	Material melting temperature
T_0	Reference temperature
Q_{act}	Activation energy
X_{drex}	Dynamic recrystallized volume fraction
d_0	Initial average grain size
d_{drex}	Recrystallized average grain size
d	Average grain size
V	Cutting speed
f	Feed rate
ϑ_v	Volume fraction of α to β transformation
T_0	Reference temperature
A_S, T_S, D_S	Material coefficient of Avrami mode for to transformation
ξ	Volume fraction of β to $\alpha + \beta$ transformation
σ_α, σ_β, σ	Flow stress of the α phase, β phase and the norminal flow stress
η	Volume fraction of α phase
τ	Shear force between the cutting tool and workpiece material
σ_n	Normal stress on the tool/workpiece interface
σ_1	Maximum principle stress

ε_f	Effective strain
D_f	Fracture coefficient in Cockroft and Latham's model
A_{hp} and K_{hp}	Hall-Petch parameters
AB	Length of the shear plane
ϕ	Shear angle
t	Undeformed chip thickness
α_r	Rake angle
V_S	Shear velocity
V_C	Chip flow velocity
ε_{AB}	Strain on the shear plane
$\dot{\varepsilon}_{AB}$	Strain rate on the shear plane
C_{Oxley}	Oxley's constant
T_{AB}	Temperature on the AB shear plane
η_p	Plastic energy to heat conversion ratio
ρ	Density
h	Conductivity
h_c	Tool chip contact length
w	Width of cut
ΔT	Temperature rise
C_P	Heat capacity
k_{AB}	Flow stress in the AB shear plane
λ	Friction angle
θ	Inclination angle
C_n	Modified Oxley's constant
h	Tool chip contact length
τ_{int}	Shear stress
F	Shear force

T_{int}	Temperature on tool chip interface
$\dot{\varepsilon}_{\text{int}}$	Average strain rate on the chip
F_C, F_t, F_P	Machining force in cutting, thrusting, ploughing direction
C_S*	Side cutting angle
t*	Equivalent depth of cut in 3D turning
W*	Equivalent width of cut in 3D turning
P_1, P_2, P_3	Force in the cutting, feed and axial direction in 3D turning
$\Delta T_{shear}(x,z)$	Temperature rise on workpiece from the heat source in shear zone
k	Thermal conductivity
K_0	Modified second Bessel function
$\Delta T_{rub}(x,z)$	Temperature rise on workpiece from heat source on the rubbing zone
γ	Heat partition coefficient
$F_X(\psi)$, $F_Y(\psi)$, $F_Z(\psi)$	Force in the x-, y-, and z- direction at the rotational angle of ψ
ω	Angular rotation speed

CHAPTER 1. INTRODUCTION

1.1 Motivation

The development of high precision machining technology enables the complicated shape control, high geometrical accuracy and good surface integrity of the end-product. The geometrical shape control is achieved by the precise machine tool path planning and error compensation. Appropriate design of the final workpiece material mechanical and microstructural property is required for good surface integrity. The machining process conditions could significantly influence the resultant surface integrity of the final workpiece material. The service functionality of the precision machining end-product strongly depends on workpiece material properties. The main consideration in terms of the final workpiece properties includes mechanical attributes (residual stress profile, yield stress, surface hardness), microstructure states (grain structure and orientation, phase composition). The workpiece material properties in the machining process are directly influenced by the process conditions.

Appropriate selection of the machining parameters could help to improve the functionality performance of the end product [1]. For the hard to machine material, such as titanium, nickel based alloys and hardened steels, the high precision machining still faces considerable challenges [2]. Significant microstructural evolution has been observed in the machining process [3-5]. The material mechanical properties are strongly dependent on the microstructural states. Also, workpiece surface corrosion resistance, microhardness is also influenced by the microstructural attributes. The machining induced residual stress profile is a critical factor for the workpiece corrosion resistance. For biomedical or aerospace industry, the grain refinement would be desirable for the strengthening.

The thermo-mechanical loading introduced from high speed machining will unfavorably affect the workpiece material properties, such as augmented grain size, reduced surface hardness, and tensile residual stress profile [6]. Most of the current research work only focuses on the thermo-mechanical coupling process, where the microstructural evolution effect is largely ignored. However, obvious microstructural change has been observed in the machining process, especially for multiphase material, such as titanium alloys and nickel-based alloys. Therefore, it is important to understand the thermo-mechanical-microstructural coupling effects.

The combined effect of server plastic deformation, large strain, high strain rate and high temperature in the primary shear zone and workpiece/tool interface would promote the microstructure evolution such as dislocation density change, grain size evolution and multiphase material phase transformation. The early work on the microstructure change in the machining process is reported by Xu et al. [7] in the grinding of ceramics. The different material microstructure effect on the material removal mechanism is investigated. The white layer is observed in the hard turning of hardened steel by Chou et al. [8], which results from workpiece material phase transformation effect. Similarly, the extensive grain refinement and strain induced martensite phase transformation is observed by Ghosh et al. [4] in surfaced turning of 304L stainless steel. The grain refinement and uniform nanocrystalline structure also is found in the chip in turning of copper by Swaminathan et al. [9]. The investigation of machining induced microstructure change would not only benefit the machining process optimization to achieve machining end-product with good service functionality, the machining tool selection and improvement could also be obtained. However, the microstructural level investigation of machining is still at its debut stage, where most of the research focuses on the experimental investigation.

Different advanced machining processes, such as thermal-assisted machining, acoustic-assisted machining, have been proposed to achieve high machining efficiency, improved machining end-product quality. Due to the complicated thermal-mechanical coupling effects, the current modeling techniques have not been well developed to fully address the challenges. Only some simple empirical models are proposed by previous researchers. In a current study, a more energy efficient co-axial laser assisted milling setup is developed to locally heat the working piece material in the milling process. A two-step modeling is proposed for the laser-assisted milling process simulation.

1.2 Research Goal and Objectives

A physical based modeling scheme for the residual stress, machining forces and microstructural states will be developed. The flow chart of the proposed research method is shown in Fig. 1. The material microstructural affected machining inputs the process parameters, machining tool configuration and material initial mechanical microstructural properties into a well-defined process function path. The machining forces and temperature field are the output in the first step, which was calculated by the classic contact mechanics theory. In the second step, the thermo-mechanical loading condition from the previous step are taken into the microstructural evolution loop. The phase transformation is purely based on the temperature loading history. However, the dynamical recrystallization process is a strong function of strain, strain rate, temperature. After the explicit calculation of the microstructure attributes, the material flow stress is updated back into step one. An interactive process is conducted. Finally, the residual stress, material microhardness, machining forces are the prediction outcomes.

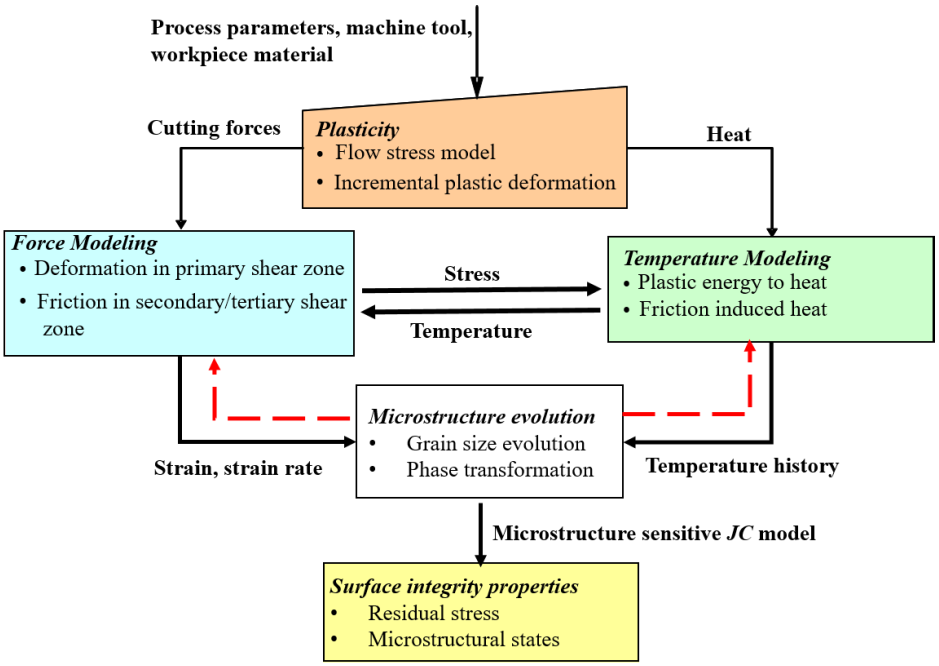

Figure 1 Material microstructural affect machining modeling scheme

1.3 Overview of Thesis

The thesis consists of five parts. In the chapter 2, literature review part, we would give a comprehensive review work on the state of art research on the material microstructure related machining process modeling work. Mainly two different material will be reviewed, the *Ti-6Al-4V* and the Inconel 718. In the chapter 3, a material dynamic recrystallization model and phase transformation model will be introduced for the multiphase material. A case study will be conducted on the orthogonal turning of *Ti-6Al-4V* for the grain size evolution and phase change prediction. In chapter 4, a thermal-mechanical-microstructure coupled machining process modeling framework will be developed for application the machining force and residual stress calculation. The microstructure sensitive flow stress model will be developed. In chapter 5, as an extension of the traditional machining process, a novel co-axial laser-assisted milling setup is developed to machine the hard to machine material. An FEA (finite element analysis) model is developed for the temperature field and heat-affected zone prediction in the laser-assisted

machining process. At the second section of the chapter 5, the analytical machining force prediction model is proposed for the milling force prediction in the laser-assisted milling process.

CHAPTER 2. LITERATURE REVIEW

2.1 Machining induced microstructure evolution

In the manufacturing processes, such as hot forging, laser assisted melting and friction stir welding, the material microstructure would typically have considerable change due to the high-temperature effect [10-12]. With the development of high speed machining equipment, the increased cutting speed could elevate the machining temperature where material microstructure is unstable. In a traditional manufacturing process, the material microstructural evolution path is mainly dependent on the temperature history. In the machining process, the server plastic deformation (large strain, high strain rate) could also help to promote the material microstructure evolution. The material microstructure evolution mainly occurs in the primary shear zone and machined workpiece surface.

The microstructure changes on the machined surface typically manifest as the white layer. In the machining process, the generation of white layer mainly attributes to the two mechanisms: the phase transformation from rapid heating and quenching, the homogenous structure or ultrafine grain structure from the server plastic deformation. A list of some selected research work on the white layer is shown in Table 1. The white layer in the hard turning of AISI 52100 steel alloys has been reported by the Chou et al. [8]. In the white layer, improved material microhardness is observed due to possible strain hardening effect. In the laser assisted milling of Al 2024 alloy, up to around 5 μm thick heat-affected-zone layer is observed, where a-liquid phases are generated [13], shown in Fig. 2. High residual stress concentration and reduced fatigue life on the heat affected zone are observed. In the high speed hard turning of hardened steels with ceramic cutting tool, refined grain structure and white layer is observed on the machined surface up to 2 μm depth

into the workpiece. Compared with the ceramic cutting insert, less significant microstructure alteration is found when machining with PCBN tool, as reported by EI-Wardany et al. [14]. The micromachining, the material microstructure has strong influence on the end product qualify. The roughness of the machining surface is dominated by surface layer grain size. More than three times better surface roughness was reported by Popov et al. [15] in the milling of ultra-fine grain aluminum. In the high speed milling of AISI H12 steel, significant microstructure and microhardness changes are found [16]. Also, the effect of different milling conditions on the microstructure are investigated, as shown in Fig. 3. Extensive grain refinement and strain induced martensitic phase transformation near the machined surface in finish turning of 304L steel are reported by Ghosh et al. [4], as shown in Fig. 4. The work hardened layer on the surface could help to increase the susceptibility to stress corrosion crack of the machined surface.

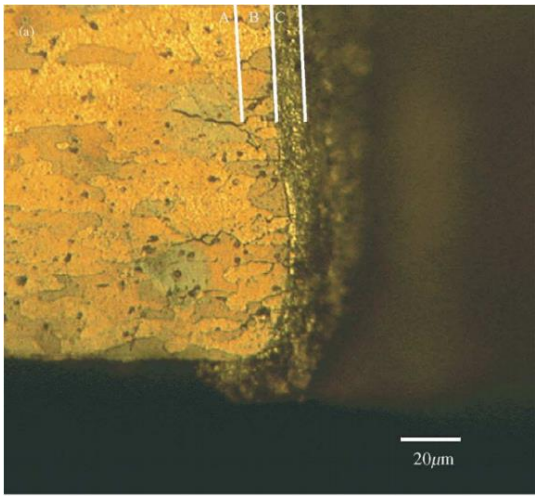

Figure 2 The heat affected zone of the aluminum alloy after the laser assisted milling process, where *A* is the unaffected area, *B* indicates the elongated grain structure region, C shows the refined α-grain structure [13].

Table 1 Previous research on white layer formation in machining

Material	Process	References	Comments
EN8 steel	Drilling	Griffiths [17]	Catastrophic wear and rubbing induce white layer formation.
AISI 1045 steel	Turning	Han et al. [18]	Plastic deformation promotes phase transformation at lower temperature.
AISI 52100 steel	Turning	Barbacki et al. [19]	
		Ramesh et al. [20]	Prediction model for plasticity induced martensitic phase transformation.
		Umbrello et al. [21]	The white layer thickness increases with increasing feed rate.
		Poulachon et al. [22]	The white layer thickness increases with the tool flank wear.
		Duan et al. [23]	Temperature based FEA model for white layer thickness prediction.
BS 817M40 steel	Turning	Barry et al. [24]	Refined grain size from the material recrystallization.
H13 steel	Turning	Bosheh et al. [25]	The martensitic phase transformation is correlated with tool wear.
Ti-6Al-4V	Turning	Che-Haron et al. [26]	Working hardening is observed on the white layer.
		Velásqueza et al. [27]	Plastically affected zone observed, but no phase transformation.
	End milling	Daymi et al. [28]	Thin plastically deformed layer.
Inconel 100	Turning	Ranganath et al. [29]	FEA prediction model for the white layer and bent grains

(a) (b)

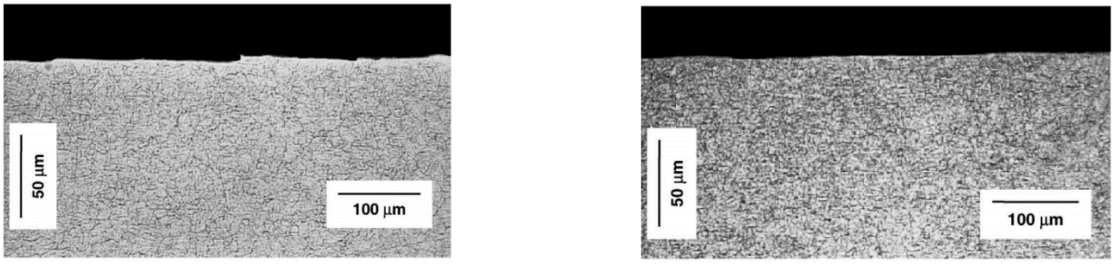

Figure 3 The microstructure of the AISI H13 steel of the machined workpiece at cutting speed of 300 *m/min*, feed rate = 0.1 *mm/tooth*, axial depth of cut = 0.2 *mm* , (a) at cutting direction of 0^o (b) cutting direction of 60^o [16].

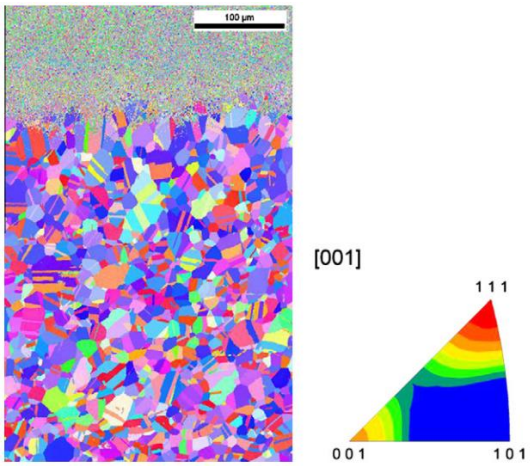

Figure 4 EBSD image showing around 150 μm thick layer grain refinement (less than 0.5 μm) in the machined surface [4].

Besides the observation on the white layer formation purely from experimental study, both empirical and physical based models have been proposed to predict the white layer generation after machining. A finite element based model is developed by Ranganth et al. [29] to calculate the plastic strain, which is believed to be the cause of white layer generation on the machined surface of Inconel 100 alloy. The temperature effect on the white layer generation is largely ignored. Duan et al. [23] argued that, the phase transformation is the dominating factor in white layer generation.

A pure temperature-based phase transformation model is used for the white layer thickness prediction. Ramesh et al. [20] developed a model that incorporates the strain, stress and temperature effect on the white layer generation. Similar research is done by Han et al. [18] in turning of AISI 1045 steel. From a more physics based ground, an analytical model is proposed by Chou et al. [30] to calculate the white layer thickness in the orthogonal turning of hardened steel. More specifically, Umbrello et al. [31] called the phase transformation layer as the dark layer on the machining surface of AISI 51200 steel. A FEA model is developed for the prediction of both white layer and dark layer on the machined surface.

The shear zone, where large plastic deformation occurs, typically there would be considerable microstructure change. Another factor that influences the microstructure change in the primary shear zone is the high temperature condition. Different from the tool workpiece interface, where the heat is generated mainly from the friction effect, the plastic energy to heat transformation in the shear zone is the dominating factor. Another characteristic of the shear zone is the large strain and high strain rate. A list of some representative previous research work on the material microstructure change in the shear zone is provided in Table 2. Wan et al. [32] reported that, with the increasing cutting speed, the shear zone would go through deformed bands to transformed bands in the machining of titanium alloy. The Martensitic phase transformation from α phase is triggered by the high temperature, as shown in Fig. 5. Similar report is also provided by Shivpuri et al. [33]. The phase transformation is one of the dominating factors that influence the chip morphology in the machining of multiphase material. Though extensive experimental studies have been conducted to investigate the phase transformation on chip formation, few prediction models have been developed. In the micro milling process, the workpiece material microstructure properties will strongly influence the minimum chip thickness and machined surface roughness,

as reported by Vogler et al. [34]. Interrupted chip formation occurs when the milling tool passes through the grain boundaries for multiphase materials.

Table 2 Related research work on the microstructure change in the shear zone

Material	References	Comments
Amour steel	Derep [35]	Phase transformation occurs in the adiabatic shear zone observed.
AISI 1045 steel	Duan et al. [36]	Plastic shear, reorientation and elongation of the martensitic laths.
Ti-6Al-4V	Shivpuri et al. [33]	Phase transformation occurs in the shear zone.
	Wan et al. [32]	Microstructure evolution in shear zone depends on cutting speed.
	Bayoumi et al. [37]	Non-diffusion phase transformation in shear localized chips.
	Velásquez et al. [38]	Deformation shear bands occurs, but no phase transformation observed.
	Ye et al. [39]	A momentum diffusion based-model is proposed to predict chip segmentation.
Al-7075	Campbell et al.[40]	Recrystallized equiaxed grains within the shear bands.
Al-6061-T6	Shankar et al. [41]	Refined grain of microstructure is found.

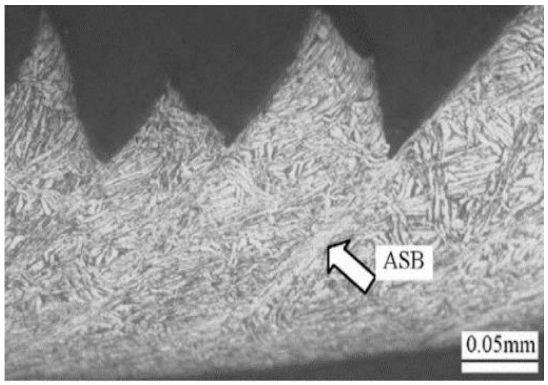

Figure 5 The martensitic transformation in the adiabatic shear bands (ASB) in turning of Ti-6Al-4V at rake angle of 10^o, cutting speed 30.2 *m/min*, depth of cut 0.3 *mm*, feed rate 0.21 *mm/rev* [32].

2.2 Microstructure effect on machining

2.2.1 Material microstructure effects on machining forces

The material microstructure variation could result in significant flow stress change. For the most of conventional machining process, the material could be treated as homogeneous where material microstructure variation is neglected. However, in the micromachining processes, the machining depth of cut could be smaller than the grain size of the material. Many materials, such as steels or titanium alloys do not exhibit good homogeneity at the microscale. The grain orientation of SiC whiskers with respect to the cutting directions would strongly influence the cutting force in the orthogonal turning process, as reported by Yuan et al. [42]. The cutting force also varies with the grain boundaries in the machining of aluminum alloys [43]. Chou et al. [44] reported increased tool life in the turning of fine microstructure steels compared with conventional steels. A microstructure based machining force prediction model is proposed by Chuzhoy et al. [45] to consider the different phase compositions in the turning of ductile irons. The smaller grain size of the material will result in both higher frequency and magnitude of the machining forces. Vogler et al. [46] also developed a statistic model to incorporate the microstructure consideration

in the micro-end milling of iron. With a grain size evolution consideration in the shear zone, a more accurate force prediction model is developed for the machining of *Ti-6Al-4V* material [47].

In the machining process, the machining force mainly comes from the plastic deformation stress in the primary shear zone, the friction stress between the tool and workpiece. In most cases, when the cutting tool nose radius is smaller enough compared with the depth of cut, the plastic deformation dominates. Server plastic deformation in the shear zone would generate considerable heat. Combined with the large strain, high strain rate, localized shear deformation would be generated. The adiabatic shear band is observed in the orthogonal turning of Ti-6Al-4V [48]. In the chip formation process of titanium alloys, the catastrophic adiabatic shear mechanism is proposed by Rechet [49] to described the segmented chip formation. From a physical ground, Xu et al. [50] discovered the phase transformation effect in the shear band which act as a softening mechanics for the crack propagation. Similar results are also reported in the machining of 340 stainless steel [51].

Since the material flow stress is a strong function of the material microstructure attributes, the material flow stress would have significant change in the machining processes, as shown in Fig. 6 [52]. The dominating microstructure factors on material flow stress include grain size, dislocation density and phase composition. Tremendous research has been dedicated to account for the microstructure evolution effect on the machining force. Most of the current research work focuses on the modified Johnson-Cook (JC) flow stress model to include the possible microstructure change in the shear zone. A semi-empirical flow stress model is developed by Guo et al. [53] to capture the dislocation density change in the primary shear zone. In order to explain the obvious strain softening effect at the high speed machining process, Calamaz et al. [54] introduced a TANH term into the traditional Johnson-cook flow stress model. A self-consistent

model is proposed by Zhang et al. [55] to account for the phase transformation effect in turning of titanium alloys. An empirical phase transformation model based on the temperature is proposed. The material flow stress is obtained from the simple mixture rule of two different phases. A physics-based continuum flow stress model is proposed by Venkatachalam et al. [56] to account for the grain size and dislocation density effect. However, the grain size evolution model is not explicitly provided. The Johnson-Mehl-Avrami-Kolmogorov model is used for the phase transformation and grain size calculation in the turning of *Ti-6Al-4V* by Arisoy et al. [57]. Based on the phase transformation and grain growth model, a modified Johnson-Cook flow stress model is proposed to consider the grain size and phase transformation effect in the machining force calculation [58]. Also, an improved chip morphology prediction is achieved.

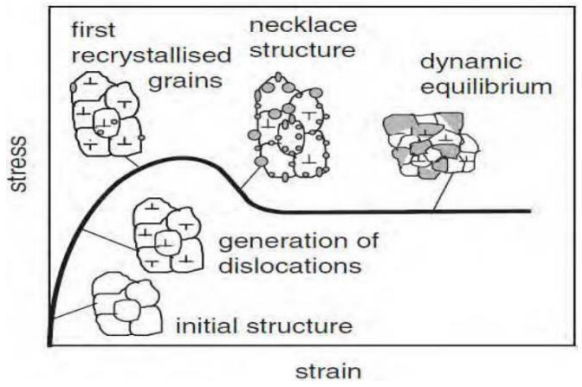

Figure 6 The influence of material microstructure on the material flow stress [52].

In addition to the modified JC models, the mechanical threshold flow stress (MTS) model is a physical thermo-viscoplastic model that involves the material dislocation glides. A modified version of the MTS model is proposed by Gourdin and Lassila [59] to incorporate the grain size effect from the Hall-Petch law into the a-thermal stress term. Most recently, Atmani et al. [60] applied the grain size sensitive MTS model to the application in turning of OFHC copper. Better machining force prediction is found compared with the traditional JC model. Some representative

microstructure sensitive flow stress models for the application of machining process are listed in the Table 3. A material microstructure affected machining process modeling framework is proposed by Omar et al. [61]. The model gives a general idea of the microstructure implementation in the machining process. Microstructure attributes such as grain size, phase transformation are included, as shown in Fig. 7.

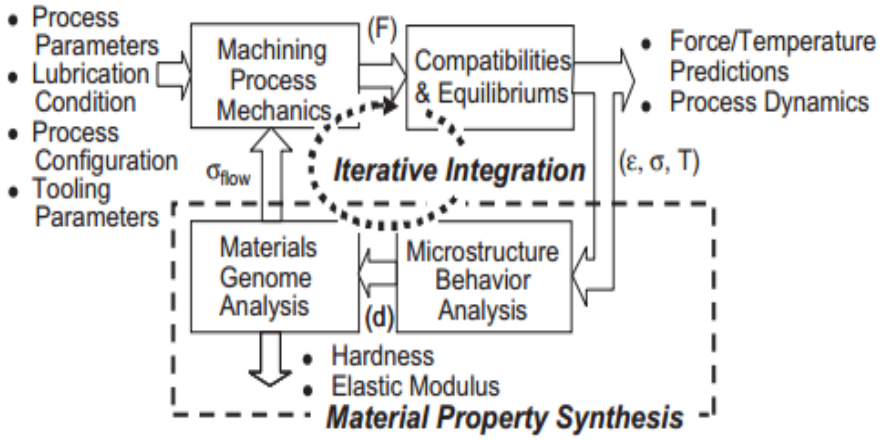

Figure 7 The material microstructure affected machining framework [61].

Table 3 Previous research on microstructure sensitive flow stress model

References	Model
Venkatachalam et al. [56]	$\sigma = \sigma_0(\varepsilon, \dot{\varepsilon}, T) + M\alpha Gb\sqrt{\frac{k\theta_{av}}{D_{avg}b}} + K_{hp}D^{-1/2}$
Andrade and Mayers [62]	$\sigma = f(\varepsilon)g(\dot{\varepsilon})h(T)H(T)$
Calamaz et al. [54]	$\sigma = (A + B\varepsilon^n(\frac{1}{\exp(\varepsilon^a)}))(1 + C\ln\frac{\dot{\varepsilon}}{\dot{\varepsilon}_0})[1 - (\frac{T - T_r}{T_m - T_r})^m]$ $(D + (1 - D)\tanh(\frac{1}{(\varepsilon + S)^c}))$
Nemat- Nasser et al. [63]	$\sigma = \sigma_0\varepsilon^n + \hat{\sigma}\{1 - [-\frac{k}{G_0T}(\ln\frac{\dot{\varepsilon}}{\dot{\varepsilon}_0})]^{1/q}\}^{1/p}$
Zerlli and Armstrong [64]	$\sigma = C_0 + C_1e^{(-C_3T + C_4T\ln\dot{\varepsilon})} + C_5\varepsilon^n$
Atmani et al. [60]	$\sigma = 0.278/\sqrt{d} + (\hat{\sigma} - \hat{\sigma}_a)\left(1 - [\frac{KT\ln(\dot{\varepsilon}_{oe}/\dot{\varepsilon}_e^p)}{g_{0\varepsilon}Gb^3}]^{1/q}\right)^{1/p}$

2.2.2 Material microstructure effect on surface integrity

The surface consideration covers a wide range of topics including heterogeneous catalysis, lubrication, adhesion and corrosion. In the manufacturing community, the surface integrity concerns the whole assemblage of the surface structure, including physical, mechanical, metallurgical, chemical and biological states. A series of publications by M'Saoubi et al. [65] laid as pioneering review work for machining induced surface integrity. The emphasis of this work would be focused on the material microstructure alteration in the machining process and how this alteration would affect the machined component surface integrity properties. The surface microstructure alterations are in the form of plastic deformation, micro-cracks, phase transformation, microhardness, recrystallization, tears and residual stress profile. Instead of giving an exhaustive list of the previous related research work, the paper will cover some major issues involved the microstructure structure affected surface integrity in the context of hard to machine material, such as nickel-based alloys and titanium alloys.

2.3 Nickel-based alloy

The nickel-based alloys retain the mechanical and chemical properties at the high temperature. However, nickel-based alloys are also thermal resistant, which makes considerable heat concentration in the machining processes. As one of the most widely used nickel-based alloys, Inconel 718 is strengthened by the body centred tetragonal γ"-Ni_3Nb precipitates and face centred cubic γ'-Ni_3 (Al, Ti) precipitates. The high yield strength of the material mainly attributes to the large volume fraction of the γ'' and γ' strengthening precipitates. The morphology and distribution of the precipitates could be determined by different heat treatment method. The γ and grain size is controlled by the cooling rates in the heat treatment. The complicated chemical composition and

intermetallic phase transformation phenomenon imposes great challenge for the microstructural investigation. The surface integrity issue concerned with the machining of Inconel 718 includes tensile residual stress, micro-hardness, metallurgical alteration and plastic deformation.

The inhomogeneous grain size distribution is found on the machined subsurface in the dry cutting condition, as shown in Fig. 8 [66]. The elongate grain morphology and a directional orientation of the grain boundary point to the cutting direction are observed. More distorted grain morphology is found on the subsurface by the worn tool where significant rubbing occurs. This microstructure alternated layer would typically contribute to the bad surface roughness. However, due to the server plastic deformation, significant strain hardening occurs, which result in the increased micro-hardness of the machined surface. The machined subsurface microhardness is plotted as shown in Fig. 9 (a) [67]. The hardness value gradually decreases when the depth into the workpiece increases. The effect of feed rate and depth of cut on the subsurface microstructure are also investigated in Fig. 9 (a). It is interesting to find that, with the increasing depth of cut, the material hardness would slight increase due to the more sever hardening effect. An empirical prediction model is also proposed to calculate the subsurface material yield stress from the micro-hardness, as shown in Fig. 9 (b).

(a) (b)

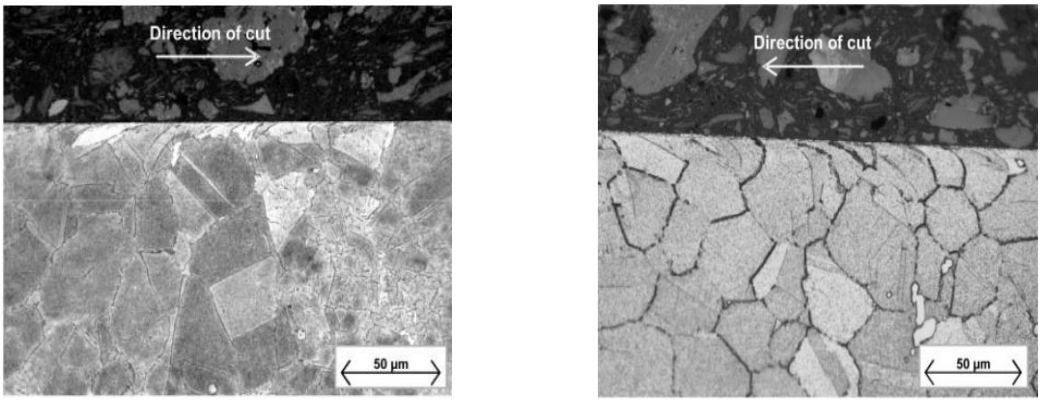

Figure 8 The machined Inconel 718 workpiece subsurface at cutting speed 60 *m/min*, feed rate 0.1 *mm/rev*, depth of cut 0.5 *mm* by a new tool (a) and a worn tool (b) [66].

(a) (b)

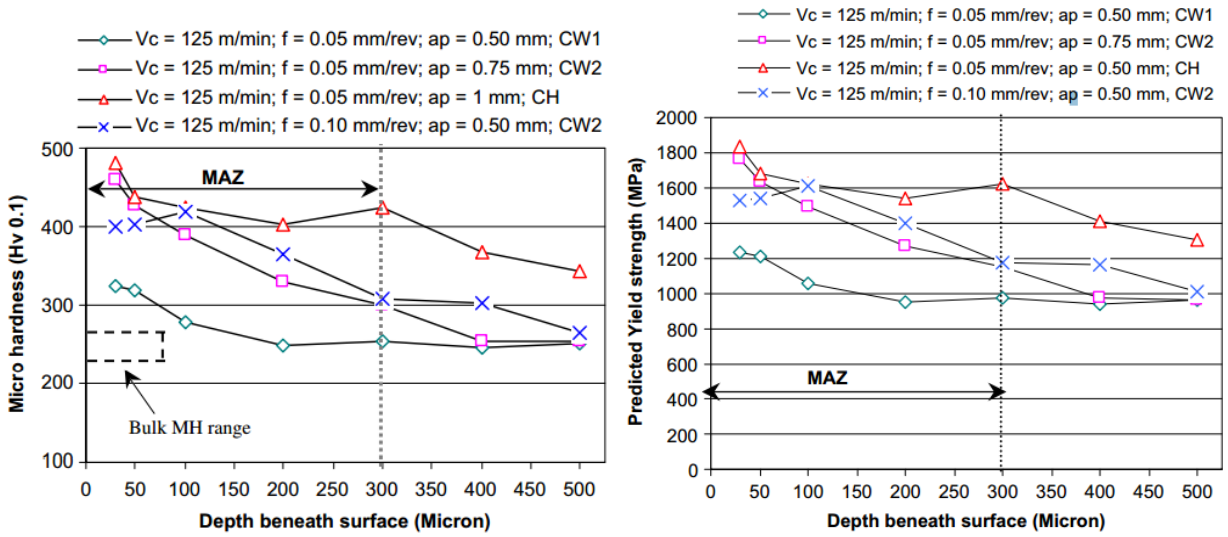

Figure 9 The material microhardness (a) and yield strength (b) as a function of depth into the workpiece at different machining conditions [67].

Large tensile residual stress on the machined surface of Inconel 718 is reported in previous literature work. Arunachalam et al. [68] concluded that the ceramic cutting tool would contribute to large tensile residual stress in the cutting direction compared with CBN tool in the hard turning of Inconel 718. Also, the uniformly deformed plastic deformation layer is found in the machined

surface of CBN tool, which indicates the possible residual stress release in uniform plastic deformation process. Compared with new cutting tool, the worn tool tends to induce server plastic deformation near the surface area from the ploughing effect [69]. This high level of strain hardening and grain distortion would result in the increased magnitude of tensile residual stress. Similar trend is also found by Outeiro et al. [70]. Comparing the residual stress distribution of the machined surface between coated and TiAlN coated cutting inserts, obvious decrease in the magnitude of tensile residual stress is observed from the TiAlN coated tool, as shown in Fig. 10. This could be explained by the less friction between the workpiece and tool, which help to decrease the plastic deformation. Also, with appropriate lubrication and cooling, the magnitude of tensile residual stress could also be reduced, as shown by Devillez et al. [66]. However, the machined surface roughness shows a better qualify in the dry cutting condition than a wet cutting, as shown in Fig. 11.

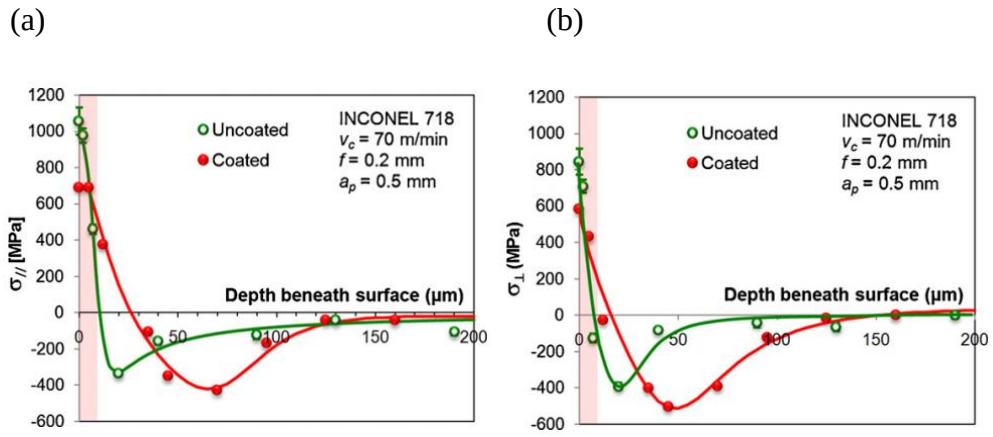

Figure 10 The residual stress profile as a function of depth into the Inconel 718 workpiece in (a) cutting direction and (b) radial direction at cutting speed of 70 *m/min*, feed rate 0.2 *mm/rev*, depth of cut 0.5 *mm* [70].

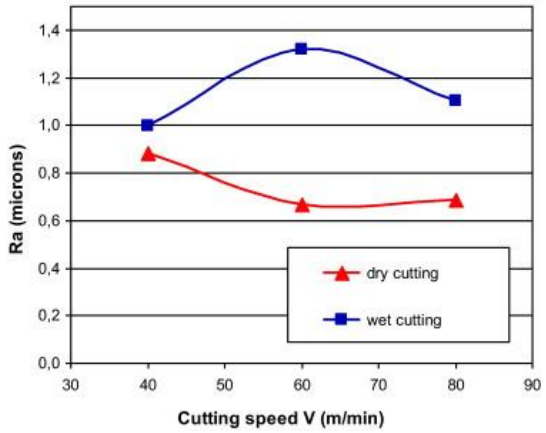

Figure 11 The surface roughness comparison in dry and wet cutting at different cutting speed, with a feed rate of 0.1 *mm/rev*, depth of cut 0.5 *mm* [66].

In a typical machining process, the surface roughness is dominated by the feed rate. The residual stress is a combined effect of uniform plastic deformation, temperature gradient and the phase transformation induced volume change. Previous research work shows interesting observations on these topics. With the increasing cutting speed, the surface roughness value would be larger. The surface residual stress in the cutting direction would become more tensile, as reported by Arunachalam [68]. In a similar study by Thakur [71], the surface roughness improves with the increasing cutting speed. However, in the separate study by Devillez [66], the residual stress is reported to be more compressive with the increasing cutting speed.

The chip morphology is dominated by the fracture initiation and propagation in the chip. The material fracture initiation is dependent on the strain, strain rate and temperature. Additionally, the material microstructure evolution, especially the phase transformation, could promote the material ductile to brittle transition in the shear zone. This ductile to brittle transition would also promote the crack initiation and result in the segmented chip morphology. In the machining of Inconel 718, the critical machining speed for chip segmentation is found to be around 50 m/min, above which the saw tooth chip would be formed. As reported by Pawade [72], segmented chip

formation in machining of Inconel 718 would increase the surface roughness value. Further study shows that, the localize shear band in the chip, which elongated grain size occurs, also contributes the segmented chip. Therefore, both the phase transformation effect and grain size growth in the shear zone would result in the segmented chip, which increases the surface roughness value.

2.4 Titanium alloy

Titanium alloys could be divided into three types based on the crystal structure, α alloys, β alloys and α + β alloy. The α alloys have α stabilizer such as aluminum and tin with hcp structure at the room temperature. High strength, toughness are the main characters of α alloys. The β alloys are in the state of bcc phase which contains large amount of β isomorphous additions, such as vanadium, niobium and tantalum. The low strength characterizes the basic mechanical property of the β alloys. For the α + β alloys, more than one α stabilizers together with β stabilizers exist. The dominating factor that influences titanium alloy mechanical properties is the α phase colony size. The yield strength, fracture toughness and ductility could be greatly improved by reducing the colony size of α phase.

A so called coating delamination phenomenon is observed by Ginting et al. [73] in the machining of Ti-6242S, which the coating layer peels off and deposit on the major cutting edge. This delamination effect results in the poor surface roughness. A comprehensive surface roughness investigation is conducted by Sun et al. [74] in the end milling of *Ti-6Al-4V*. The surface roughness value increases with the increasing cutting speed up to 80 *m/min*, and then decreases with the further cutting speed increase. A 70 μm thick hardened layer below the machined surface is reported by Che-Haron et al. [26] in the dry turning of *Ti-6Al-4V*. More obvious hardening effect is found with a worn cutting insert, as similar with the Inconel 718. This microhardness improve

could be attributed to the strain hardening in the plastic deformation process. More uniformly distributed plastic deformation layer is found at a higher cutting speed. With a worn insert, the rubbing effect is more significant. Irregular grain morphology is reported, as shown in Fig. 12. The machined surface microhardness is reported by Ginting et al. [73], as shown in Fig. 13. The micro-hardness improvement could be also due to the dynamic recrystallization process where grain refinement occurs. However, different from the Inconel 718, the large hardness value is not on the machined surface. The hardness value gradually increases from the machined surface, around 100 μm beneath the surface, the maximum value is achieved. When the depth into the workpiece further increases, the micro-hardness slight decrease. The hardness affected zone is around 350 μm. In a separate work of Sharman et al. [75] for the finish turning of gamma titanium aluminide, the maximum microhardness value is found on the machined surface rather than beneath the surface. This could be explained by the possible phase transformation or softening effect in Ginting's work where the depth of cut is larger than a finish turning. It is validated from the ball end milling of *Ti-6Al-4V* by Mhamdi et al. [76], in which the depth of milling is only 0.5 *mm*. So, in the machining process with a smaller cutting depth, the machined surface has the most significant hardening effect. In a more aggressive machining, the hardening effect is beneath the surface.

(a) (b)

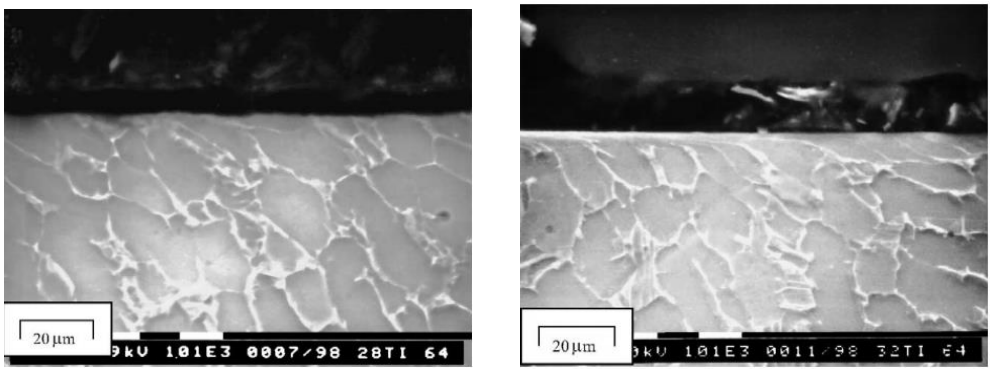

Figure 12 Machined surfaced of *Ti-6Al-4V* with a new tool (a), and with a worn out tool (b) [26].

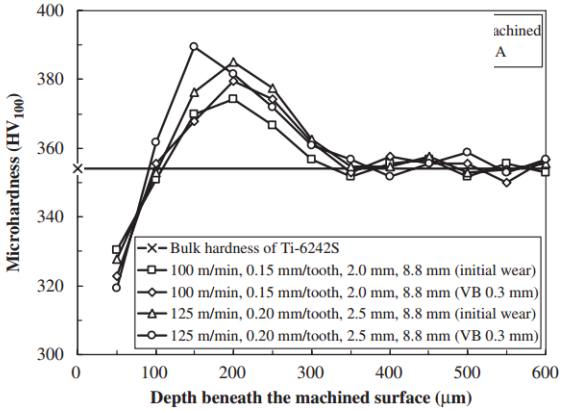

Figure 13 The micro-hardness value as a function of depth into the Ti-6242S workpiece at different cutting condition [73].

The residual stress in the cutting direction is typically found to be tensile on the machined surface [77]. The magnitude of tensile residual stress sharply decreases with the increasing depth into the workpiece. The material microstructure alteration and temperature effects are believed to be the dominating factors that influence the residual stress distribution on the machined surface. The higher cutting speed will help to increase the cutting temperature. A comprehensive study is conducted by Sun et al. [74] in the end milling of Ti-6Al-4V material, as shown in Fig. 14. It is found that the magnitude of residual stress in all three directions would slightly increase with the increasing cutting speed. The normal residual stress is almost negligible compared with the other

two directions, which indicates large shear deformation on the machined surface. Through appropriate control of the machining process parameters, the residual stress on the machined surface of Ti-6Al-4V could be altered to compressive as reported by Daymi et al. [28].

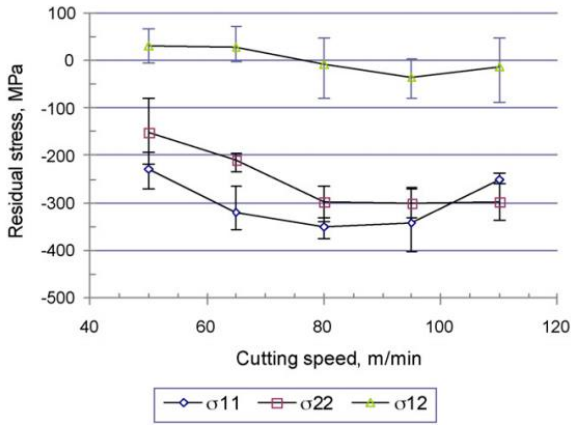

Figure 14 The effect of cutting speed on the surface residual stress at feed rate 0.08 *mm/tooth*, radial depth of cut 4 *mm*, axial depth of cut 1. 5 *mm* [74].

2.5 Laser assisted machining

The nickel based alloys, especially Inconel 718 have been widely used in the aerospace industry due to the high strength to weight ratio, corrosion resistance and high strength at elevated temperature [78, 79]. Those attractive properties of the material which contribute to its wide application also make it hard to machine at the room temperature. Excessive tool wear, built up edge, and even tool failure could occur in the machining process [80]. Much effort has been devoted for the development of new machine tools or advanced machining processes to improve the machinability of hard to machine materials in the last decades. Among all the others, cryogenic cooling and thermal assisted method prove to be very effective in increasing the machine tool life.

The flow stress of Inconel 718 could have significant decrease when the temperature increases up to 650 ^{o}C. Besides the flow stress decreasing at the elevated temperature, the reduced

work hardening and annealing effect from heating also help to improve the machinability of Inconel 718 [81, 82]. The laser assisted machining (LAM) is a hybrid manufacturing process, which integrates a high energy laser beam into the traditional machining process to achieve large material removal rate, reduced tool wear. At the high-temperature, the material flow stress would be much smaller than that of the room temperature. Also, there is a brittle to ductile transition for material at elevated temperature, which could significantly reduce the chip segmentation induced chattering.

The main parameters involved in the LAM is the laser power input, laser spot size, and the machining process parameters. To achieve the optimal process parameter in the LAM, comprehensive experimental work and simulation would be required in the process and material envelope. The laser serves as a good heat source for the machinability improvement of Inconel 718 in the machining process. Extensive research has been done for the process optimization on the LAM [83, 84]. The LAM utilizes a high energy laser beam to locally heat the workpiece before the material removal by machining tool.

The early work of LAM was proposed by Bass et. al. [85] with a carbon dioxide laser for the hot spot machining of nickel alloys. The LAM could help to significantly reduce the machining force. Due to the material brittle and ductility transformation, the magnitude of the machining force variation also has sharp decrease. To improve the surface integrity, the LAM was used by Chang et al. [86] for the machining of ceramics. The feasibility of LAM on the machining of hard to machining metals was investigated on the titanium alloy and nickel alloys. Experimental investigation was conducted by Anderson et. al [79] for the evaluation of tool wear and surface roughness improvement in the milling of Inconel 718. More than 50% material removal rate improvement is achieved with LAM compared to traditional milling process. With appropriate

turning parameter selection, Ding et. al. [87] showed that the cutting forces could have more than 20% drop in LAM compared against traditional milling. More than 150 *MPa* compressive axial residual stress was also observed on the LAM of hardened steel.

CHAPTER 3. MATERIAL MICROSTRUCTURE EVOLUTION IN MACHINING

3.1 Introduction

Ti-6Al-4V alloy has high strength to weight ratio, excellent corrosion resistance and biocompatibility, which makes it one of the most commonly used titanium alloy in medical industry and aerospace engineering [88-90]. However, due to the low thermal conductivity and high rigidity, high temperature, large strain and high strain rate would occur in the machining process of *Ti-6Al-4V* material [91, 92]. This will result in obvious microstructure change and mechanical property degradation. The fatigue life and corrosion resistance of the machined parts are highly dependent on the microstructure and mechanical properties of the machined surface [93, 94]. *Ti-6Al-4V* is a dual phase (α + β) alloy, which has a variety of microstructure dependent properties [54]. Among all the microstructural properties, the average grain size and volume fraction of the two-different phase play significant roles in the mechanical properties of the *Ti-6Al-4V* material.

Tremendous research has been conducted to investigate the phase transformation and grain growth of the *Ti-6Al-4V* in hot forging, friction stir welding or laser sintering process [95, 96]. The challenge of microstructure evolution in machining process comes from the complicated stress, strain and temperature coupling relation. Based on extensive experimental data, Malinov et al. [97] developed a neural network model to correlate the processing parameters with microstructure evolution for titanium alloy. Zhang et al. [55] investigated the phase transformation on the serrated chip formation in the high speed machining process of *Ti-6Al-4V* material. The work was based on a steady state phase transformation approximation which might not be as accurate for the high-

speed machining. Arisoy et al. [57] explicitly calculated the grain size growth of *Ti-6Al-4V* in machining with a dynamic recrystallization approach. The apparent phase transformation was not considered, which could have significant influence on the material flow stress. Ducato et al. [98] predicted the phase transformation of *Ti-6Al-4V* in the hot forging process. For *Ti-6Al-4V* material, the dynamic recrystallization and phase transformation are concurrent processes in the thermal-mechanical machining process. However, no comprehensive study has been provided to investigate how the machining parameters could explicitly influence both the phase transformation and grain size evolution of *Ti-6Al-4V* material.

The objective of this study is to provide a physics-based finite element model that is capable of capturing the dynamic recrystallization grain growth and phase transformation in the machining process. A modified Johnson-Cook (*JC*) material flow stress model is used for strain and temperature prediction. The flow stress model takes the phase transformation into account. Based on the temperature, strain and strain rate history, the Johnson-Mehl-Avrami-Kolmogorov (*JMAK*) model [99] is proposed for the dynamic recrystallization grain growth. According to time-temperature-transformation (*TTT*) diagram for the *Ti-6Al-4V*, the phase transformation from α to β is calculated. The β to mixed $\alpha + \beta$ phase transformation in the cooling is calculated with the generalized form of Avarmi model. The simulation results are compared with the literature data for model validation.

3.2 JMAK model for grain growth

The *JMAK* model has been widely used to describe the dynamic recrystallization process of crystalline material by considering the strain, strain rate and temperature [100]. The basics of *JMAK* model is the calculation of the recrystallized volume fraction of the material as a function

of time. The grain size is obtained from the grain growth rate and nucleation. The dynamic recrystallization is defined with the Avrami equation as

$$X_{drex} = 1 - \exp[-\beta_d (\frac{\varepsilon - a_{10}\varepsilon_p}{\varepsilon_{0.5}})^{k_d}] \quad (1)$$

where ε is the strain, ε_p is the peak strain, X_{drex} is the volume fraction of dynamically recrystallized material. $\varepsilon_{0.5}$ is the strain for X_{drex} = 0.5 and it is given by

$$\varepsilon_{0.5} = a_5 d_0^{h_5} \varepsilon^{n_5} \dot{\varepsilon}^{m_5} \exp(Q_{act} m_5 / RT) + c_5 \quad (2)$$

where R is the gas constant, d_0 is the initial diameter of the grain, a_5, h_5, n_5, m_5, c_5 are material constants which could be determined by experiments and regression analysis, Q_{act} is the activation energy. A critical strain at which the dynamic recrystallization would occur is defined as $\varepsilon_c = 0.8\ \varepsilon_p$. The peak stain ε_p is denoted as

$$\varepsilon_p = a_1 d_0^{h_1} \dot{\varepsilon}^{m_1} \exp(Q_{act} m_1 / RT) + c_1 . \quad (3)$$

where a_1, h_1, m_1, c_1 are material constants. The grain size after recrystallization is given by

$$d_{drex} = a_8 d_0^{h_8} \varepsilon^{n_8} \dot{\varepsilon}^{m_8} \exp(Q_{act} m_8 / RT) + c_8 \quad (4)$$

where a_1, h_1, n_8, m_1, c_1 are the material constants. The average grain size is calculated with a mixture rule as

$$d = d_0 (1 - X_{drex}) + d_{drex} X_{drex} . \quad (5)$$

The initial average grain size is characterized as d_0 = 15 μm. The JMAK model parameters for grain growth are partially obtained from on Quan et al. [101] and Arisoy et al. [57] and are listed in table 4.

Table 4 *Ti-6Al-4V* material constants of *JMAK* model [102]

Peak strain	a_1	h_1	m_1	$Q_{act}m_1$		c_1		a_2	
	0.0064	0	0.0801	30579 *J/mol*		0		0.8	
DRx kinematics	a_5	h_5	n_5	m_5	$Q_{act}m_5$	c_5	β_d	k_d	a_{10}
	0.022	0	0	0.11146	26430 *J/mol*	0	0.9339	0.5994	0.0311
DRx grain size	a_8	h_8	n_8	m_8	$Q_{act}m_8$	c_8			
	150	0	0	-0.03	-6540	0			

3.3 Model of phase transformation

The microstructure modelling of *Ti-6Al-4V* consists of two phases, α phase and β phase. The initial microstructure of *Ti-6Vl-4V* is bimodal, mainly composed α grains with low concentration of β. In the thermal heating process, $_{\alpha}$ destabilizes and the transformation from α to β starts above the β transformation temperature according to the phase transformation curves. Also, in the cooling down process, the β phase starts to slowly decompose into α phase. Therefore, two different α phase need to be distinguished, Widmanstatten and grain boundary [95]. In the current study, to simplify the model, it is assumed that the material only consists of primary α and β phase.

For the heating process where the phase transformation of α to β takes place, a simplified Avrami model [103] is used as

$$\vartheta_v = 1 - e^{\{A(\frac{T-T_s}{T_e-T_s})^D\}} \quad (6)$$

where T is the temperature, Ts = 600 ^{0}C is the phase transformation starting temperature, T_e = 980 ^{0}C is the temperature when the process ends, A_s and D_s are material constants to be determined.

The calculation of A_s and D_s could be conducted through an experimental curve of the phase transformation. In the current work, A_s and D_s are selected as -1.86 and 4.35 from a previous study [98].

In the cooling down process, the β to $\alpha + \beta$ transformation is characterized by the TTT curve, as shown in Fig. 15. As for the α to β transformation in cooling, the coefficient is used as a mean value of a set of data from literature, which could be described by the function of time as

$$\xi_V = 1 - e^{-bT^n} \quad (7)$$

where b is the material constant and n =1.32 is the Avrami number. The dynamic recrystallization of the grain growth and phase transformation model are implemented in the finite element code for microstructural evolution simulation.

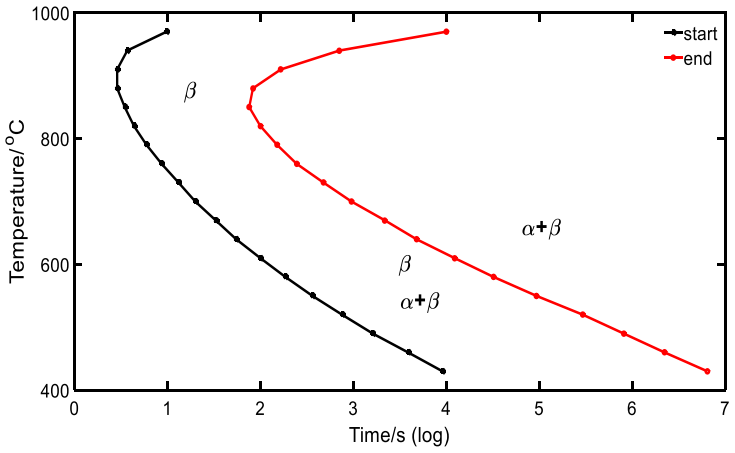

Figure 15 TTT curve of *Ti-6Al-4V* [103]

3.4 Finite element model for 2D orthogonal cutting

The numerical procedure of the proposed microstructural modelling scheme is implemented in a finite element software Deform (Scientific forming technologies corporation, Columbus, OH). The initial *Ti-6Al-4V* workpiece material is characterized with an average grain

size of 15 μm and the volume fraction of the α phase is 95%. The tungsten carbide (WC) is selected for the cutting tool. The cutting tool is assumed as a rigid body. The displacement boundary condition of the workpiece is defined by restricting the base of workpiece in *x*- direction. A plain-strain coupled thermal-mechanical model by considering dynamic recrystallization is implemented. Since the dry cutting condition is assumed here, the workpiece and tool are allowed to exchange the heat with the environment at a heat convection coefficient of 20 $W/(m^2 \cdot K)$, which is a typical value for free air convection. The environment temperature is set as 20 ^oC.

The friction between the tool and workpiece involves both the sticking and sliding [104]. The sticking region is dominated by the Tresca model, which is equal to the maximum shear stress, $\tau = \tau_{max}$. The shear force in the sliding region is governed by Coulomb model $\tau = \tau\sigma_n$, where μ is the friction coefficient, α is the flow stress of the workpiece material in uniaxial tensile test. A simple estimation could be conducted as $\tau = \sigma/\sqrt{3}$, so the maximum shear stress in the sticking region is estimated to be 300 *MPa* for *Ti-6Al-4V* in high speed machining. Thermal and mechanical properties of the workpiece material are collected from a previous study [104], which are listed in table 5. The mechanical properties could be measured by a uniaxial tensile test. The thermal properties could be obtained transient plane source tests. For the cutting tool material WC, the heat capacity is 2.21106 $J/(m^3 \cdot K)$ and conductivity is 26.7 $W/(m \cdot K)$.

Table 5 Thermal and mechanical properties of *Ti-6Al-4V* [105]

Young's modulus(*MPa*)	$0.714T + 113.34 \times 10^3$
Density(Kg/m^3)	4430
Poisson's ratio	0.34
Heat capacity($J/(kg \cdot °C)$)	$505.64 \exp(0.0007T)$
Conductivity($W/(m \cdot °C)$)	$7.039 \exp(0.0011T)$
Expansion($\mu m/(m \cdot °C)$)	$3 \times 10^{-9} T + 7 \times 10^{-6}$

The fracture initiation and propagation in the chip segmentation is capture by the Cockroft and Latham's [106] fracture criterion as

$$\int_0^{\bar{\varepsilon}_f} \sigma_1 d\varepsilon = D_f \qquad (8)$$

where ε_f is the effective strain, σ_1 is the maximum principle stress, D_f is the material constant, which is called the material fracture coefficient. The integration of the largest tensile principle stress component over the plastic path is evaluated on D_f. The fracture will occur, and chip segmentation starts once the integral reaches the fracture coefficient. The chip morphology is dominated by the combination of shear coefficient μ and the fracture coefficient D_f. A classic iteration scheme could be carried out by optimizing the chip morphology to find the combination. In this paper, μ and D_f are selected as 0.7 and 200 from a previous study [104].

3.5 Simulation results and discussion

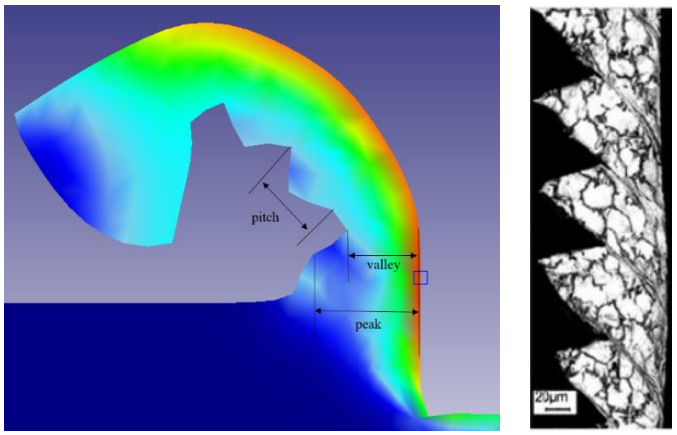

Figure 16 Comparison of experimental and simulated chip morphology

For the validation of the above proposed flow stress model, the chip morphology comparison test is first conducted. The tool workpiece configuration consists of a 0^o rake angle and 6^o clearance angle. The tool radius is about 5 μm. Cutting speed at two levels 1200 *m/min*,

4800 *m/min*, at the feed rate of 70 *μm/rev* are implemented for the validation. The chip characteristic parameters such as valley, peak and pitch defined in Fig. 16. The chip morphology parameters are measured and compared with the experimental data, as shown in Table 6. The biggest estimation error is 27.5% and the predicted chip geometry parameters are very close to the experimental measurements [107].

Table 6 Comparison of predicted chip dimensions with measured data

	Experimental			Modeling		
Cutting condition	Valley/*μm*	Peak/*μm*	Pitch/*μm*	Valley/*μm*	Peak/*μm*	Pitch/*μm*
v=1200 *m/min*,	50.3	105.7	68.2	50.1	93.5	50.7
f=0.07 *mm/rev*				(0.4%)	(-11.5%)	(-25.7%)
v=4800 *m/min*,	26.5	49.5	42.9	19.2	57.4	47.2
f=0.07 *mm/rev*				(-27.5%)	(16.0%)	(10.0%)

In order to validate the proposed material dynamic recrystallization grain growth model in the machining process, the cutting condition and tool geometry are kept the same as Arisoy et al. [57] for the purpose model validation. The rake angle is zero, clearance angle is 5^{o}, tool radius is 5 μm. The microstructure evolution data at different cutting speed and feed rate is investigated. In the high-speed machining process, the grain size tends to decrease both on the machined surface and the chip, as shown in Fig. 17. The temperature affected depth is very close to the microstructure evolution affected depth on the machined surface, which indicates that the temperature dominates the grain growth. The simulated grain size growth data shows very good agreement with the experimentally measured data, as shown in Table 7. The grain size would decrease both when the feed rate and cutting speed increase. A proper cutting speed could be determined based on the above model for the *Ti-6Al-4V* material which will result in finer grain size and better surface integrity of the cutting surface. A similar trend for has also been found for the machining of IMI834 Titanium alloy by Balasundar et al [108]. With the increasing of strain

rate and decreasing temperature, the average recrystallized grain size will increase after a thermos-mechanical process.

Table 7 Comparison of the experimental and simulation for microstructure change

Cutting condition	Experimental		Modeling	
	Grain size/μm	α volume fraction	Grain size/μm	α volume fraction
v=55 *m/min*, *f*=0.05 *mm/rev*	15	--	14.7	75.20%
v=55 *m/min*, *f*=0.1 *mm/rev*	13.6	--	14.5	66.40%
v=90 *m/min*, *f*=0.05 *mm/rev*	13.6	--	14.5	74.50%

Since in the current model, the microstructure evolution is not only dependent on the temperature history, the strain and strain rate play significant roles in the Avrami equations. In the machining, the strain and strain rate are mainly dominated by the cutting speed. Different cutting speeds are selected here to investigate their effect on the microstructure change. The highest temperature in the machining process reaches up to 833 ^{o}C, which is approaching the β phase transformation temperature (about 980 ^{o}C). All α phase will transform to β if the temperature exceeds 980^{o}C in an equilibrium state. However, due to the high speed of the machining process, the obvious phase transformation only takes places on the chip where large strain and high strain rate occurs. The driving force for the phase transformation in *Ti-6Al-4V* comes from the free energy difference in α and β phase, which is about 1.0 *kJ/mol* [109]. The dynamic recrystallization process is driven by the tracked energy in the dislocation density in the deformation process, it is only about 0.05 *kJ/mol*. The required energy for the phase transformation is more than one magnitude higher than that of the dynamic recrystallization. The α to β phase transformation only take place

after the dynamic recrystallization is completed. In the machined surface of the workpiece material, only a small amount of α to β is involved even though the dynamic recrystallization process is significant.

(a) (b)

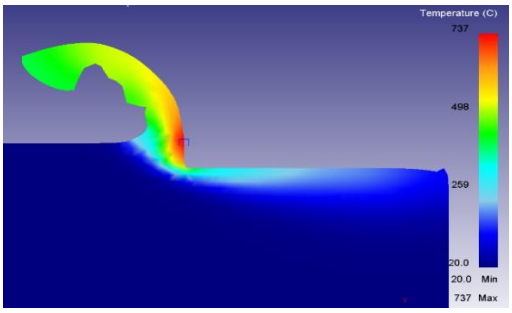

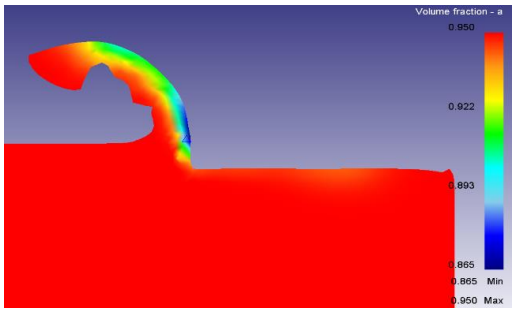

(c) (d)

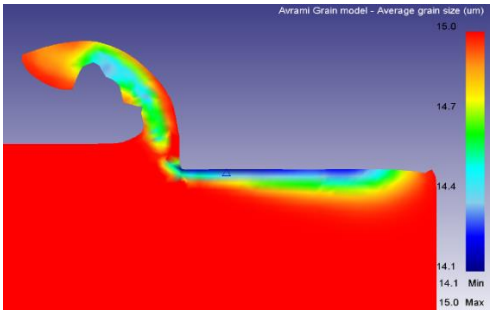

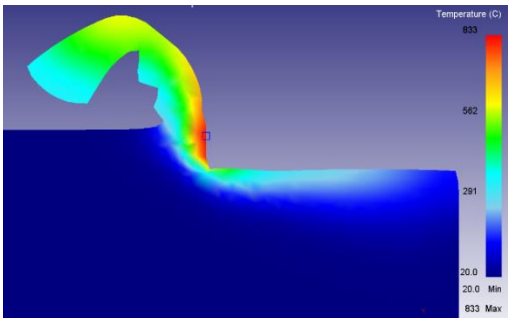

(e) (f)

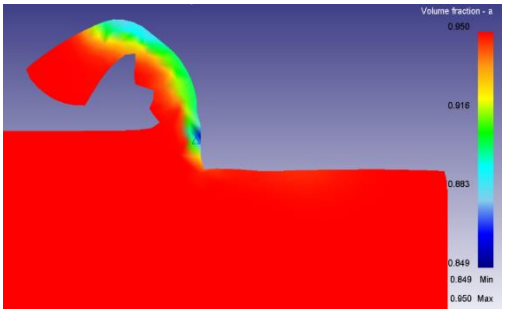

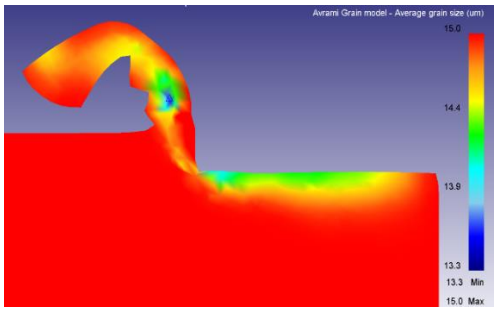

Figure 17 The temperature (a), α phase volume fraction (b) and average grain size (c) of the machined surface at the cutting speed of 55 *m/min*; The temperature (d), α phase volume fraction (e) and average grain size (f) of the machined surface at cutting speed of 90 m/min.

To validate the accuracy of the phase transformation model, one set simulation was conducted. The volume fraction of the β phase varies between 5% - 25.3%. Significant phase transformation (up to 25.3% β phase) occurs at the tool chip interface where there exists the highest temperature and strain rate, as shown in Fig. 17. As shown in Zhang's paper, when the cutting speed increases in the high-speed machining process, more phase transformation could occur which will further influence the chip morphology of the *Ti-6Al-4V*. As noted in the temperature distribution map, the temperature can reach up to about 800 ^{o}C. Large volume fraction of β phase should be expected. However, due to the fast cooling down process, the reverse transformation of β to α is very obvious. So the volume fraction of the β phase in the primary shear zone is almost negligible. In the tool chip interface, the cooling rate is comparatively much smaller due to the air convection which results less reverse phase transformation.

To investigate the effect of cutting speed on the microstructural evolution, both the grain size and phase transformation at a cutting speed of 21.8 *m/s*, 43.6 *m/s* and 65.4 *m/s* were simulated. When the cutting speed increases, the grain size of the resultant surface and the α phase volume fraction of the chip both decreases, as shown in Fig. 18. For *Ti-6Al-4V* material, finer grain structure would result in improved mechanical property. However, larger volume fraction of the β phase could be detrimental to the service functionalities of the workpiece, since the yield strength of the β phase is only 33% of the α phase.

(a) (b)

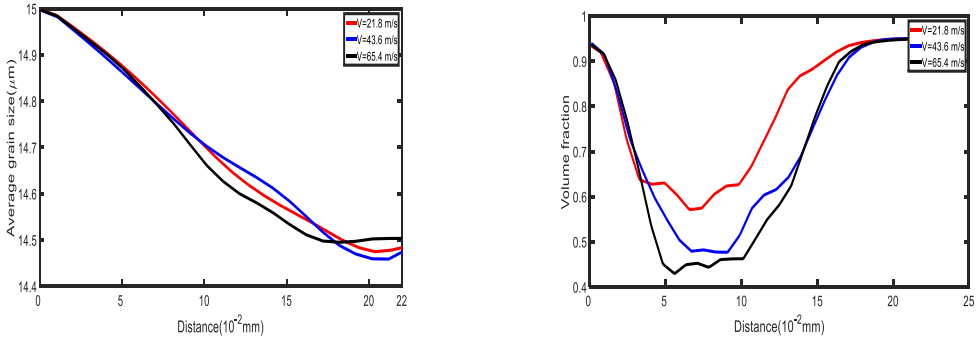

Figure 18 The effect of cutting speed on the grain growth of the machined surface (a), The effect of cutting speed on the volume fraction of α phase on the chip (b).

For the effect of feed rate on the resultant workpiece microstructural change, one more simulation was conducted at a cutting speed of 21.8 *m/s* with feed rate of 0.1 *mm/rev*, 0.15 *mm/rev*, 0.2 *mm/rev*, respectively. The grain size of the machined surface tends to decrease as the feed rate increases from 0.1 *mm/rev* to 0.2 *mm/rev*, as shown in Fig. 19 (a). This indicates the strengthened mechanical property on the surface with larger feed rate. The volume fraction of the α phase decreases when increasing the feed rate from 0.1 *mm/rev* to 0.15 *mm/rev*. However, when the feed rate further increases from 0.15 *mm/rev* to 0.2 *mm/rev*, the volume fraction of the α phase shows slight increase, as shown in Fig. 19 (b).

(a) (b)

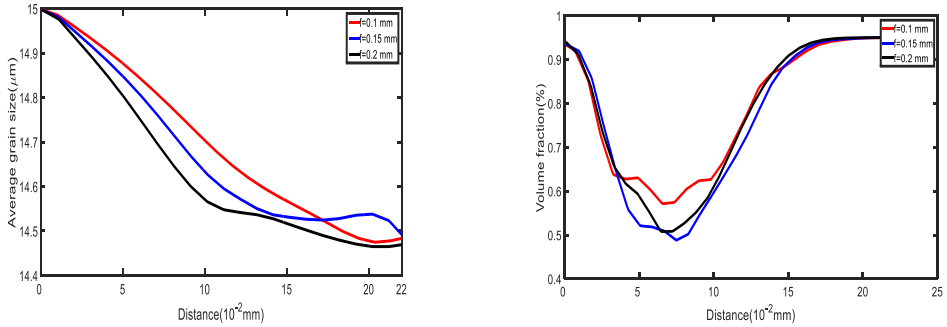

Figure 19 The effect of feed rate on the grain growth of the machined surface (a), The effect of feed rate on the volume fraction of α phase on the chip (b).

3.6 Conclusion

A dynamic recrystallization-based microstructure modelling *JMAK* method was introduced and implemented to predict the grain growth and phase transformation of *Ti-6Al-4V* material in the machining process. A new modified *JC* model was developed by directly relating the material flow stress with the phase transformation of the dual phase *Ti-6Al-4V* material for the first time. The method was validated to be accurate by comparison with experimental data. The effects of cutting speed on the machined surface has been investigated at three different levels ($v = 21.8m/s, 43.6m/s, 65.4m/s$) on the workpiece and chip. The results show higher machining speed helps to decrease the grain size of the machined surface in the high-speed machining. Also, the volume fraction of the β increases with the higher machining speed due to the elevated temperature at higher speed. For the effect of increasing feed rate, its decreasing effect on the grain size of the workpiece is more significant. The same trend of increasing volume fraction of β phase is observed as feed rate increases. The proposed *JMAK* method for microstructural evolution provides a new avenue for machining parameter optimization and final workpiece

material mechanical property prediction. Additionally, a multiphase material inverse modelling for machining could be developed based on the proposed microstructure evolution model.

CHAPTER 4. MATERIAL MICROSTRUCTURE SENSITIVE FLOW STRESS MODELING IN MACHINING

4.1 Introduction

Ti-6Al-4V alloy has been widely used in aerospace, biomedical and automobile industry due to its high strength to weight ratio, fracture toughness and corrosion resistance [110-112]. However, *Ti-6Al-4V* is also regarded as hard to machine material because of its low thermal conductivity, instability in the plastic deformation and high chemical reactivity with the cutting tool material [113, 114]. The low thermal conductivity will contribute to the temperature and stress concentration at the tool-workpiece interface. The significant instability in the adiabatic shear bands could result in chattering of the manufacturing system. The chemical reactivity of *Ti-6Al-4V* with cutting tool material will accelerate the tool wear in the machining process.

The proper selection of the machining process condition and tool material property is important not only in the aspect of machining productivity, the machined surface integrity, residual stress and workpiece microstructure are also influenced. To accurately predict the mechanical property of the workpiece material from different machining conditions, the material flow stress model is of great importance. The *JC* model is the mostly used flow stress model because of its simplicity and considerable accuracy. The *JC* model relates the material flow stress with the strain, strain rate and the temperature. The *JC* model has been successfully applied for the flow stress prediction of material in the machining process, such as Aluminum 7075 [115], hardened 52100 steel [116, 117]. *Ti-6Al-4V* is a two-phase material which composes of α phase and β phase. At the room temperature, the hexagonal close-packed (hcp) crystalline structure α phase dominates.

When the temperature rises up to the phase transformation temperature (about 800 ^{o}C), the volume fraction of the body centered cubic (bcc) slip structure β phase will increase [118]. This microstructure change in the machining process would have significant influence on the material flow stress, which is ignored in the traditional *JC* model.

Extensive research has been conducted for the application of *JC* flow stress model for the *Ti-6Al-4V* material in the machining process. A direct data fitting method from Hopkinson pressure bar tests was used by Lee and Lin [119] to model the deformation behavior of Ti-6Al-4V. Andrade and Meyers [120] introduced a modified term to include the material recrystallization effect on the flow stress. A similar flow softening term was suggested by Calamaz et al. [54] to capture the decreasing of flow stress above a critical strain value. Instead of a continuum level description, Nemat-Nasser et. al. [63] introduced a thermally activated stress term by considering the effect of dynamic microstructure change and deformation dislocation. However, the strain, strain rate and temperature coupling effect are not fully captured in the model. A so called self-consistent flow stress model was developed by Zhang et. al. [55] to include the phase transformation effect of *Ti-6Al-4V*. The model is essentially a data fitting method which dose not explicitly involve the microstructure evolution.

A recently developed model by Liang et. al. [102] included the phase transformation effect on the material flow stress by explicit calculation of the phase transformation of *Ti-6Al-4V* in the machining process. However, the accuracy of the phase transformation model was not adequately calibrated against experimental data. Also, further study shows that grain size effect on the flow stress is also comparable to the phase transformation. In the current study, a microstructure-sensitive flow stress model (MSM) is proposed by explicit calculation of both the phase transformation and grain growth. The phase transformation model is improved by a more

comprehensive time-temperature-transformation (*TTT*) diagram. The microstructural evolution model parameters and flow stress model are calibrated with measured experimental data. The MSM is implemented in a finite element code in the orthogonal cutting process by modifying the traditional *JC* model. The proposed model is validated by comparison with experimental data. Additionally, the influence of microstructure evolution on the segmented chip formation and final chip morphology is investigated.

4.2 Microstructural sensitive flow stress model

In order to include the microstructure properties into the flow stress model, physical based models have been developed, such as crystal plasticity model for metal [121], modified JC model and self-consistent model for composite material [122]. Crystal plasticity is a computational expensive method which considers the material texture evolution and material dislocation density. It could not be easily applied to the machining process which involves complicated large elastoplastic deformation and high temperature. For the *JC* model, which describes the material flow stress as a function of strain, strain rate, temperature as,

$$\sigma = (A + B\bar{\varepsilon}^{n})[1 + C\ln(\frac{\dot{\bar{\varepsilon}}}{\dot{\varepsilon}_0})]\left\{1 - \left[\frac{T - T_0}{T_m - T_0}\right]^m\right\}. \quad (9)$$

As noted by Calamaz et al. [54], there was some significant decrease of the flow stress at the extremely high strain rate condition. A strain softening term is added to the classic JC model. Sima et al. [123] found that the softening term is a coupled effect from both the strain softening and temperature softening. Zhang et al. [55] proposed a self-consistent model to consider the effect of phase transformation in the multiphase phase material *Ti-6Al-4V*. However, the self-consistent model is only based on an iterative regression scheme without explicitly calculation of the microstructure properties.

The microstructure properties, such as the average grains size and phase volume fractions, have significant roles in the material flow stress of the *Ti-6Al-4V*. Obvious microstructure change could occur in the machining process due to the concentrated heat generation in machining process. The average grain size and volume fraction of different phase could have very significant change depending on the machining configurations. The bcc β phase has much smaller flow stress than the hcp α phase. The flow stress of *Ti-6Al-4V* would vary from 850 MPa to 1100 MPa after different heat treatment at the room temperature. In order to more accurately capture the effect of microstructure properties on the flow stress of *Ti-6Al-4V*, a modified JC model could include a volume fraction term and average grain size term for the application of machining. Different from the previous flow stress model which only considers the phase transformation effect, the current model would take the effect of grain size change into the consideration. At a microscale perspective, the hcp crystal of *Ti-6Al-4V* has a strong grain-boundary. The grain boundary hardening exhibits a similar behavior with Hall-Petch effect which was observed in a typical dual phase *Ti-6Al-4V* material. The grain size effect on the flow stress could be denoted as the Hall-Petch equation as,

$$A = A_{hp} + K_{hp} D^{-0.5} \quad (10)$$

where A_{hp} and K_{hp} are the Hall-Petch parameters. The constant $K_{hp,\alpha}$ and $K_{hp,\beta}$ for different phases are taken as 803.22 $MPa \cdot \mu m^{0.5}$ and 401.61 $MPa \cdot \mu m^{0.5}$ [124], $A_{hp,\alpha}$ and $A_{hp,\beta}$ are estimated to be 517.31 *MPa* and 237.86 *MPa* respectively from the measured flow stress. The average grain size of the alpha phase will increase as a function of the temperature [125]. Seshacharyulu et. [89] reported that more than 40% volume fraction of b phase would occur when the temperature increased up to 900 ^{o}C. The flow stress value of the α and β phases are plotted as the function of strain rate, temperature and the average grain size for the machining of *Ti-6Al-4V* material, as shown in Fig. 20 (a, b) and (c, d) respectively. Compared to the strain rate, the flow stress is a

weak function of the average grain size in the current flow stress model. In our current grain size range between 10 μm and 18 μm, the flow stress deviates no more than 10%.

After the calculation of the flow stress for each phase σ_α and σ_β from equation (8), a mixture rule could be used to get the nominal flow stress of the two-phase material as

$$\sigma_{\alpha+\beta} = \eta\sigma_\alpha + (1-\eta)\sigma_\beta \qquad (11)$$

where η is the volume fraction of the α phase. The equivalent flow stress of the dual phase $\alpha + \beta$ *Ti-6Al-4V* material is plotted as a function of strain rate and temperature, as shown in Fig. 21. In the MSM, the flow stress is a strong function of the volume fraction of the β phase. The equivalent flow stress is dependent on the initial material microstructure and the machining condition. The equivalent flow stress is less than that of the flow stress of α phase at the same condition, but larger than that of β phase. When the temperature increases up to the phase transformation temperature in the primary shear zone and secondary shear zone, the flow stress would have significant decrease.

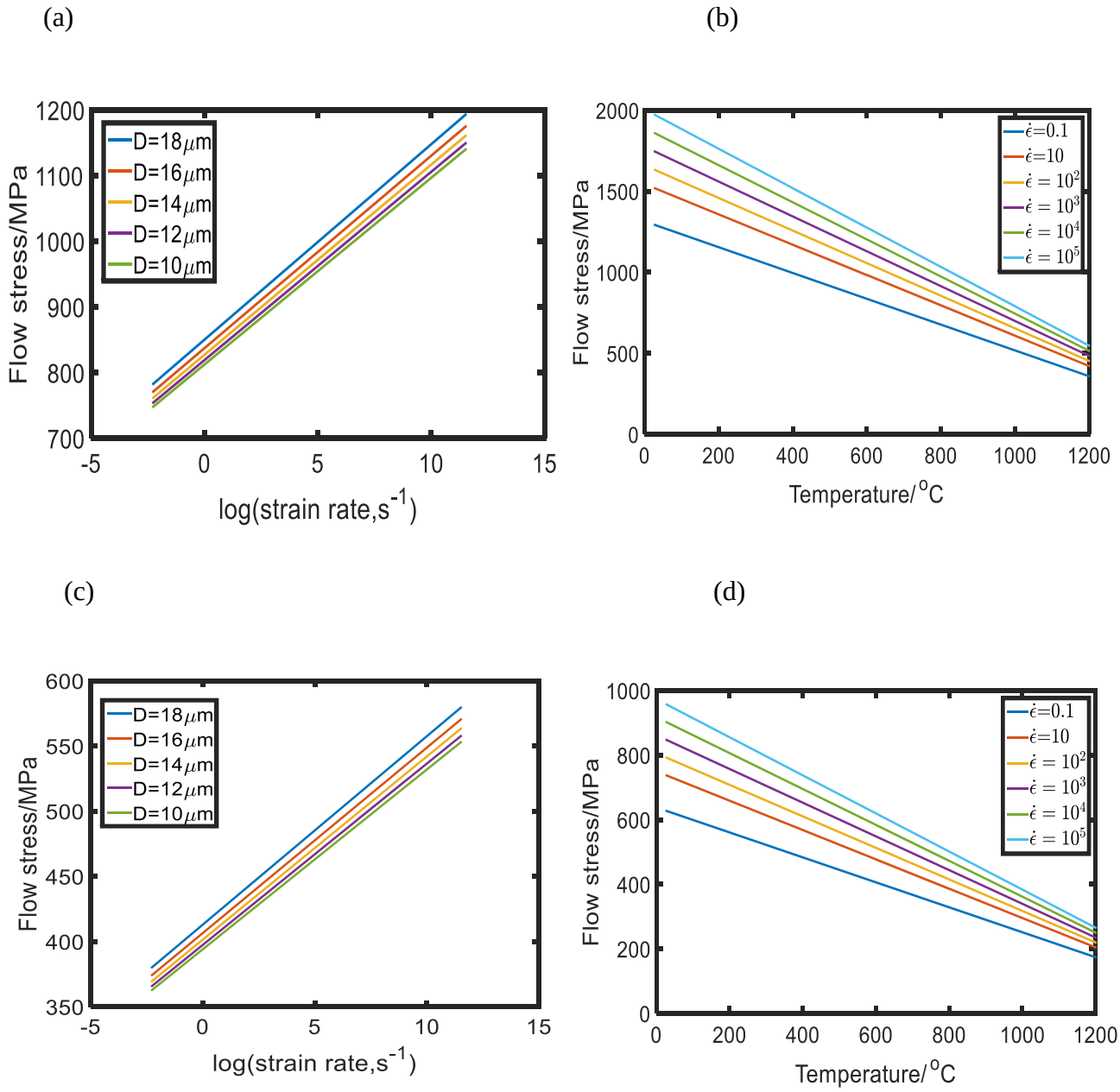

Figure 20 The flow stress as a function of strain =1, temperature = 700 °C, strain rate (a) and strain =1, grain size =15 μm temperature (b) for α phase; the flow stress as a function of strain rate (c) and temperature (d) for β phase.

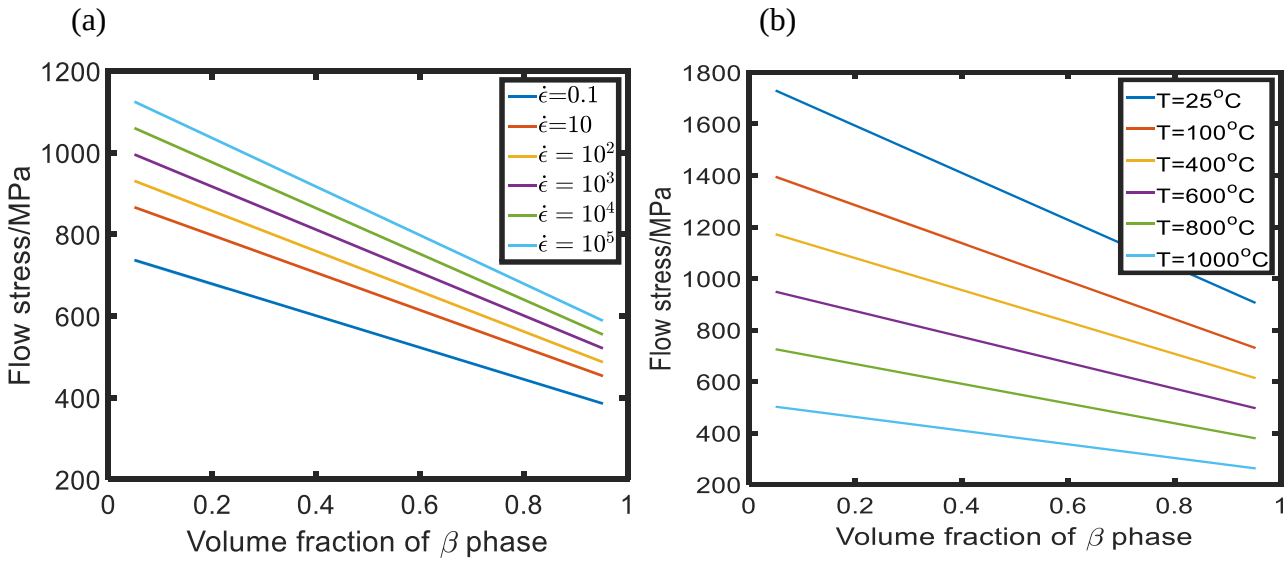

Figure 21 When temperature T = 700 ºC and strain ε = 1, the equivalent flow stress as a function of strain rate and β phase volume fraction (a); when strain rate $\dot{\varepsilon} = 10^4 s^{-1}$, strain ε =1, the equivalent flow stress as a function of temperature and β phase volume fraction (b).

4.3 Model development of 2D turning

The finite element model for the two dimensional (2D) orthogonal cutting process is developed in a commercial finite element software Deform (SFTC, Columbus, OH). The as received *Ti-6Al-4V* rod is measured with an initial average grain diameter of 15 μm by an optical microscope. The initial volume fraction of the β phase is 5%. For cutting tool material, the tungsten carbide (WC/Co) is used here. For simplicity, the tool is regard as non-deformable in the machining process. The boundary condition for displacement of the cutting tool in both *x*- and *y*-directions are fixed as zero. The workpiece is restricted on the based to move only in the *x*-direction. The imbedded dynamic recrystallization model for phase transformation and grain size evolution is activated. The MSM flow stress model is implemented as a subroutine written in Fortran code in the Deform, as schematically shown in Fig. 22. The dry cutting environment assumption is used here. Both the workpiece and cutting tool are allowed to have heat convection

with the surrounding environment at the rate of 20 W/(m^2·K) in the machining process. The environmental reference temperature is 20 ^{o}C.

Both the sliding and sticking are involved in the friction between the tool and workpiece. The Tresca model dominates the sticking region. The shear stress is equal to the maximum shear stress, $\tau = \tau_{\max}$. In the sliding region, the shear force is dominated by Coulomb model $\tau = \mu\sigma_n$, where μ is the interfacial friction coefficient, σ_n is the normal stress on the friction interface. So, the friction model could be summarized as

$$\tau = \begin{cases} \tau_{\max}, & if \quad \mu\sigma_n > \sigma/\sqrt{3} \\ \mu\sigma_n, & if \quad \mu\sigma_n \le \sigma/\sqrt{3} \end{cases} \qquad (12)$$

where σ is the material flow stress. Thermal and mechanical properties of the *Ti-6Al-4V* are obtained from a previous study [15]. The density is 4430 *Kg/m*^{3}; Poisson's ratio is 0.34. The Young's modulus, heat capacity and conductivity are temperature dependent properties, which is taken as $0.714T + 113.34 \times 10^3$, $505.64e^{0.0007T}$, $7.039e^{0.0011T}$. T is the temperature in the unit of ^{o}C. Since a rigid tool assumption is used for the cutting tool of WC/Co, only the thermal properties are required. The constant heat capacity and heat conductivity are taken as 2.21×10 *J/(m*^{3}*·K)* and 26.7*W/(m·K)*, respectively.

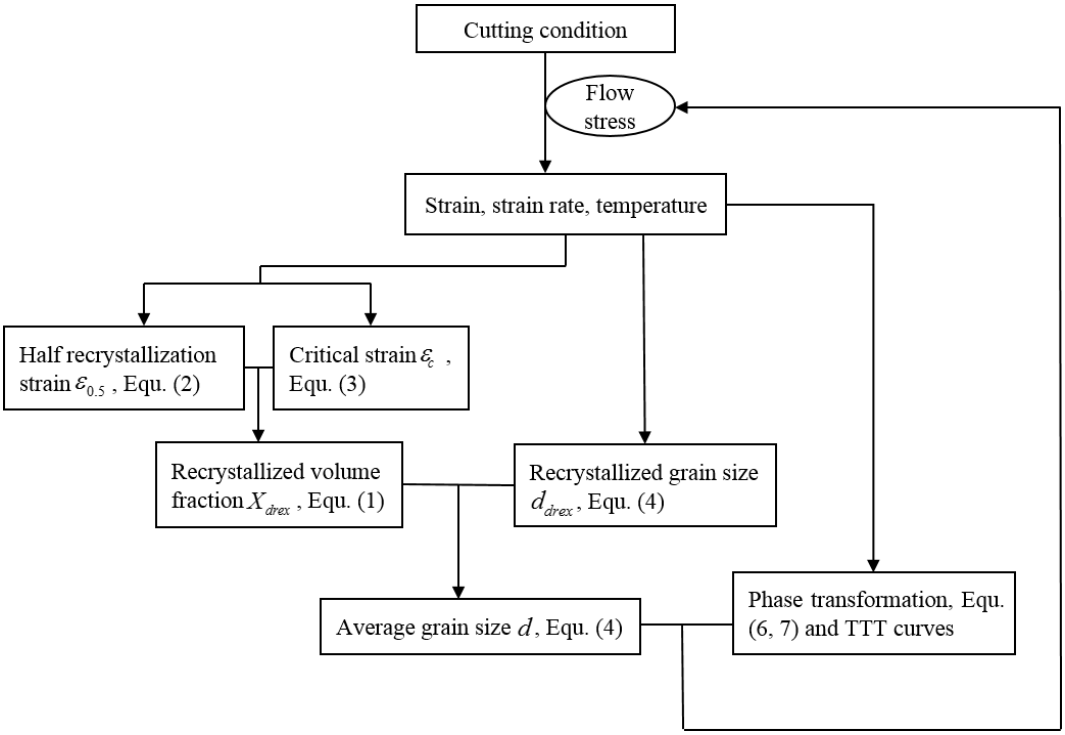

Figure 22 Schematic illustration of the grain growth and phase transformation implementation.

4.4 Results and experimental validations

Previous research has shown that, the segmented chip morphology is generated in the machining of *Ti-6Al-4V* material. The validation for the proposed MSM flow stress model is conducted by the chip morphology comparison with experimental results. The cutting tool confirmation is selected as rake angle 0^o, clearance angle 6^o, cutting tool radius 5 μm. In the machining process, the uncut chip thickness is 76 μm. An iterative scheme is implemented to optimize the chip morphology. A combination of μ and D_f are selected as 0.7 and 0.354 in the current study.

With the same machining configuration, the temperature, equivalent stress, average grain size and α phase volume fraction from the MSM and traditional *JC* model are plotted for

comparison, as shown in Fig. 23. Due to the microstructure evolution effect, the flow stress computed from the MSM is relatively smaller, which are validated by the temperature and effective stress distribution map as in Fig. 23 (a, b) and (e, f). At the high temperature machining condition, the dynamic recrystallization occurs which results in grain could size refining of the machined workpiece. The smallest average grain size on the workpiece surface reduces to 14.3 μm in the MSM compared against 14.1 μm from a traditional *JC* flow stress model, as shown in Fig. 23 (c, g). Obvious dynamic recrystallization occurs both on the workpiece and the segmented chips. Since the surface integrity of the workpiece material is important for the workpiece service quality. The reduced grain size will help to increase the surface micro hardness and strength. The phase transformation is clearly indicated in Fig. 23 (d) on the segmented chip for a traditional *JC* model. The significant volume fraction increase of the laminated α phase will help to promote the fracture propagation in the segmented chip formation. The maximum machining temperature in the MSM is 671 ^{o}C, which is below the phase transformation temperature. No obvious phase transformation occurs. Compared with the α phase, the laminated β phase has lower fracture toughness.

For the phase transformation validation, the effect of the cutting speed and feed rate on the phase transformation are investigated. When the cutting speed increases from 55 m/s to 90 m/s, the average grain size on the surface of the workpiece would slightly decrease. For the phase transformation, it is a direct function of the temperature history. When the machining temperature becomes higher, larger volume fraction of the β phase would be generated. This agrees well the prediction as shown in Fig. 24 (a), as the volume fraction of the β phase increases on the chip with increasing cutting speed and feed rate. The predicted grain size data agrees well with the experimental data at different cutting conditions, as indicated in Table 2.

When the turning feed rate increases from 0.05 *mm* to 0.1 *mm*, the grain size of the machined surface would have slight decrease as shown in Fig. 24 (b, c). The dynamic recrystallization is dependent on the temperature, strain rate and strain. The larger feed rate will contribute the increased machining temperature which will promote the grain refinement. The volume fraction of the α phase also has the decreasing trend with the increasing feed rate.

4.5 Conclusion

A modified *JC* MSM was developed by including the phase transformation and grain size evolution for *Ti-6Al-4V* material. The material flow stress model was validated by phase transformation and grain size growth prediction at various cutting speed and feed rate in the 2D orthogonal cutting. Good agreement is found between the experimental data and the prediction model outputs. More than 5% flow stress softening on the primary shear zone was observed due microstructure evolution. The MSM was applied for the grain size, phase transformation and chip morphology prediction. With the increasing of cutting speed and feed rate, reduced average grain size was predicted on the machined surface of the workpiece which could help to increase the surface microhardness and corrosion resistant. The phase transformation plays significant role in the segmented chip formation process. Parametric study shown that the increasing cutting speed and feed rate could promote the α to β phase transformation. Up to 11.2% β phase volume fraction was observed in the primary shear zone of high speed turning of *Ti-6Al-4V*.

(a)

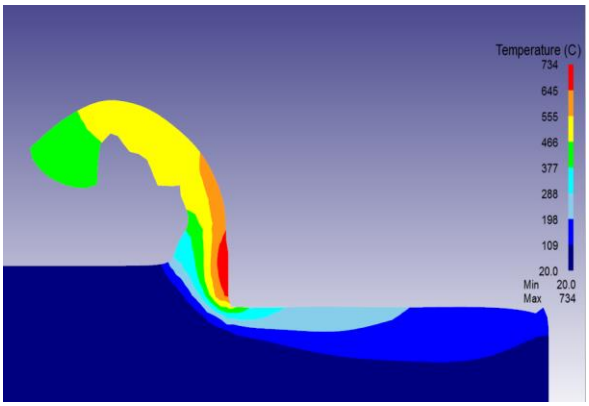
Temperature (C)
734
645
555
466
377
288
198
109
20.0
Min 20.0
Max 734

(b)

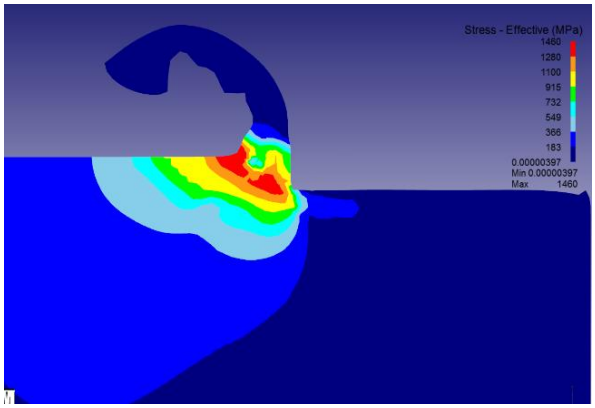
Stress - Effective (MPa)
1460
1280
1100
915
732
549
366
183
0.00000397
Min 0.00000397
Max 1460

(c)

(d)

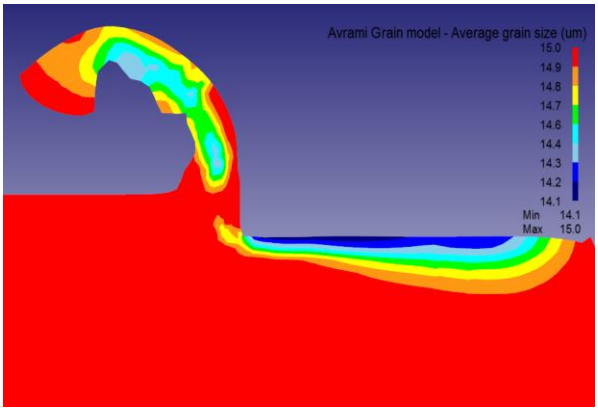
Avrami Grain model - Average grain size (um)
15.0
14.9
14.8
14.7
14.6
14.4
14.3
14.2
14.1
Min 14.1
Max 15.0

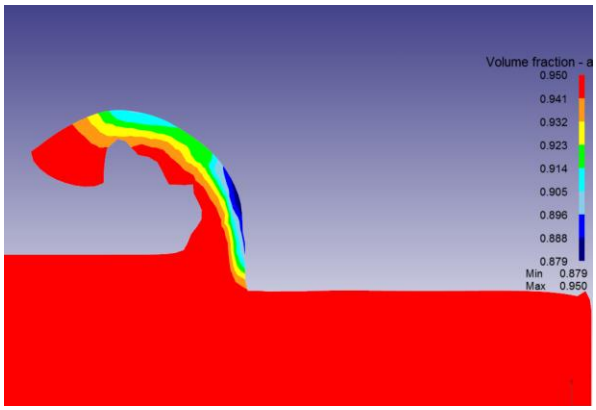
Volume fraction - a
0.950
0.941
0.932
0.923
0.914
0.905
0.896
0.888
0.879
Min 0.879
Max 0.950

(e)

(f)

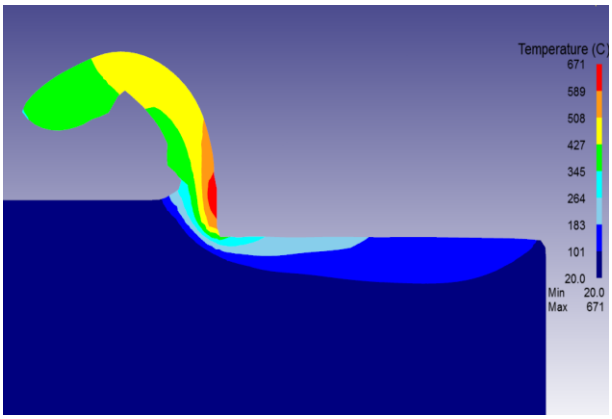
Temperature (C)
671
589
508
427
345
264
183
101
20.0
Min 20.0
Max 671

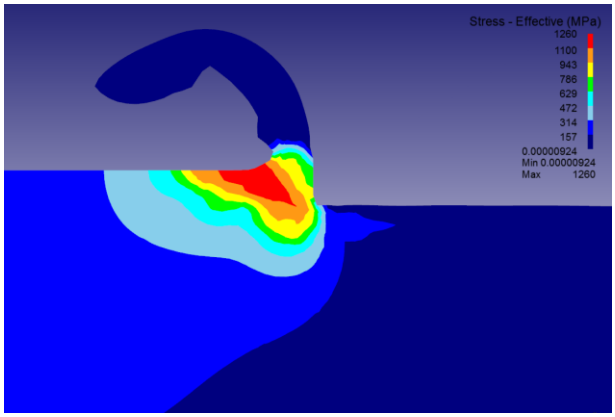
Stress - Effective (MPa)
1260
1100
943
786
629
472
314
157
0.00000924
Min 0.00000924
Max 1260

(g)

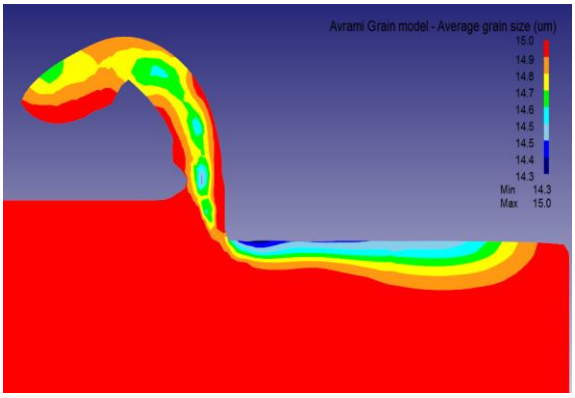

Figure 23 The comparison of temperature (a), stress (b) and average grain size (c) and volume fraction of the α phase distribution for a traditional Johnson-Cook flow stress model with the that of microstructure sensitive flow stress model (c, d, e).

(a)

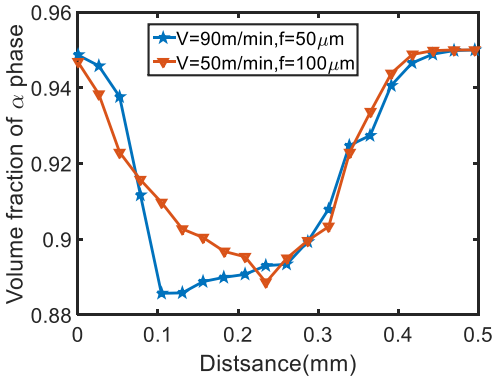

(b)

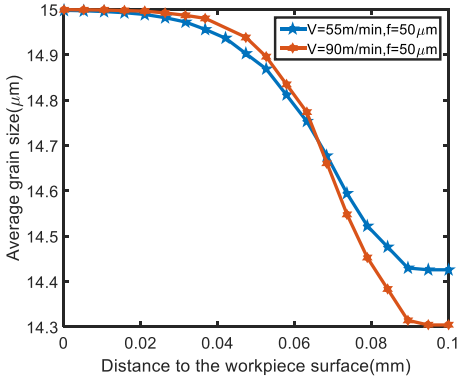

(c)

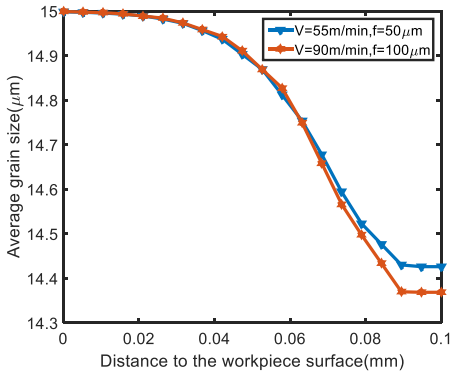

Figure 24 The effect of cutting speed and feed rate on the grain size evolution and phase transformation.

CHAPTER 5. FORCE AND RESIDUAL STRESS PREDICTION IN MACHINING

5.1 Machining force prediction

5.1.1 Introduction

In the machining process, the tool wear and machine total power input are strongly dependent on the cutting forces [3, 126-128]. The reduced cutting forces could help to improve the tool life. The resultant tool deflection could also be reduced to achieve high geometric accuracy [129]. The process mechanics on machining involves complicated thermomechanical coupling. The tool geometry, cutting process parameters and workpiece material are the key factors to be considered for machining forces determination [130]. The early work on machining forces mainly focuses on the experimental measurement. With advanced re-meshing techniques, the finite element method (*FEM*) is applied for the force prediction in machining [131]. Although, considerable accuracy is achieved from the *FEM*, the physical material response is not clearly indicated. Another problem with the *FEM* is the computational efficiency, especially in dealing with three-dimensional machining. Analytical model provides an easy implementation method for the machining process modeling. The analytical prediction model could have considerable accuracy with a high computational efficiency [132, 133]. The material mechanical and thermal response in the machining process could be explicitly calculated.

Ti-6Al-4V, as a widely used material in medical and aerospace industry, has been extensively investigated in the manufacturing process [74, 104]. *Ti-6Al-4V* is a typical $\alpha + \beta$ alloy. At the room temperature, the material mainly consists of α phase with scattered distribution of β phase. The β phase transformation temperature is around 600 ^{o}C. When the temperature rises up to the phase transformation temperature, the dynamic recrystallization will occur. The early report on the microstructure change on the manufacturing process of *Ti-6Al-4V* focuses on the hot forming process [134, 135]. With the development of high speed machining, the increased machining temperature could help to promote the microstructure evolution. The dynamic recrystallization is reported by Wan *et al.* [32] in the adiabatic shear zone in the high speed

machining process. No clear indication of how the recrystallized grain structure would influence the material mechanical response is given. Yigit *et al.* [57] proposes a *FEM* model for the grain size evolution in the turning of *Ti-6Al-4V*. The explicit calculation of the average grain size on the machined workpiece is given. The recrystallized grain structured is found to significantly influence the material mechanical properties in the primary shear zone, which results in the segmented chip formation.

A recent study proposed by Pan et. al. [102] includes the effect of phase transformation on the material flow stress in the machining of *Ti-6Al-4V*. The explicit calculation of the phase transformation is provided. The obvious phase transformation is predicted on the machined workpiece surface. However, the effect of grain size evolution is largely ignored. To accurately calculate the material dynamic recrystallization in the machining process of *Ti-6Al-4V*, an analytical based *JMAK* model will be developed in the current study. The recrystallized volume fraction of the material is calculated. The recrystallized grain size is obtained by grain growth and nucleation. A modified Johnson-cook (*JC*) flow stress model will be developed to account for the effect of grain size on material flow stress. The analytical model will be used for the cutting forces prediction for both orthogonal turning and 3D turning of *Ti-6Al-4V*. Comparison against the experimental data will also be provided.

5.1.2 Orthogonal cutting force model

A sharp tool assumption is made here for the calculation of steady state cutting forces with the classic Oxley's contact mechanics model, as shown in Fig. 25. In the orthogonal turning, a plane strain analysis is used. The stress distribution is calculated along the shear plane *AB*. The shear angle is defined as ϕ, which will be determined with an iterative algorithm. The undeformed chip thickness is *t*. Large deformation occurs on the shear zone. The shear velocity in the shear plane could be denoted as

$$V_S = \frac{\sin\phi}{\cos(\phi-\alpha)}V \qquad (13)$$

where V is the cutting speed, α is the rake angle. Similarly, the chip flow velocity could be obtained as

$$V_C = \frac{\cos\alpha}{\cos(\phi-\alpha)}V \quad (14)$$

By neglecting the elastic deformation, the shear plane *AB* plastic strain could be denoted as,

$$\varepsilon_{AB} = \frac{\cos\alpha}{2\sqrt{3}\sin\phi\cos(\phi-\alpha)} \quad (15)$$

With a constant cutting velocity *V*, the strain rate in *AB* plane is

$$\dot{\varepsilon}_{AB} = \frac{C_{Oxley}V\sin^2\phi}{\sqrt{3}t} \quad (16)$$

where C_{Oxley} is the Oxley's constant. In the shear zone, large plastic deformation could help to induce concentrated heat generation. The heat generated per unit volume could be calculated from the shear force and shear velocity. The average temperature in the shear plane could be described as

$$T_{AB} = T_0 + \eta_P \Delta T \quad (17)$$

where T_0 is the room temperature, η_P is the plastic energy to heat conversion ratio, taken as 0.9. The temperature increment includes the plastic deformation in the primary shear plane $F_S V_S$, the chip flow rate is ρVtw. The temperature rise in the primary shear zone could be obtained as

$$\Delta T = \frac{(1-\beta)F_S V_S}{C_P \rho Vtw} \quad (18)$$

where F_S is the shear force, β is the energy dissipation coefficient, *w* is the width of cut, ρ is the material density, C_P is the heat capacity. With an explicit calculation of the dynamic recrystallization in the shear zone, the average grain size *d* could be obtained. The material flow stress could be obtained from the modified *JC* model as

$$k_{AB} = \frac{1}{\sqrt{3}}(A_{hp} + K_{hp}d^{-0.5} + B\varepsilon_{AB}^n)(1 + C\ln\frac{\dot{\varepsilon}_{AB}}{\dot{\varepsilon}_0})(1-(\frac{T_{AB}-T_0}{T_m-T_0})^m) \quad (19).$$

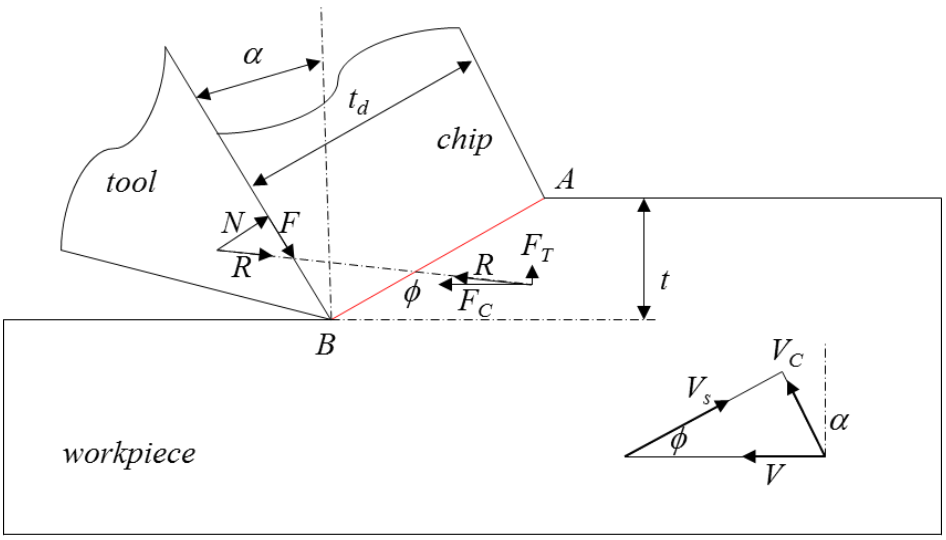

Figure 25 Chip formation model

With the given geometrical consideration, the friction angle is λ could be obtained as

$$\lambda = \theta + \alpha - \phi \quad (20)$$

The resultant force inclination angle is given by

$$\theta = \arctan(1 + 2(\pi/4 - \phi) - Cn) \quad (21)$$

where C_n is the modified Oxley constant. The tool chip contact length could be calculated as

$$h_C = \frac{t\sin\theta}{\cos\lambda\sin\phi}(1 + \frac{Cn}{3\tan\theta}) \quad (22)$$

Assuming that the stress is uniformly distributed in the tool workpiece interface, the shear stress would be obtained as

$$\tau_{\text{int}} = \frac{F}{hw} \quad (23)$$

where F is the shear force. With a similar approach as mentioned for the temperature increase in the shear zone, the temperature on the tool/chip interface could be obtained as

$$T_{\text{int}} = \frac{F\sin\alpha}{\rho C_p tw\cos(\phi - \alpha)} + T_{AB} \quad (24)$$

The strain rate in chip could be calculated from chip flow velocity as

$$\dot{\varepsilon}_{\text{int}} = \frac{V_C}{\sqrt{3}\delta t_d} \quad (25)$$

where δ is the strain rate coefficient, t_d is the deformed chip thickness. The strain in the deformed chip is determined to be

$$\varepsilon_{\text{int}} = 2\varepsilon_{AB} + \frac{h_C}{\sqrt{3}\delta t_d} \quad (26)$$

The chip flow stress is given as

$$k_{\text{int}} = \frac{1}{\sqrt{3}}(A_{hp} + K_{hp} d^{-0.5} + B\varepsilon_{\text{int}}^{n})(1 + C\ln\frac{\dot{\varepsilon}_{\text{int}}}{\dot{\varepsilon}_0})(1 - (\frac{T_{\text{int}} - T_0}{T_m - T_0})^m) \quad (27)$$

The shear angle calculation is conducted by an iterative loop, as shown in Fig. 26. An initial value of 5° is assigned to the loop, with an increasing step size of 0.1°. The τ_{int} and k_{int} are compared in each step. The largest ϕ value is selected at which $\tau_{int} = k_{int}$. When the shear angle ϕ is calculated, the force components could be determined from the following equations

$$F_T = \frac{k_{AB} tw\cos(\lambda - \alpha)}{\sin\phi\cos\theta} \quad (28)$$

$$F_C = F_t \tan(\lambda - \alpha)\,. \quad (29)$$

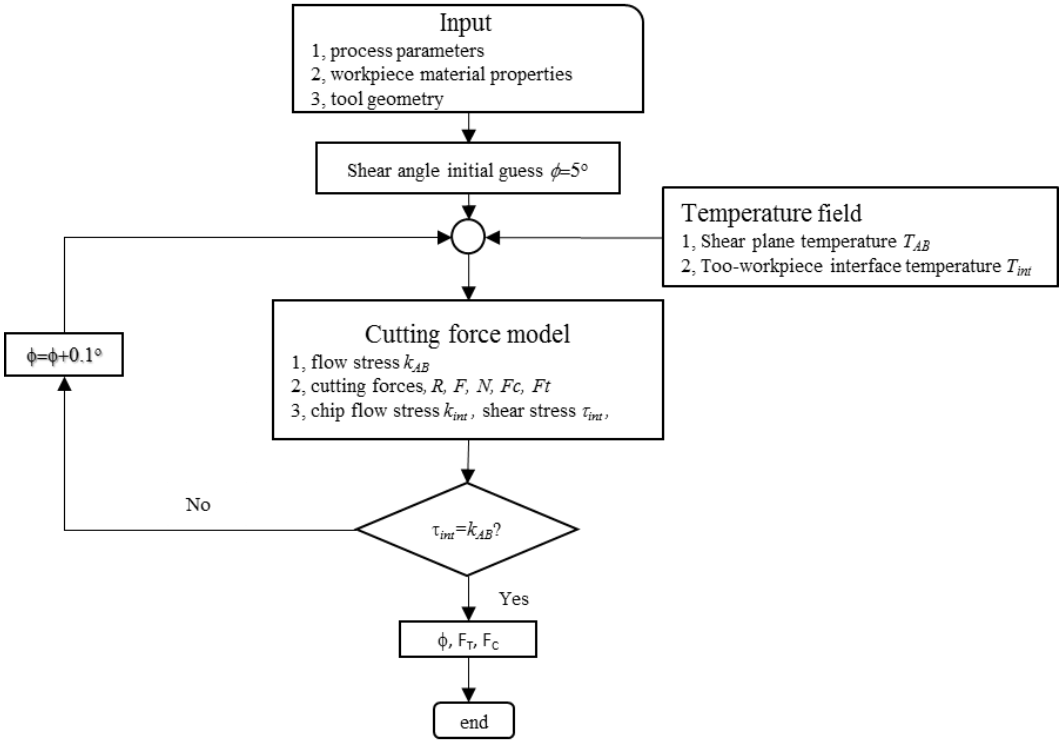

Figure 26 Iterative loop for shear angle determination

With the above-mentioned method, different orthogonal cutting conditions are used for forces prediction. The orthogonal turning experimental data are selected from Su [136] for the model validation. The cutting speed is fixed at 0.5 *m/s*, rake angle is 8°. The tool edge radius is 13 μm. The width of cut is 3.8 *mm*. The depth of cut ranges from 25 μm to 0.153 *mm*. To investigate the grain size effect on the cutting forces, the comparison study is conducted between a classic analytical model and the grain evolution embedded model. By varying the depth of cut, the cutting force data from experiment, classic model and grain evolution model are listed in Table 8. The predicted cutting force and experimental measurement force F_c are plotted in Fig. 27 (a). The predicted cutting force tends to be larger than the experimental measurement. The analytical model with the dynamic recrystallization model shows a closer approximation to the experiment. With the grain size evolution, the material flow stress will decrease due to the augmented grain size. The similar trend is found for the ploughing force predictions, as shown in Fig. 27 (b).

For further cutting force validation, three more tests are conducted by varying the rake angle, as listed in Table 9. In these tests, the cutting speed is 0.5 *m/s*, width of cut is 3.8 *mm*, depth of cut is 0.153 *mm*. The rake angle ranges from 8° to 15°. The predicted cutting forces and ploughing forces are plotted in Fig. 28 (a, b). The model with the grain size effect shows a more accurate prediction with the experimental data.

The grain size effect consideration gives a more accurate machining force prediction as indicated in the orthogonal turning case. In the traditional *JC* model, the material flow stress is only dependent on the strain, strain rate and the temperature. The material microstructure influence on the flow stress is not clearly indicated. Previous research has shown the obvious grain size growth in the adiabatic shear zone in turning of *Ti-6Al-4V*. The chip formation in machining is dominated by the material stiffness degradation in the shear zone [137]. The catastrophic shear failure will be induced by the plastic instability in the primary shear zone, which generates the chip segmentation. The segmented chip was observed at a low cutting speed of 1.3×10^{-3} *m/min* in turning of *Ti-6Al-4V* [138]. The grain growth in the shear zone will help to reduce the material flow stress and promote the fracture propagation. This could also partially contribute to the segmented chip formation in turning of *Ti-6Al-4V*. To further investigate the grain size evolution effect on the chip morphology, a material damage model would be required, which is out of the scope of our current study. One thing worth to note, the predicted force is consistently smaller than the measurement in all three directions. As has been stated in the previous study, the dynamic

measured cutting force due to the chip segmentation would slightly higher than that of the static force [139].

(a) (b)

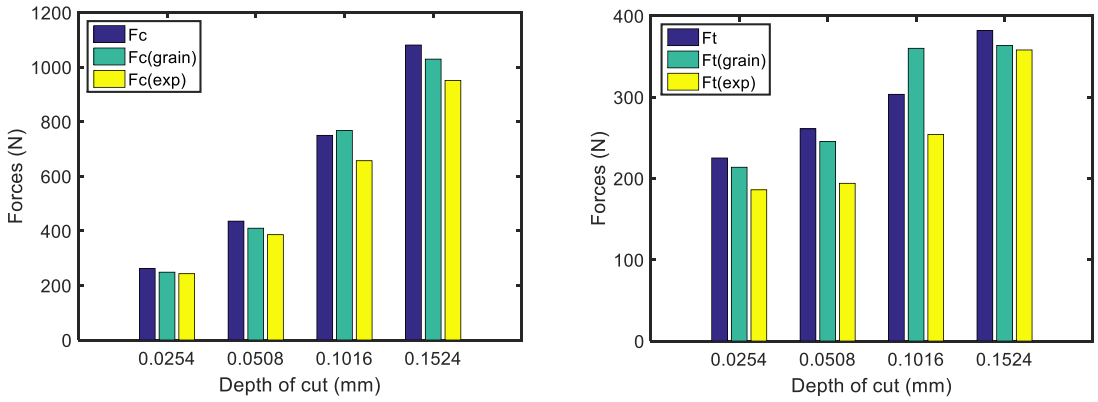

Figure 27 Cutting force F_c (a) and ploughing force F_t (b) with a rake angle of 8^o at different depth of cut

(a) (b)

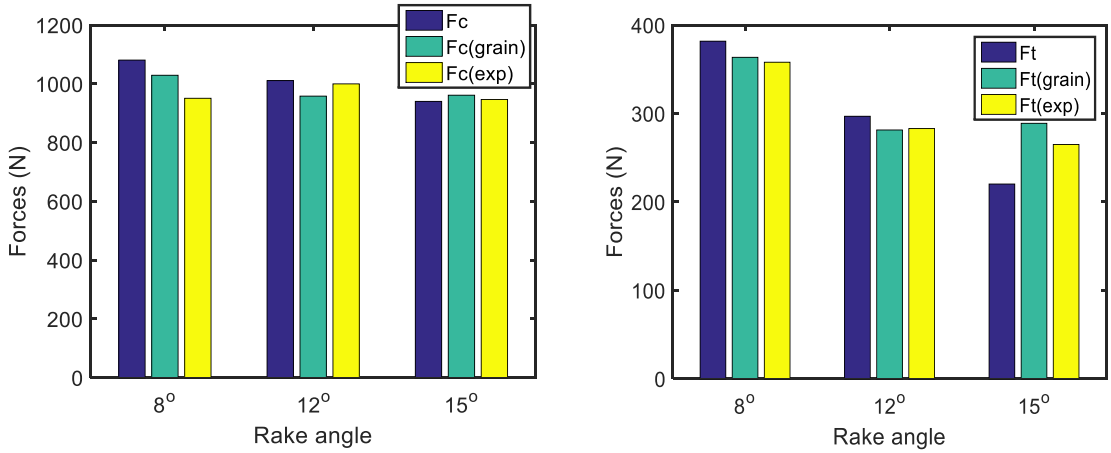

Figure 28 Cutting force F_c (a) and ploughing force F_t (b) at a depth of cut 0.153 *mm* with different rake angles

Table 8 Comparison of orthogonal turning force measurement and prediction at different depth of cut

Depth of cut (*mm*)	0.0254	0.0508	0.1016	0.1524
F_C (classic model)/*N*	261.76	435.59	749.95	1081.02
F_C (grain model)/*N*	248.53	409.66	767.60	1029.34
F_C (Experiment)/*N*	243	286	657	9521
F_t (classic model)/*N*	225.15	261.01	303.44	381.81
F_t (grain model)/*N*	213.76	245.51	360.04	363.56
F_t (Experiment)/*N*	186	194	254	358

Table 9 Comparison of orthogonal turning force measurement and prediction at different rake angle

Rake angle/^{o}	8	12	15
F_C (classic model)/*N*	1080.02	1011.15	940.47
F_C (grain model)/*N*	1029.34	958.35	961.46
F_C (experiment)/*N*	951	1000	947
F_t (classic model)/*N*	381.81	296.91	220.28
F_t (grain model)/*N*	363.56	281.41	288.94
F_t (experiment)/*N*	358	283	265

5.1.3 3D Machining experiment

The 3D oblique turning experiments were used to validate the 3D machining force prediction capability of the model. The turning experiments were conducted on an Okuma CNC lathe machine for the oblique turning force model validation. Kennametal TPG322 type ceramic inserts with a nose radius of 0.793 *mm* was used. The insert was mounted on a Hertel CTAP type tool holder to enable a 0^o rake angle and 45^o inclination angle. The tool holder was fixed on a Kistler dynamometer for the turning force measurement. The depth of cut was fixed at 0.5 *mm*. The cutting speed was selected to be 100 *m/min*. By varying the feed rate, two different feed rates 0.254 *mm/rev*, and 0.508 *mm/rev* were used to investigate the effect of feed rate on turning forces. The machining experiments were conducted under the dry cutting conditions.

5.1.4 3D turning force model

For the three-dimensional (3D) oblique turning, the orthogonal turning could be used by assuming an inclination angle. The side cutting angle C_S* could be obtained by a geometric translation [140]. Also, the equivalent depth of cut t* and width of cut W* could be calculated as,

$$t^* = f \cos C_S^* \quad (30)$$

$$w^* = \frac{w}{\cos C_S^*} \quad (31)$$

The resulting cutting forces from the inclined angle could be calculated as

$$P_{cut} = k \cdot w^* [\cos(2\eta)\cos(\phi - \gamma + \eta) + (1 + 2\theta + 2\gamma + \sin(2\eta))\sin(\phi - \gamma + \eta)] \cdot CA \quad (32)$$

$$P_{thrust} = k \cdot w^* [(1 + 2\theta + 2\gamma + \sin(2\eta))\cos(\phi - \gamma + \eta) + \cos(2\eta)\sin(\phi - \gamma + \eta)] \cdot CA \quad (33)$$

The cutting forces F_C, F_T, F_R shown in figure could be given as

$$F_C = F_{cut} + P_{cut} \quad (34)$$

$$F_T = F_{thrust} + P_{thrust} \quad (35)$$

$$F_R = \frac{F_C(\sin i - \cos i \sin \alpha_n \tan \eta_c) - F_T \cos \alpha_n}{\sin i \sin \alpha_n \tan \eta_c + \cos i} \quad (36)$$

With geometrical transformation as shown in Fig. 29, the cutting forces could be obtained from the above equations. A further geometric translation need to be conducted forces in the cutting, feed, and the axial directions, as

$$P_1 = F_C \quad (37)$$

$$P_2 = F_T \cos C_S^* + F_R \sin C_S^* \quad (38)$$

$$P_3 = F_T \sin C_S^* - F_R \cos C_S^* . \quad (39)$$

The predicted turning forces and measured forces data is listed in Table 10. The predicted turning forces in all three directions show a close approximation to the experimental measurement, as shown in Figure 30. By increasing the feed rate, the forces in all three directions will have obvious increase, as indicated in the experimental data in Fig. 30 (b). The trend is also well captured by the model prediction. The predicted ploughing forces F_P are consistently smaller than the experimental measurement. This discrepancy could be attributed to the horn radius effect. The cutting force F_C is largely dependent on the tool edge radius. The predicted trend for F_C closely follow the experimental measurement.

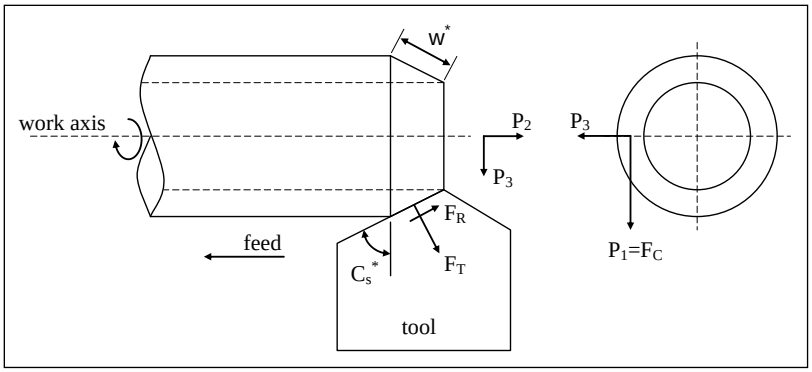

Figure 29 Schematic diagram of the 3D oblique turning [141]

(a) (b)

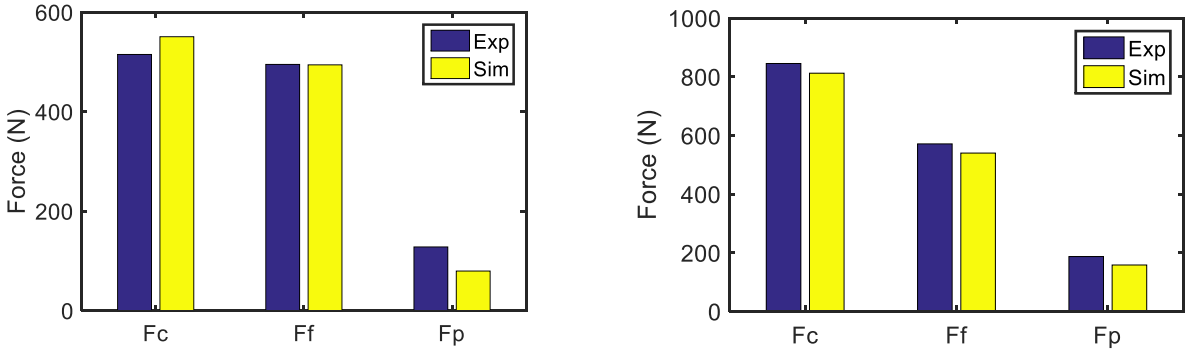

Figure 30 Comparison of 3D machining forces at feed rate of 0.254 *mm/rev* (a), and 0.508 *mm/rev* (b)

Table 10 Comparison of 3D oblique turning force measurement and prediction at different feed rate

Feed rate/ *mm/rev*	0.254	0.508
F_C (classic model)/N	515	1011.15
F_C (grain model)/N	550.67	958.35
F_C (experiment)/N	495	1000
F_t (classic model)/N	494.1	296.91
F_t (experiment)/N	128	281.41
F_t (grain model)/N	79.53	283

5.2 Residual stress modeling

5.2.1 Introduction

Residual stress profiles on the machined surfaces of parts greatly influence service properties such as fatigue life and corrosion resistance [142, 143]. Near surface compressive residual stress to increase fatigue life and corrosion resistance while tensile residual stress tends to adversely accelerate the initialization and growth of micro-cracks [144]. Subsequent heat treatment is required to remove the tensile residual stress. Control of residual stress on machined surfaces becomes critically important in various machining processes [145]. In precision machining of thin structures, the dimensional accuracy, fatigue life, and distortion are of top concern [146]. So the precision machining would require the residual stress could be predetermined in which the above requirements could be controlled.

Residual stress induced during machining processes are directly influenced by tool geometry, such as rake angle or clearance angle, and process parameters such as cutting speed, feed rate, and depth of cut. Early understanding for the machining induced residual stress primarily comes from experimental investigation. Liu et al. [147] concluded that the governing parameters of machining induced residual stress near the surface are the cutting edge and shear plane length in orthogonal turning. More specifically, Henriksen et al. [148] found that both thermal and mechanical mechanisms play important roles in residual stress generation. Additionally, Okushima et al. [149] demonstrated that mechanical loading mainly contributes to the compressive residual stress, while thermal effects contribute to the generation of tensile residual stresses. The workpiece material properties also have profound influence on the residual stress profile on machined surface. For example, AISI 316L steel tends to have compressive residual stress on the surface [136], while

the machined surface of AISI 4304 steel, the residual stress has been found to be tensile [150]. Additionally, the surface hardness also could influence the residual stress in machining as is discussed by Matsumoto et al. [151].

Titanium alloys, especially *Ti-6Al-4V*, have been widely used in medical and aerospace industry due to their high strength-to-weight ratio. The residual stress generation in the machined product is critical to the service functionality. Extensive research work has been conducted on the machining induced residual stress investigation of *Ti-6Al-4V*. Özel et al. [77] proposed a finite element model to predict residual stress in turning of *Ti-6Al-4V*. Sun et al. [74] experimentally investigates surface residual stresses of *Ti-6Al-4V* in end milling. Microstructure evolution has been observed on machined surfaces of titanium. Hughes et al. [152] reported phase transformation and elongated grain structures in the surfaces of *Ti-6Al-4V* after turning. Song et al. [153] observed dynamic recrystallization in titanium alloys during hot forming. Modified JC flow stress models have been used to capture the grain growth induced material softening effects. However, those models are essentially based on the mathematical interpolation with no physics-based parameters.

In this current study, an analytical model is proposed to predict residual stress formation in *Ti-6Al-4V* induced during machining by considering material dynamic recrystallization effects. The recrystallized volume fraction is calculated based on Johnson-Mehl-Avrami-Kolmogorov (*JMAK*) recrystallization model. The average grain size is obtained from grain growth and nucleation. The Hall-Petch relation is introduced to relate the average grain size with the material yield strength. The modified JC model is used to describe the material flow stress as a function of strain, strain rate, temperature, and average grain size. From the McDowell hybrid algorithm, the residual stress profile is determined on a machined workpiece from the stress history considering the thermal, mechanical, and microstructural evolution effects. Residual stress data from the

archival literature is used for model validation on orthogonal turning. The effect of depth of cut and rake angle on residual stress profile are investigated.

(a) (b)

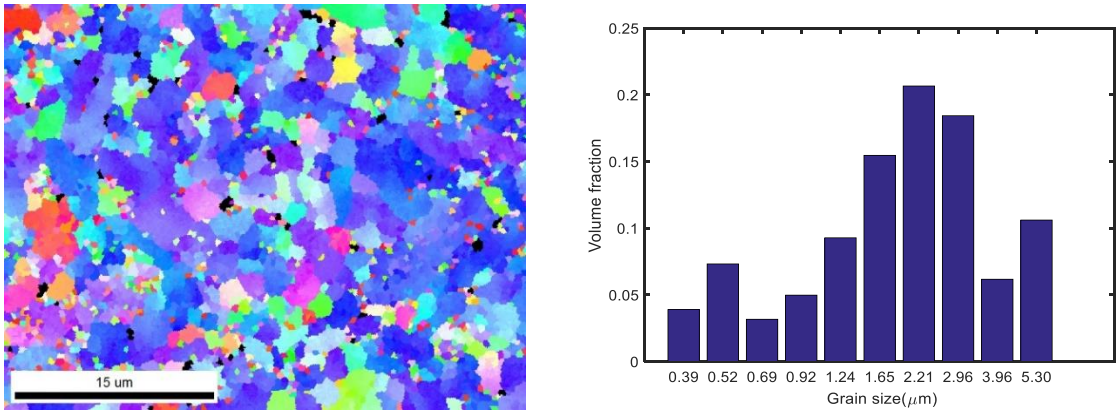

Figure 31 EBSD image of the raw material microstructure state, (a) the grain size distribution of the α phase, (b) the histogram of the α phase grain size.

5.2.2 Residual stress modeling

The initial material microstructure is characterized with EBSD, as shown in Fig. 31. During the machining process, the residual stress comes from the severe thermo-mechanical loading and material microstructural state change. Heat generated in the machining process can have significant influence on the residual stress profile. The heat comes from the primary shear zone and tertiary shear zone between the tool and workpiece. To calculate the temperature field induced by the deformation in the shear zone, an imaginary moving heat source approach is used [154], as shown in Fig. 32.

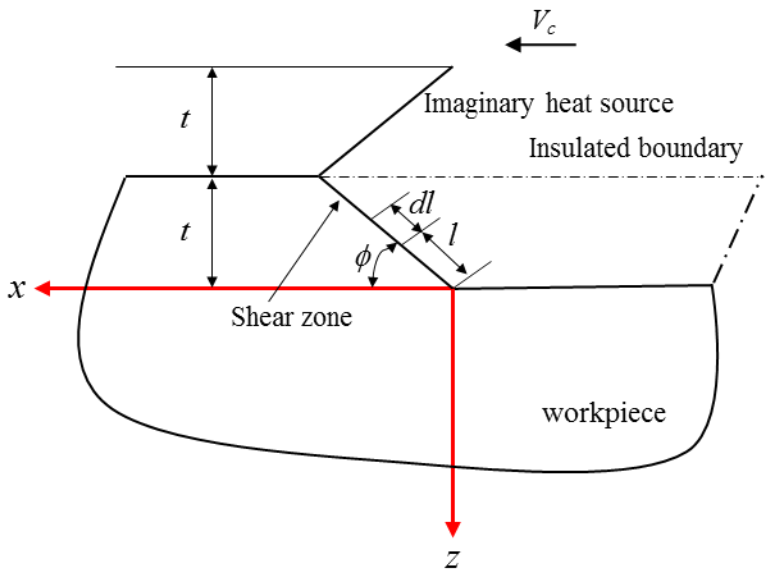

Figure 32 Heat transfer model in the shear zone.

The temperature rises in the workpiece due to shear deformation is the combined effects from the shear heat source and imaginary heat source, which can be obtained as,

$$\Delta T_{shear}(x,z)=\frac{V_c q_s}{4\pi k a}\int_0^L K_0\exp\left(-\frac{(x-l\sin\varphi)V_c}{2a}\right)\left(\sqrt{(x-l\sin\varphi)+(z-l\cos\varphi)}+\sqrt{(x-l\sin\varphi)+(z+l\cos\varphi)}\right)dl \quad (40)$$

where L is the shear length, $L=t/\sin\phi$, ϕ is the shear angle, t is undeformed chip thickness, $\varphi=\phi-\pi/2$, V_c is the cutting speed, a is the workpiece thermal diffusivity, k is workpiece thermal conductivity, K_0 is the modified second Bessel function. The average shear stress in the shear zone can be approximated as,

$$q_s=\frac{V_c(F_c\cos\phi-F_t\sin\phi)\cos\alpha}{wt\cos(\phi-\alpha)\csc\phi} \quad (41)$$

With a similar method, a moving heat source can be used to represent the generated heat in the rubbing zone, as shown in Fig. 33. To satisfy the insulated boundary condition on the workpiece surface, an imaginary heat source is imposed as coinciding with the original rubbing heat generation. The temperature rise induced by the tool workpiece rubbing can be calculated as,

$$\Delta T_{rub}(x,z)=\frac{\gamma V_c q_r}{2\pi k_w a_w}\int_0^{CA} K_0\exp(-\frac{(x-s)V_c}{2a_w})\sqrt{(x-s)^2+z^2}\,ds \quad (42)$$

where *CA* is the work-dead zone interface length which is calculated using Walforf's slip line model [155]. γ is heat partition coefficient that transferred to the workpiece.

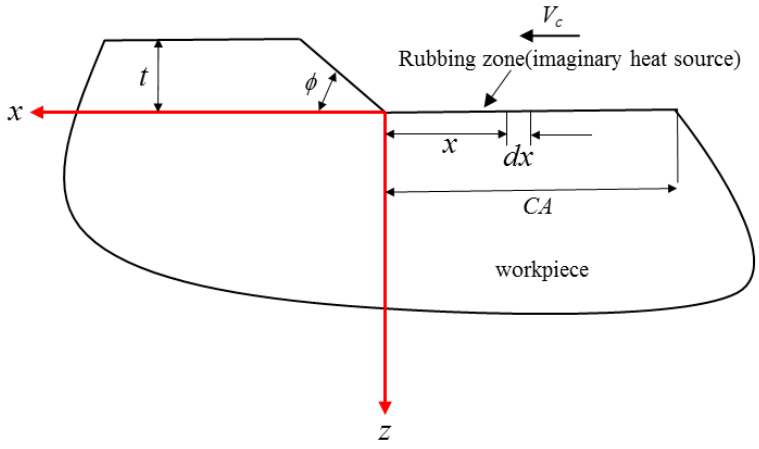

Figure 33 Heat transfer model in the tool-workpiece tertiary shear zone.

According to Barber, the heat partition could be calculated as,

$$\gamma=\frac{\rho_w c_w\sqrt{k_w}}{\rho_w c_w\sqrt{k_w}+\rho_{tool}c_{tool}\sqrt{k_{tool}}} \quad (43)$$

where the subscript ρ_w, c_w and k_w are the workpiece material density, heat capacity and thermal diffusivity respectively. ρ_w, c_w and k_w are corresponding the tool properties. The rubbing stress q_r is determined from the plowing force in the cutting direction F_C as

$$q_r=\frac{F_C V_c}{w(CA)}. \quad (44)$$

The thrusting force F_t can be calculated from traditional cutting mechanics [156], w is the width of cut. The total temperature rise in the workpiece can be obtained by superimposing the two temperature effects from rubbing and shear as,

$$\Delta T=\Delta T_{shear}+\Delta T_{rub} \quad (45)$$

In the 2D orthogonal turning process, the machining forces can be obtained from Oxley's contact mechanics theory, which has been investigated in a previous paper [130]. The equivalent normal stress field $p_1(s)$ and shear stress $q_1(s)$ are the used to represent the mechanical loading in the rubbing zone, as shown in Fig. 34.

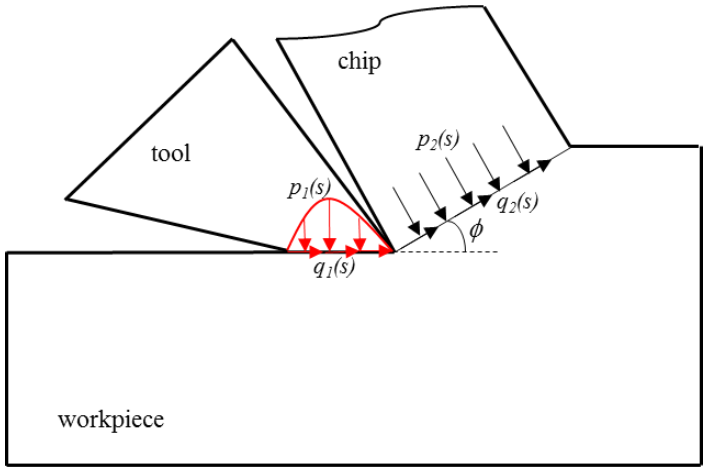

Figure 34 Simplified load for stress field calculation.

Similarly, $p_2(s)$ and $q_2(s)$ are used to represent loading in the shear zone. The residual stress in the machining process is determined from the stress history of the workpiece. In the orthogonal turning, the coordinate system is established in Fig. 35. With a plane strain assumption, the stress in the *y*- direction is assumed to be zero. The A simple rolling/sliding contact is assumed between the cutting tool the workpiece. The equivalent stress loads from the tool-workpiece interface and shear zone are accounted for in the stress field calculation. By integrating the stress load with a Boussinesq integration scheme, the stress field can be described as [136],

$$\sigma_{xx} = -\frac{2z}{\pi}\int_{-l_1}^{l_1}\frac{p_1(s)(x-s)^2}{[(x-s)^2+z^2]^2}ds - \frac{2}{\pi}\int_{-l_1}^{l_1}\frac{q_1(s)(x-s)^3}{[(x-s)^2+z^2]^2}ds$$

$$\sigma_{zz} = -\frac{2z^3}{\pi}\int_{-l1}^{l_1}\frac{p_1(s)(x-s)^2}{[(x-s)^2+z^2]^2}ds - \frac{2z^2}{\pi}\int_{-l_1}^{l_1}\frac{q_1(s)(x-s)}{[(x-s)^2+z^2]^2}ds \quad (46)$$

$$\sigma_{xz} = -\frac{2z^2}{\pi}\int_{-l_1}^{l_1}\frac{p_1(s)(x-s)}{[(x-s)^2+z^2]^2}ds - \frac{2z}{\pi}\int_{-l_1}^{l_1}\frac{q_1(s)(x-s)^2}{[(x-s)^2+z^2]^2}ds$$

where l_1 is the half tool-workpiece contact length in the rubbing area. The normal $p_1(s)$ stress load and shear stress load could be determined from the thrust force, F_t, and cutting force, F_c, respectively. A similar strategy can be used for the stress field calculation induced by the shear zone using $p_2(s)$ and $q_2(s)$ [157]. To superimpose the two stress fields, the ϕ angle clockwise rotation is required to translate the shear zone stress into the *x/y*- coordinate system.

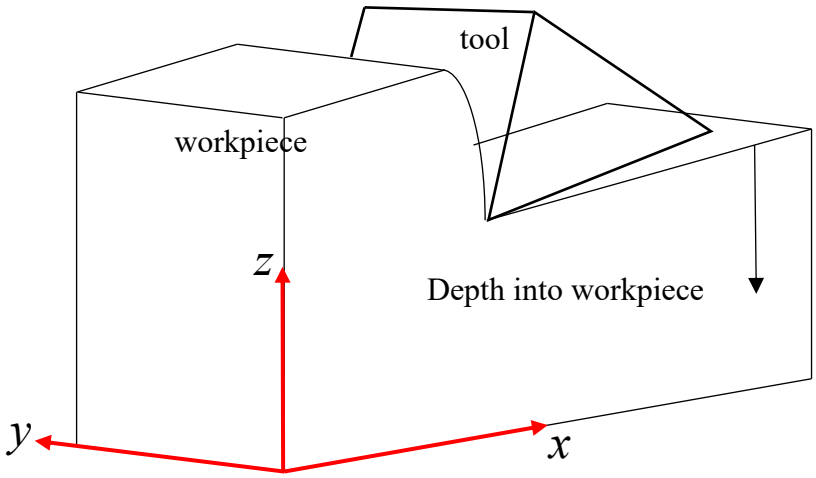

Figure 35 Schematic diagram showing the residual stress coordinate system.

The hybrid McDowell Algorithm [158] is used for the residual stress calculation. Both the elastic and plastic deformation are involved. The modified *JC* model is used for the yield stress calculation. The yield surface is described by a von-Mises yield criterion by accounting for the kinematic hardening,

$$F = \frac{3}{2}(S_{ij} - \alpha_{ij})(S_{ij} - \alpha_{ij}) - k^2 = 0 \quad (47)$$

where S_{ij} is the devitoric stress, α_{ij} is the devitoric back stress. The devitoric back stress evolution is defined as

$$\dot{\alpha}_{ij} = < \dot{S}_{mn} n_{mn} > n_{ij} \quad (48)$$

where < > is the MacCauley bracket as, $<x>$ = 0.5(x + |x|), n_{ij} is the unit normal vector pointing outwards the yield surface $n_{ij} = \sqrt{3/2}\ (S_{ij} - \alpha_{ij})/R$.

A blending function is used defined as

$$\Psi = 1 - \exp(-\kappa \frac{3h_m}{2G}) \quad (49)$$

where κ is a constant, h_m is the modulus, G is the shear elastic modulus. In an elastic/plastic loading of the machining process, the strain rate in the cutting direction can be obtained as

$$\begin{aligned} \dot{\varepsilon}_{xx} &= \frac{1}{E}[\dot{\sigma}_{xx} - \nu(\dot{\sigma}_{yy} + \dot{\sigma}^*_{zz})] + \alpha\Delta T + \frac{1}{h}(\dot{\sigma}_{xx} n_{xx} + \dot{\sigma}_{yy} n_{yy} + \dot{\sigma}^*_{zz} n_{zz} + 2\dot{\tau}^*_{xz} n_{xz}) n_{xx} \\ &= \Psi\left(\frac{1}{E}[\dot{\sigma}^*_{xx} - \nu(\dot{\sigma}_{yy} + \dot{\sigma}^*_{zz})] + \alpha\Delta T + \frac{1}{h}(\dot{\sigma}^*_{xx} n_{xx} + \dot{\sigma}_{yy} n_{yy} + \dot{\sigma}^*_{zz} n_{zz} + 2\dot{\tau}^*_{xz} n_{xz}) n_{xx}\right) \end{aligned} \quad (50)$$

where α is the thermal expansion coefficient. By assuming a plane strain condition, the strain rate in the cutting transverse direction can be similarly expressed as

$$\dot{\varepsilon}_{xx} = \frac{1}{E}[\dot{\sigma}_{yy} - \nu(\dot{\sigma}_{xx} + \dot{\sigma}^*_{zz})] + \alpha\Delta T + \frac{1}{h}(\dot{\sigma}_{xx} n_{xx} + \dot{\sigma}_{yy} n_{yy} + \dot{\sigma}^*_{zz} n_{zz} + 2\dot{\tau}^*_{xz} n_{xz}) n_{yy} = 0 \quad (51)$$

Eq. (13) and (14) are simultaneously solved to get the stress rate increments $\dot{\sigma}_{xx}$ and $\dot{\sigma}_{yy}$. The integration is conduced along the loading path for the determination of the residual stress in the cutting direction σ_{xx} and transverse direction σ_{zz}.

5.3 Results and discussion

Considering the calculated machining forces and temperature field from Eq. (9), the elastic stress field could be obtained from Eq. (10). By integrating the stress field along the loading path

with Eq. (14), (15), the residual stress σ_{xx} and σ_{zz} were obtained. At a feed rate of 0.1 *mm/rev*, cutting speed of 26.4 *m/min*, depth of cut 0.1 *mm*, tool rake angle of 0^o and clearance angle of 7^o. The tool edge radius is 8 μm. Since in the machining process, the process parameters and tool configuration are kept the same. The residual stress on any point at the same depth is the same. The measurement is randomly picked from the data point on the machined surface. By removing the layer with electrochemical polishing, the residual stress underneath the surface could be measured. The predicted residual stress as a function of depth into the workpiece is plotted in Fig. 36. Also, the temperature contour on the workpiece near the workpiece tool interface is shown in Fig. 36 (b). The maximum predicted temperature goes up to around 500 ^oC. The stress is plotted in both cutting direction and transverse direction. Large tensile residual stress is predicted on the machined workpiece surface. The magnitude of the tensile residual stress sharply decreases to zero as the depth into the part increases and the stress state changes tensile to compressive. Around the depth of 15 μm, the compressive residual stress reaches a maximum value. After that, the magnitude of the compressive residual stress slowly decreases to zero at a depth around 0.1 *mm*. Under machining conditions used for this model, the resulting residual stress affected depth is around 100 μm. The general trend of the residual stress profile on the machining induced residual stress captured by the model as comparison with the experimental measurements from Ratchev et al. [159]. However, large discrepancy was found in surface residual stress predictions where the model predicts tensile residual stress, but the experimental measurements show the compressive residual stress. In most of the residual stress measurement on machining, the surface oxidation could be a very important reason that will contribute to the error. From the modeling side, the residual stress generation in the machining mainly comes from three sources, the un-uniform plastic deformation, the existing of the temperature gradient and the material phase transformation

induced residual stress. In the current model, the author only considers the first two sources. The phase transformation effect on the residual stress is ignored. Specifically, for the Ti-6Al-4V material, the α to β phase transformation would induce the volume increase. This will result in a more compressive residual stress on the surface. This would further explain fact that the model prediction tends to be more tensile than the prediction. Ramesh et al. [20] introduced a residual stress prediction model that accounts for the martensitic phase transformation effect. More advanced model would be required to capture those complicated microstructure evolution effect for the residual stress prediction. The peak compressive residual stress value show 8.03 % error in the cutting direction and 4.36 % error in the transverse direction.

(a) (b)

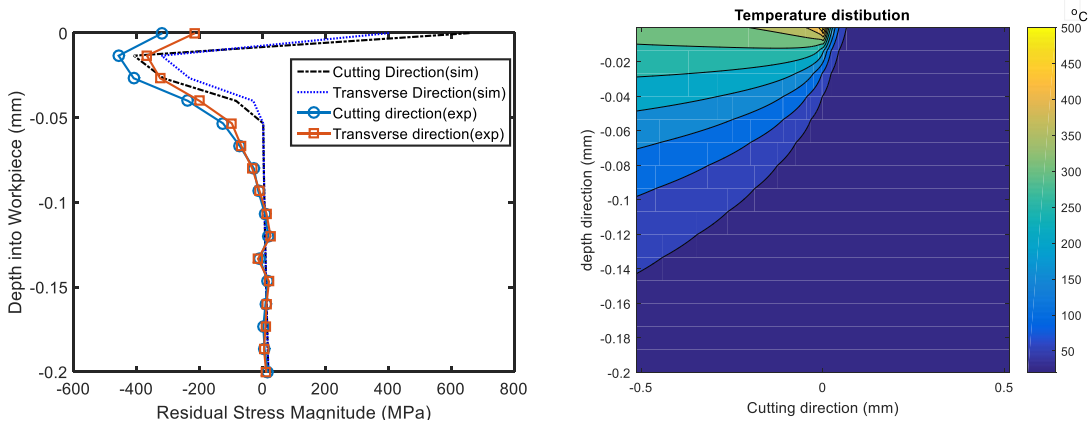

Figure 36 Prediction and measured residual stress (a) and workpiece temperature distribution (b) at a feed rate of 100 $\mu m/rev$, cutting speed 26.4 *m/min*, and depth of cut 100 μm.

(a) (b)

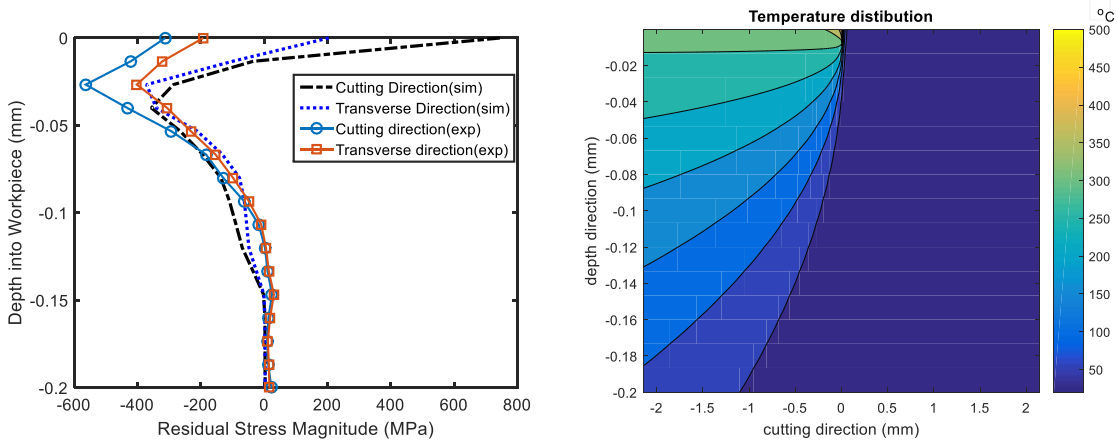

Figure 37 Predicted and measured residual stress (a) and temperature distribution on the workpiece (b) at feed rate 100 $\mu m/rev$, cutting speed 26.4 *m/min*, and depth of cut 500 μm.

A predicted residual stress profile using a cut depth of 0.5 *mm* is plotted in Fig. 37 (a). On the surface, the predicted residual stresses are still tensile in both transverse and cutting directions. Compared to the depth of cut at 0.1 *mm*, the residual stress in the transverse direction are less tensile when the depth of cut increases. The residual stress affected depth is increased slightly, which is around 0.15 *mm*. The prediction closely follows experimental measurements. The maximum predicted temperature is still around 500 ^oC. The peak value of compressive residual stress from the model prediction has 28.32 % and 1.49 % in the transverse direction. For the residual stress prediction model, the prediction error is at an acceptable level.

For the parametric study for the effect of different machining process parameters on the residual stress of *Ti-6Al-4V*, three more parametric studies are conducted. At a cutting speed of 0.5 *m/s*, depth of cut 0.1524 *mm*, and tool rake angle 8^o, the predicted residual stress as a function of depth into the workpiece is plotted in Fig. 38. The stress is plotted in both cutting direction and transverse direction. A compressive residual stress is found on the machined workpiece surface. As the depth into the workpiece increases, the magnitude of the compressive residual stress further

increases. Around a depth of 25 μm, the residual stress reaches it maximum value. After that, the magnitude of the compressive residual stress decreases. At a certain point, the compressive residual stress switches to tensile. The magnitude of the tensile stress is close to zero. The residual stress affected depth is around 75 μm beneath the machined surface.

By decreasing the rake angle from 15^o to 8^o, the predicted residual stress profile is plotted in Fig. 39. The residual stress in both directions are still compressive but the magnitude of the compressive residual stress is significantly decreased. A similar trend is followed as with a rake angle of 15^o. One more case is conducted by increasing the depth of cut to 0.3048 *mm*, as shown in Fig. 40. Compared with the depth of cut 0.1524 *mm*, the magnitude of the compressive residual stress has sharp decrease on the machined workpiece surface. The largest value of the compressive residual stress is slightly increased. The residual stress affected depth also increases up to around 100 μm. By reducing the rake angle from 15^o to 8^o, the surface magnitude of the compressive residual stress has sharp decrease, as shown in Fig. 38, 39. The smaller rake angle would result in more heat generation. This presence of the thermal effect would lead to a more tensile residual stress profile on the surface. Similarly, the increasing depth of cut also results in a more tensile residual stress profile on the machined surface, as compared by Fig. 38, 40.

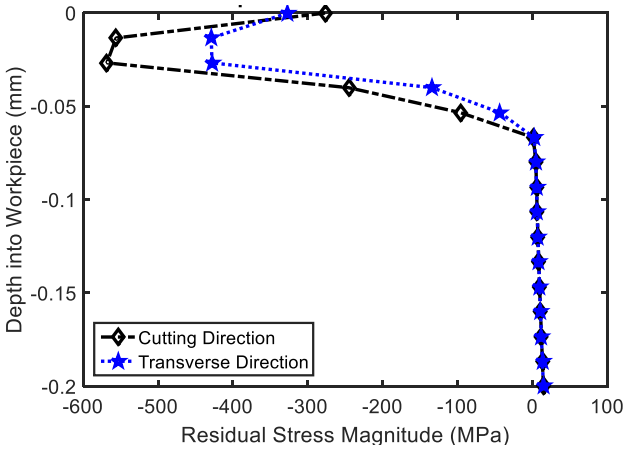

Figure 38 Residual stress prediction with a cutting speed 0.5 *m/s*, depth of cut 0.1524 *mm*, and rake angle of 15º.

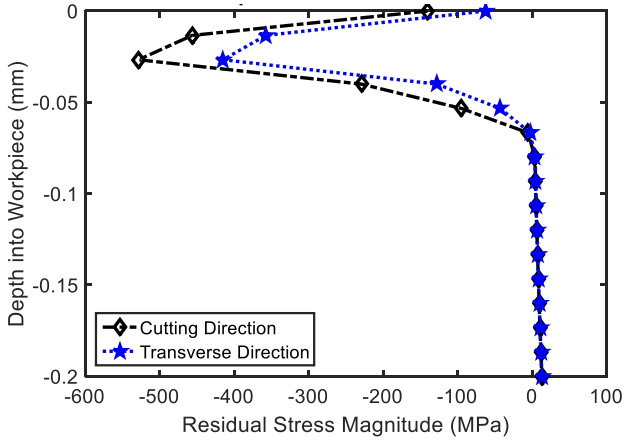

Figure 39 Residual stress prediction with a cutting speed 0.5 *m/s*, depth of cut 0.1524 *mm*, and rake angle of 8º.

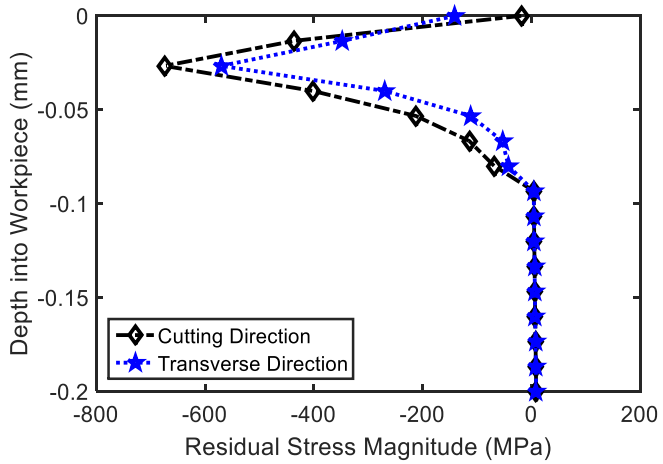

Figure 40 Residual stress prediction with a cutting speed 0.5 *m/s*, depth of cut 0.3048 *mm*, and rake angle of 15º.

5.4 Conclusion

By accounting for the dynamic recrystallization induced grain size evolution, an analytical model is proposed for the residual stress prediction in the orthogonal turning of *Ti-6Al-4V* material. The material grain size evolution in the dynamic recrystallization process is explicitly calculated in the turning process. A modified material flow stress model is developed by considering the grain size effect with the Hall-Petch relation. With the classic Oxley's contact mechanics theory, the mechanical and thermal loading are obtained. The hybrid McDowell algorithm is used for the residual stress prediction. Validation tests are conducted between the predicted residual stress and experimental measurement. Good agreements are found between model prediction and experimental data. With the validated analytical model, the residual stress profile on the machinated workpiece is predicted. The effects of tool rake angle, and depth of cut on residual stress profile are investigated. The proposed analytical model provides a more fundamental understanding of the effects material dynamic recrystallization on the cutting mechanics.

CHAPTER 6. LASER-ASSISTED MACHINING

6.1 Heat affected zone in laser assisted end milling

6.1.1 Introduction

The application for high strength and high temperature material, especially for nickel based alloys and titanium alloys, has enjoyed great increase over the past decades [80, 160, 161]. Inconel 718 is a so-called high temperature alloy which can retain its high strength the toughness at an elevated temperature up to 500 ^{o}C. The superior mechanical properties at high temperature make it one of the most widely used alloy in gas turbine application. However, the machining process of Inconel 718, which is called hard to machine material, imposes great challenges [162, 163]. The reason comes from the extremely large yield stress, even at elevated temperature, low thermal conductivity and large fracture toughness. The large machining forces would require large power input for the machining equipment, which would reduce the material removal rate. Also, the generated heat near the machine tool and workpiece interface would lead to severe tool wear. The built up edge, flank wear and notching wear are the typical tool wear types in the machining process of Inconel 718 [164, 165].

Extensive research has been devoted to overcome those limitations in the Inconel 718 machining process, such as electrical discharge machining [166, 167], cryogenically enhanced machining [168], jet assisted machining [169] and thermally enhanced machining [170, 171]. Among all those methods, the thermally enhanced machining provides an easy and cost-effective setup to improve the machinability of hard to machine material. An external heat source is required to preheat the workpiece material in front of the machining tool. The preheating process could help

to significantly reduce the material yield stress and machining induced heat generation. The laser beam or plasma could be used for the preheating, from which the spot size of the heating zone could be easily controlled [172, 173].

The laser assisted machining (LAM) for hard to machine material is originally introduced by Bass et. al [85]. The LAM makes it especially suitable for the precision machining process, where the manufacturing system stiffness and machine tool flexibility is the biggest challenge. By appropriate selection of the LAM parameters, such as laser beam spot size, power input and local preheating area, the strength of the workpiece material could be tremendously reduced. The consequent cutting forces and machining tool deflections will also be eliminated. The early research on the LAM includes its application to the machining of ceramics [167, 174]. Improvement of machined surface roughness and tool wear is reported [86]. Ding et. al [87] investigated the LAM for hardened steel. Significant improvement on the surface roughness in the hard turning of steels over traditional turning with an appropriate selection of the laser power input parameters was reported. The improvement of the surface roughness was mainly due to the reduced cutting force. Also, more compressive residual stress profile was observed on the laser assisted machined surface. Similar observation is reported by Chang et al [175]. A comprehensive study on the laser-assisted turning is conducted by Anderson et. al [79] at an economical aspect of view. The specific cutting energy and material removal rate are greatly improved when compared against the turning without laser preheating.

In addition to the machining configuration and cutting parameters, the LAM includes other parameters, such as laser spot size, laser power input and relative position of laser beam to the machine tool. The appropriate control of those parameters could help to improve the efficiency of laser power and machining efficiency. The characterization of laser generated temperature

distribution, which is called heat affected zone (HAZ), is crucial for the optimization of laser heating related parameters. A mathematical model is proposed by Tian et. al. [176] for the laser assisted orthogonal turning to predict the temperature field on the workpiece. A three-dimensional transient finite element model is developed by Rozzi et. al. [177] for the thermal response of silicon nitride workpiece in turning.

The current study will provide a physical understanding for the thermal response of the Inconel 718 workpiece material in the laser-assisted milling. The shape of HAZ induced by simple laser scanning will be experimentally measured and predicted by finite element modeling. The absorption ratio will be analyzed from the measured data and model prediction. The effect of laser scanning speed and laser power input on the material heat absorption ratio will also be investigated. A special coaxial laser preheating setup will be proposed for end milling. The temperature field prediction induced by a rotational laser scanning path will be provided. Parametric study will be conducted to investigate the effect of rotation speed on the temperature field.

6.1.2 Experimental

Experiments are conducted to characterize the temperature distribution induced by the moving laser beam on the workpiece surface. An Inconel 718 plate with a dimension of 200 $mm\times$ 100 $mm\times$ 2 mm is used. The initial surface roughness of the workpiece material Ra is 0.439. A YAG type laser system with a beam radius of 0.6 mm is used for the laser beam generation. The workpiece surface is in the focus plane of the laser. The laser beam with a fixed power input is scanning on the workpiece surface along the x- direction at a constant speed, as shown in the Fig. 41. The temperature of the preheating area is measured with thermal couples. Those thermal couples are located on the top surface of the workpiece, as shown in Fig. 43. To get the shape and

dimension of the HAZ along the laser beam moving path. The cross-section view of the laser moving path is imaged by a metallographic microscope. In a metallographic image, the melting zone has a sharp color contrast with the un-melting area. The boundary of the melting zone is indicated by the yellow line. The shape and cross section area of the melting zone are measured. Three different parameters are defined for the melting zone, those are width, depth and cross section area, as shown in Fig. 44.

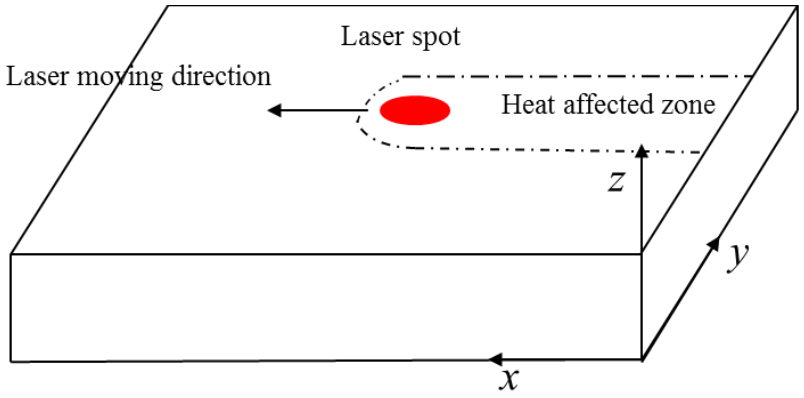

Figure 41 Schematic diagram for the laser preheating experiment.

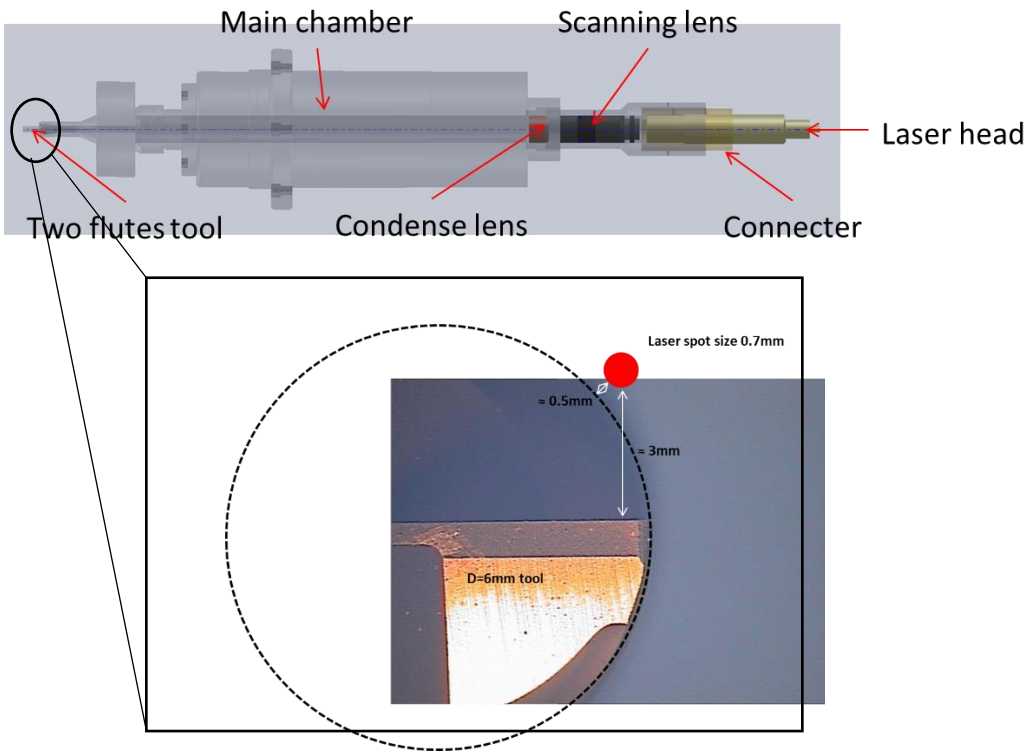

Figure 42 The schematic diagram of the coaxial laser milling tool setup.

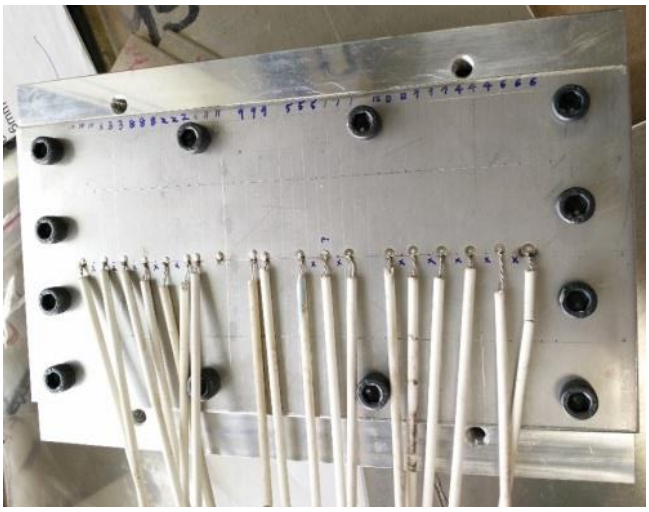

Figure 43 Temperature measurement of the melting zone.

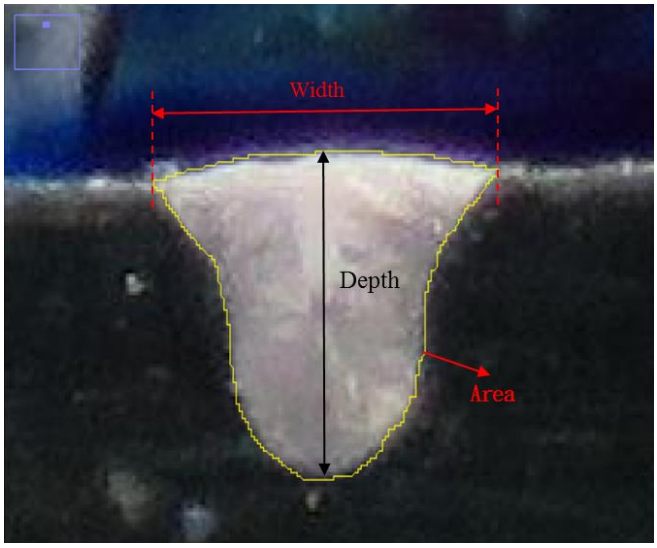

Figure 44 Three parameters defined to characterize the melting zone shape.

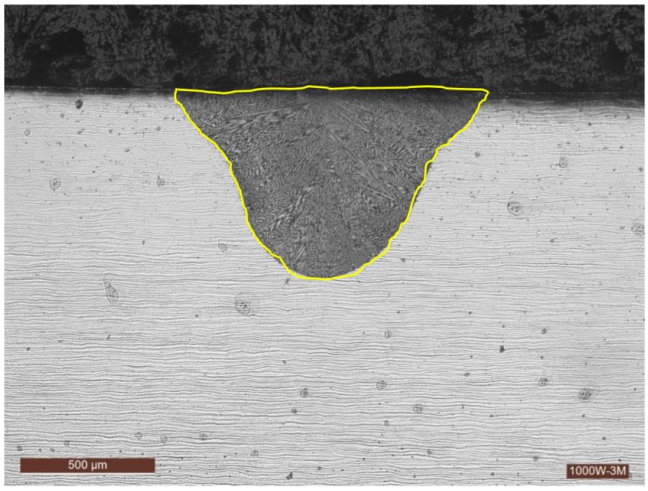

Figure 45 The melting zone shape with a laser power input of 1000 *W* and moving speed at 3000 *mm/min*.

The cross section of the heat affected zone with a laser scanning speed of 3000 *mm/min*, power input 1000 *W* and laser spot diameter 0.6 *mm* is shown in the Fig. 45. As indicated in the figure, the dark area which is above the yellow line, is the melting zone. The melting zone has a parabolic shape. The white area, which is next to the melting zone, is the heat affected zone in the laser scanning process. The material in this area is affected by the high temperature. Significant phase transformation or dynamic recrystallization may occur.

Different laser scanning speed and laser power input is used to investigate their effects on the melting zone shape. In the current study, three laser power input levels are selected as 400 *W*, 600 *W*, and 1000 *W*. The laser scanning speed ranges from 1000 *mm/min* to 9000 *mm/min*. The effects of laser power input and laser scanning speed on the melting zone area are shown in Fig. 46. The maximum melting zone area is achieved when the power input of 1000 *W* and scanning speed at 1000 *mm/min*. The melting zone area monotonically decreases with the increasing laser scanning speed. As can also be noticed, when the laser power input is between 400 *W* to 600 *W*, the melting zone area is a weak function of the laser scanning speed. When the power input is at 1000 *W* level, the melting zone area has sharp decrease with the increasing laser scanning speed. The effects of power input and laser scanning speed on melting zone depth are plotted in Fig. 47. A similar trend for the effects of laser scanning speed and laser power input on melting zone depth is found. The largest melting zone depth is found to be around 1.375 *mm* when the laser input is 1000 *W* and laser scanning speed is 1000 *mm/min*. The maximum width of the melting zone is determined to be 1.446 *mm*, as shown in Fig. 48.

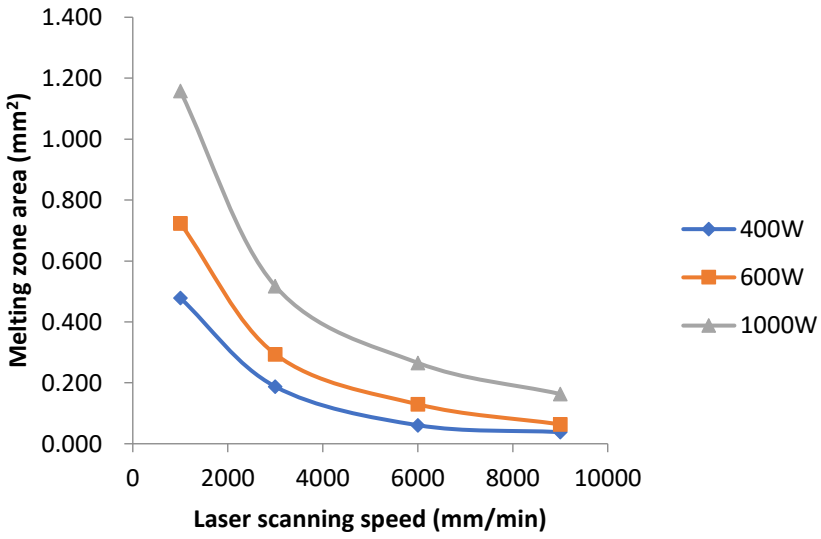

Figure 46 Effects of Laser scanning speed and power input on the melting zone area.

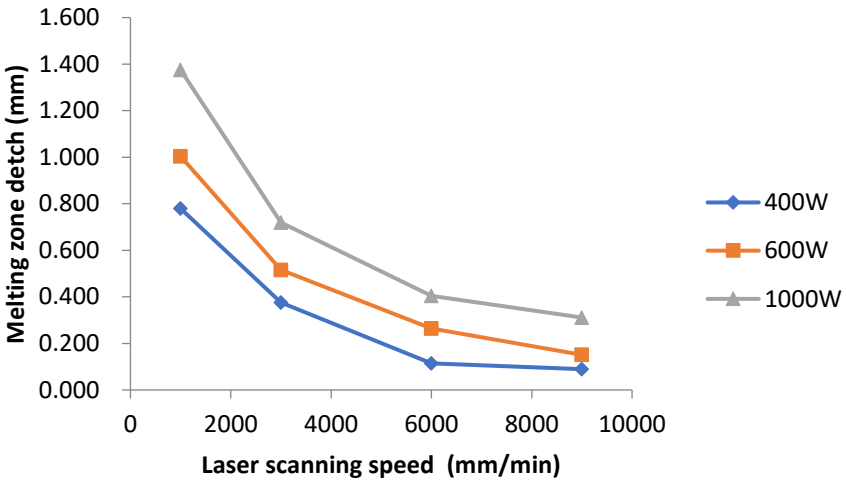

Figure 47 Effects of laser scanning speed and power input on melting zone depth

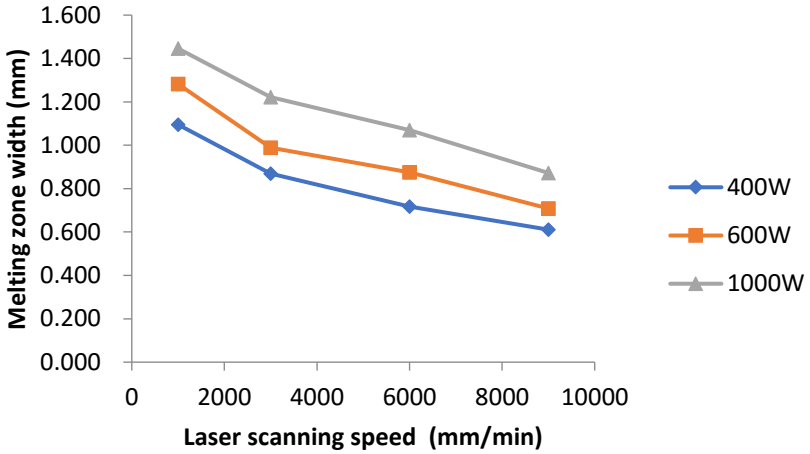

Figure 48 Effects of laser scanning speed and power input on the melting zone width

6.1.3 Temperature field modeling

Table 11 Thermal properties of Inconel 718

Density (kg/m^3)	8190
Heat capacity $J/(kg{\cdot}^oC)$	$0.2T\ (^oC) + 421.7$
Thermal conductivity $W/(m{\cdot}^oC)$	$0.015T\ (^oC) + 11.002$
Melting temperature (^oC)	1300
Latent heat (J/kg)	227000

The laser power distribution on the laser beam focus plane is described by the Gaussian equation, as

$$q(x,y)=\frac{2Q}{\pi r^2}\exp(-\frac{2(x^2+y^2)}{r^2}) \quad (52)$$

where Q is the laser total power input, r is the laser spot radius. With a laser power input of 400 W and laser spot diameter of 0.6 mm, the power density distribution is shown in the Fig. 49. The thermal conductivity and specific heat capacity of the Inconel 718 material are dependent on the temperature. The melting temperature of the Inconel 718 is in the range of 1260 -1336 ^oC.

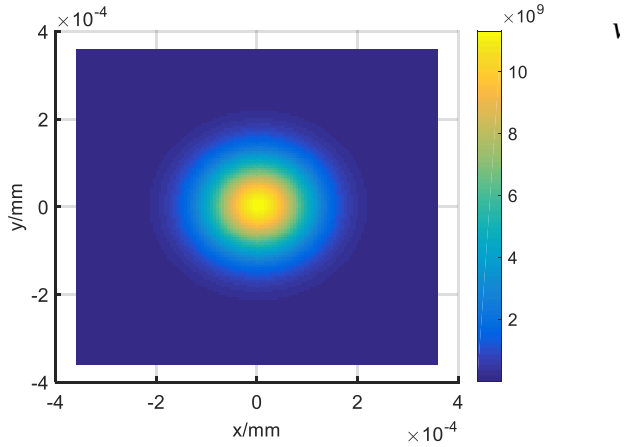

Figure 49 Power distribution of laser beam with total power input 400 W and laser spot diameter 0.6 mm.

In this study, 1300 ^oC is selected as the melting temperature for Inconel 718. All those thermal properties are summarized in the Table 11 [79, 178]. The three-dimensional heat transfer in a rectangular plate could be described by

$$\rho c_p(\frac{\partial T}{\partial t}+V_l\frac{\partial T}{\partial x})=\nabla(k\nabla T)+\dot{q} \quad (53)$$

where ρ is the material density, c_p is specific heat, k is thermal conductivity, V_l is the laser power moving speed in the x- direction, q is the power generation per unit volume. The absorption ratio defines the ratio of workpiece material absorbed energy to the total amount of laser power input,

which is dependent on the material thermal properties, laser wavelength, surrounding air heat convection. The boundary condition on the laser heating surface is defined as

$$k\frac{\partial T}{\partial z} = q(x,y) - h(T - T_0) - \sigma\varepsilon(T^4 - T_0^4) \quad (54)$$

where $q(x,y)$ laser power input, h is the heat transfer coefficient, σ is the thermal radiation coefficient, ε is the material emissivity, T_0 is the reference temperature. The initial condition could be denoted as

$$T(x,y,z,0) = T_0 \quad (55)$$

In the simulation, the workpiece boundary condition is specified in Fig. 50. An analytical method is proposed by Yang et al. [179] with comparison to experiments for the absorption ratio determination to match the maximum temperature.

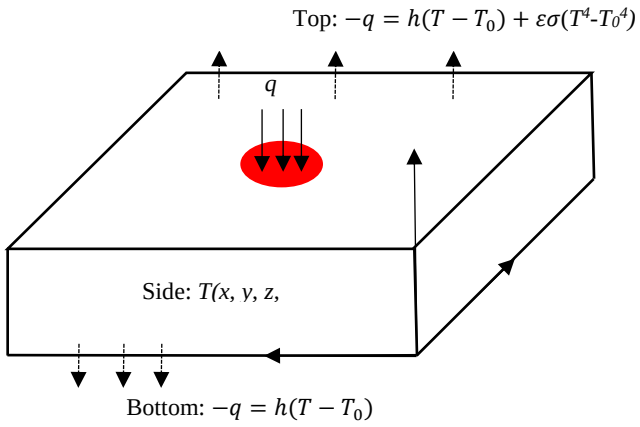

Figure 50 The boundary condition.

In our current study, a new method is developed by optimizing the melting zone shape. The absorption ratio is determined by matching the simulated melting zone shape with that measured from preheating experiments. The absorption ratio is a function of laser power input and laser scanning speed. With the increase of laser moving speed, the absorption ratio will slowly decrease.

However, when the laser power input increases from 400 *W* to 1000 *W*, the absorption ratio has sharp decrease. The material absorption ratio in the laser scanning process depends on lots of factors, such as the input laser wavelength, material thermal properties, surface texture properties, workpiece material temperature, and surrounding environment heat convection et al. In the current study, we found that the material absorption ratio would decrease as the increasing laser scanning speed and the laser power input. In terms of the laser scanning speed, the absorption ratio has only slight decrease in all three cases. The decreasing material absorption ratio could be attributed to the increasing heat convection from the surrounding air flow. Similar results are reported in the work of Ricciardi et al. [180], where the material absorptivity is found at a relatively higher welding speed. However, when the laser power input increases from 600 *W* to 1000 *W*, the energy efficiency has as much as 43.59 % decrease. At the laser power input of 1000 *W*, significant amount of laser heating area changes to the liquid state, this could attribute to the decreased material heat absorptivity. Additionally, the higher laser energy input would result in much higher workpiece temperature around the laser scanning point. The larger temperature different between the environment and workpiece would promote faster heat convection. The laser preheating efficiency diagram could be very useful in terms of the laser assisted machining experiment design. In the laser assisted milling of silicon nitride, Pfefferkorn et al. [181] reported that the laser preheating efficiency has sharp decrease with higher laser power input. In a different study by Yang et al. [179] for the laser assisted milling of titanium alloy, the laser energy absorptivity also shows obvious decrease with increasing workpiece plate temperature. From an analytical side, the absorption ratio could be obtained as

$$\xi = \frac{k(T_s - T_0)}{2Q}\sqrt{\frac{\pi^3 r^3 V}{2a}} \qquad (56)$$

where T_s is the workpiece top surface temperature in the center of laser beam, a is the material thermal diffusivity, which is 2.9×10^6 m^2/s. The absorption ratio calculated with this method is in the range of 0.25 to 0.41 as the variation of different laser scanning speed and power input. In most of the previous research work, typically a constant material absorption ratio is selected. For example, in the work of Catherine et al. [182], the material absorptivity is determined to be around 0.2 for the Inconel 718 material. In the current study, we assume that the material absorption ratio is dependent on the laser power input and laser scanning speed. The material absorption ratio is determined from the laser straight scanning experiment. The material absorption ratio data will be used in the rotational laser scanning for the temperature field prediction.

6.1.4 Results and discussion

The temperature distribution on the workpiece surface are predicted from ANSYS. The top view and cross section view of the temperature field from the center of laser beam are shown in Fig. 51 (a, b). In this case, the laser power input is selected as 400 *W*, laser scanning speed at 6000 *mm/min* and laser spot diameter of 0.6 *mm*. The maximum temperature from the prediction 1558 ^oC, is even higher than the melting temperature of Inconel 718. This is validated by the uneven workpiece surface when the laser beam passes over the heat affected zone. Also, the magnitude temperature gradient in the *z*- direction is very large, which indicates the sharp temperature decrease in the workpiece depth direction. When the laser scanning at the speed of 9000 *mm/min*.

(a) (b)

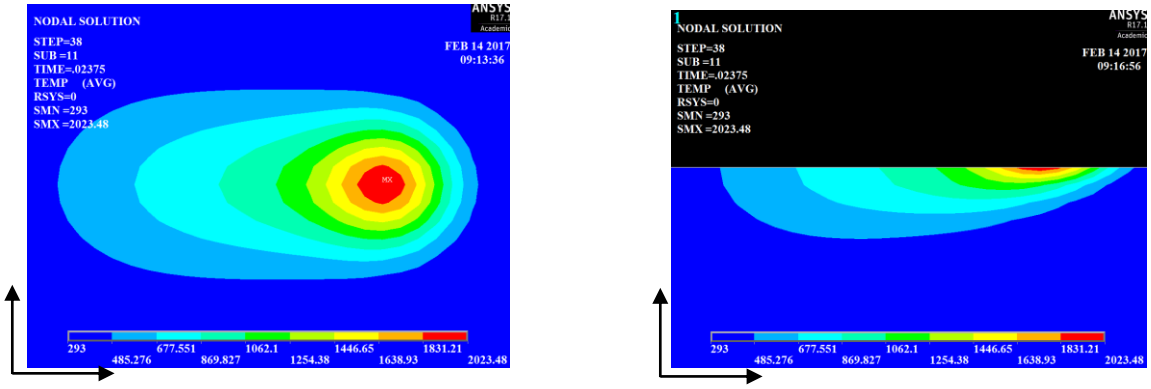

Figure 51 Cross section view (a) and cross section view (b) of the temperature field with a laser power input of 400 *W* and laser scanning speed 6000 *mm/min* (Temperature is in the unit of *K*).

The workpiece bottom surface temperature history, which is located 2 *mm* away from the laser beam heating center is plotted as a function of time shown in Fig. 52 at different laser power input. The temperature sharply increases when the laser spot approaches the measurement point and slowly decreases to the room temperature. When the laser power input decreases from 1000 *W* to 400 *W*, the peak temperature has slight decrease from 53 ^{o}C to 44 ^{o}C. The predicted temperature history profiles agree well with the measurement.

(a)

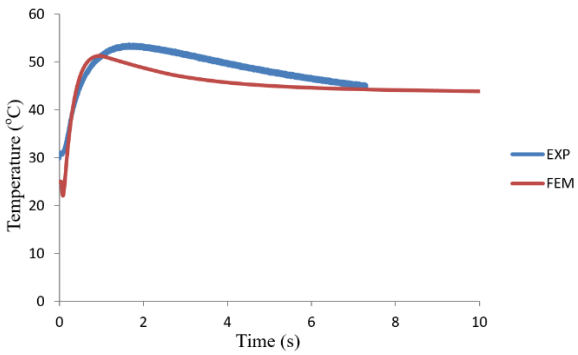

(b)

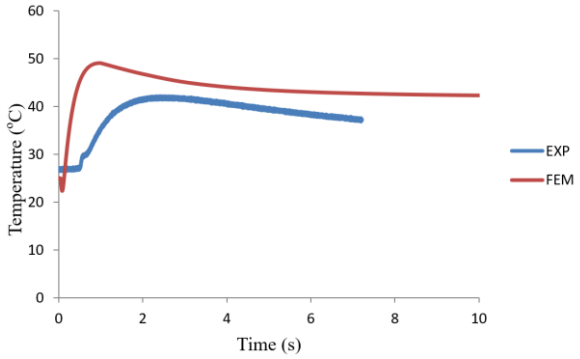

(c)

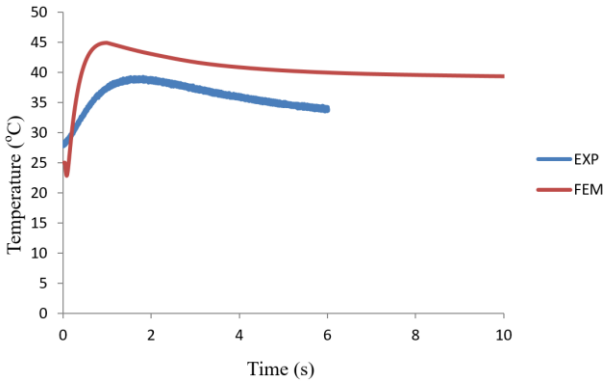

Figure 52 Comparison of surface temperature between experiment and FEM modeling at laser scanning speed 9000 *mm/min*, when laser power input is (a) 1000 *W*, (b) 600 *W*, and (c) 400 *W*.

In our current study, a coaxial laser preheating system is used for the laser-assisted end milling process. The first attempt to use coaxial laser preheating was proposed by Brecher et al. [183]. Instead of heating the whole workpiece, a local heating scheme is introduced. So significant thermal loading could be reduced in the milling processes. Also, the machining flexibility could be greatly improved. In addition to the translation in the *x*- direction, the laser is rotating along with the workpiece in the milling process at a constant angular speed, as shown in Fig. 53. The

laser is assumed to be rotating along a circle with a 2 *mm* radius. The laser induced preheating temperature is predicted at a laser power input of 400 *W*, *x*- directional scanning speed 1000 *mm/min*, and a rotational speed of 3500 *rpm*. The top view and cross section view of the predicted temperature field are shown in Fig. 54 (a, b). The maximum predicted temperature in this case is 463 ^{o}C, which is below the material melting temperature. The heat penetration depth is about 0.95 *mm*. As can also be noticed from the temperature distribution in the *x/y*- plane, the heat affected are in the *x/y*- plane is much larger than pure *x*- directional scanning. To further investigate the rotational speed on the temperature distribution, the rotational speed is increased to 7000 *rpm*. The predicted temperature field is shown in Fig. 54 (c, d). The highest temperature decreases to 231 ^{o}C. Also, more uniform temperature along the circular area is observed.

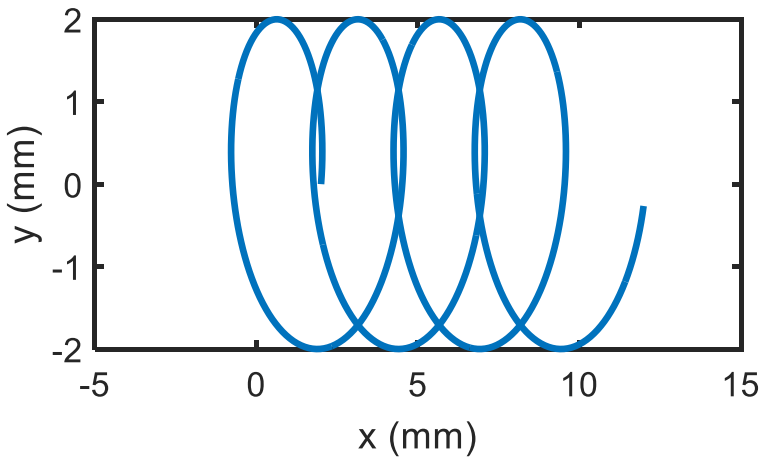

Figure 53 Schematic diagram of rotational laser scanning path.

(a) (b)

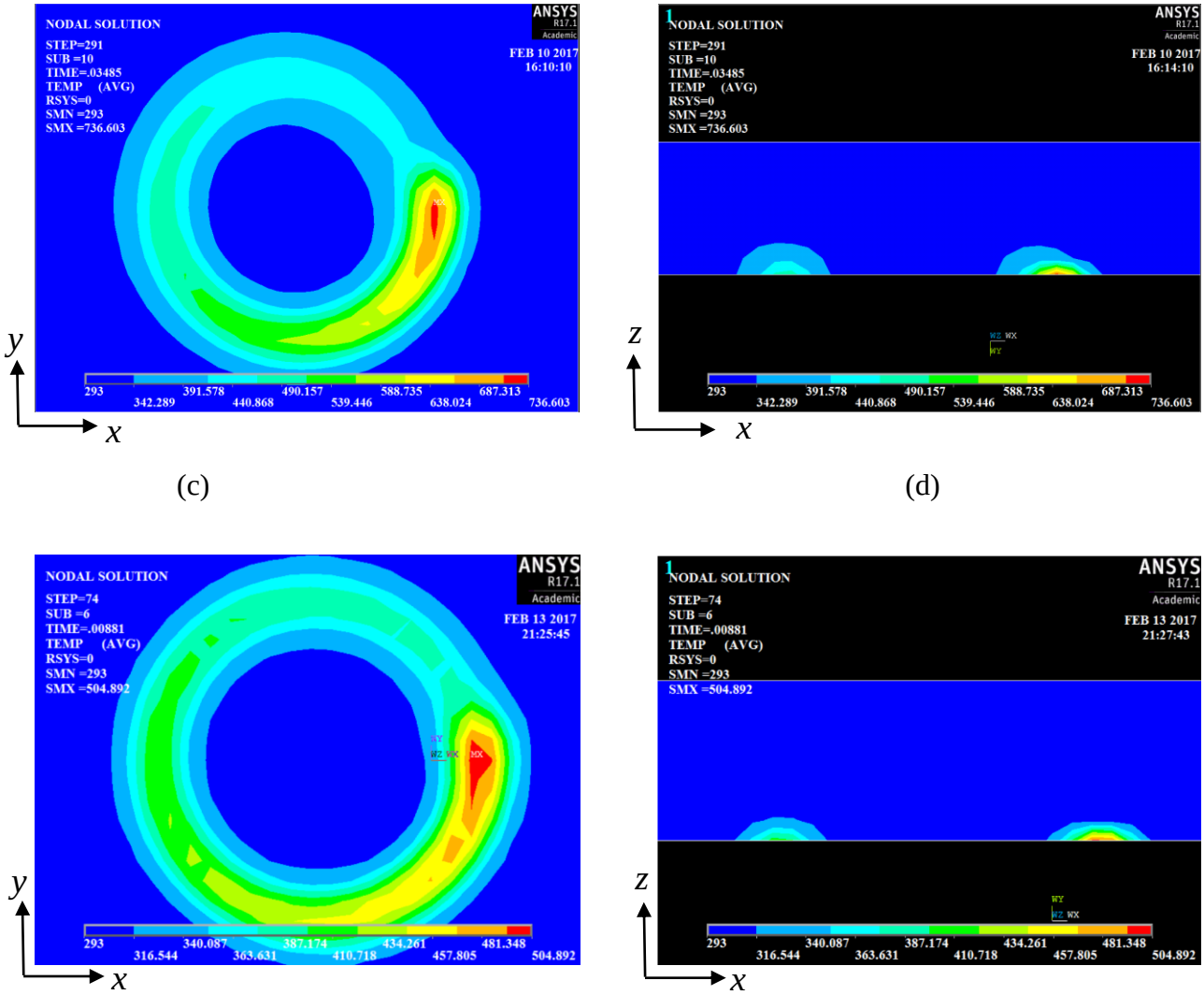

(c) (d)

Figure 54 Top section view (a) and cross section view (b) of temperature field induced by a laser rotating at laser rotational speed of 3500 *rpm*; Top section view (c) and cross section view (d) at rotational speed of 7000 *rpm*, with a 0.2 *mm* radius and *x*- directional moving speed 1000 *mm/min* (Temperature is in the unit of *K*).

Compared with the straight laser scanning, the laser preheating spot size needs to cover the whole end milling tool area, which requires a laser spot size dimeter close to the milling tool. In the laser rotational set up, the laser only locally preheats the workpiece material near the cutting flutes. Since the three shear zones mainly attribute to the milling force, which is near the cutting

flutes. This local preheating set-up will achieve comparative material softening effect with much higher efficiency.

6.1.5 Conclusion

The temperature distribution and HAZ in the laser-assisted milling of Inconel 718 is experimentally investigated. A three-dimensional finite element model is developed for the temperature field prediction. The predicted temperature fields show close approximation to the experimental measurements. The absorption ratio is determined by matching the simulated melting zone shape with the experimental characterized melting zone shape. Parametric study is conducted for the effects of laser scanning speed and power input on the absorption ratio. The effects of laser power input and laser scanning speed on the melting zone shape are also investigated. The melting zone area monotonically decreases with the increasing laser scanning speed. The increased laser power input could help to increase the melting zone area. As an application, the finite element model is used for the coaxial laser preheating system temperature distribution prediction.

6.2 Force Prediction in Laser-assisted Milling of Inconel 718

6.2.1 Milling force model

The milling force model could be extended from orthogonal cutting force model by geometrical transformation. For each cutter, the milling process could be treated as a 3D oblique turning with an inclination angle equal to the helix angle of the milling tool, as shown in Fig. 55 [184]. Compared to orthogonal cutting, an external force component F_R exits from the inclination angle i, which could be described as

$$F_R = \frac{F_C\left(\sin i - \cos i \sin \alpha_n \tan \eta_c\right) - F_T \cos \alpha_n \tan \eta_c}{\sin i \sin \alpha_n \tan \eta_c + \cos i} \quad (57)$$

where η_c is the chip flow angle, equals to the inclination angle i ; α_n is the inclination angle to be determined. The inclination angle *i* in end milling equals to the tool helix angle. An equivalent cutting model could be used to transform the oblique cutting to the orthogonal cutting condition to get the cutting forces F_C, F_R, F_T. Those predicted cutting forces are than transformed back to the milling forces components in the cutter feed, radial and tangential directions P_1, P_2, P_3, described by

$$\begin{aligned} P_1 &= F_C \\ P_2 &= -F_T \cos\left(C_S^*\right) - F_R \sin\left(C_S^*\right) \\ P_3 &= F_T \sin\left(C_S^*\right) - F_R \cos\left(C_S^*\right) \end{aligned} \quad (58)$$

where C_s^* is the equivalent side cutting edge rake angle [185]. After the calculation of forces on each flute, another transformation would be required to get the milling forces in the workpiece coordinate system. The forces from each flute are summed up to get the total force as a function of the milling tool rotation angle, as

$$\begin{aligned} F_X(\Psi) &= \sum_{j=1}^{N_t} \left(P_{1j} \cos \Psi_j + P_{2j} \sin \Psi_j\right) \\ F_Y(\Psi) &= \sum_{j=1}^{N_t} \left(-P_{1j} \sin \Psi_j + P_{2j} \cos \Psi_j\right) \\ F_Z(\Psi) &= \sum_{j=1}^{N_t} P_{3j} \end{aligned} \quad (59)$$

where $\Psi_j(t) = \omega t$ is the emersion angle of the *j-th* flute, ω is the angular velocity of the milling tool.

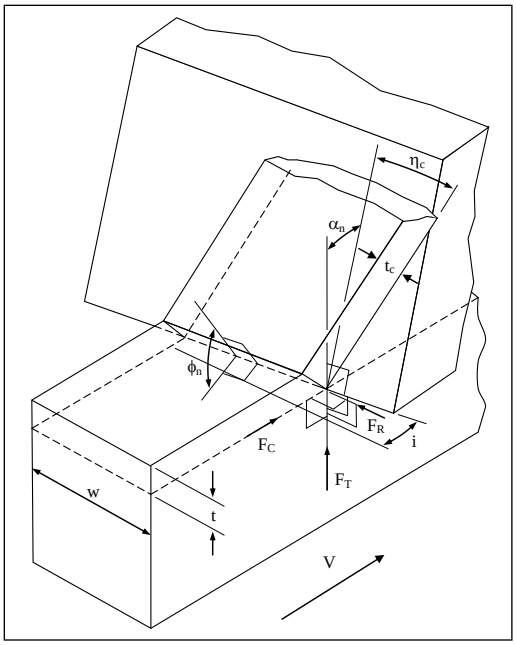

Figure 55 Oblique cutting model [22]

6.2.2 Experimental setup

To validate the proposed milling force model, experimental force measurements are conducted. To effectively heat the workpiece in the milling process, a coaxial laser-milling tool setup is designed. In the milling process, the laser is moving with the milling tool in both *x*-direction and rotational direction. The radius of the laser spot is characterized to be 0.6 *mm*. The distance between the laser and tool is measured to be 0.7 *mm*. Before the cutting force measurement, thermal couples are used to get the temperature distribution of the workpiece material. The workpiece material is mounted on the Kistler three component dynamometer for the milling force measurement. The voltage signal from the dynamometer is processed by a three-channel amplifier. A Labview code is developed for the real-time milling force measurement. A two-flutes tungsten carbide end milling tool with titanium aluminum nitride coating is used in the current study (JSK, 2182001, Taiwan). The tool radius is 6 *mm*. The tool has a rake angle of 27º, helix angle 45º, and corner radius 10 μm. The tool spindle speed is kept constant at 3500 *rpm* in the whole experiment.

Different depth of milling and feed speed are used to investigate their effects on the milling forces. Also, the milling forces at the same machining conditions without the laser heat are measured for the comparison.

6.2.3 Results and discussion

6.2.3.1 Temperature distribution

The laser beam is moving along the *x*- direction on the workpiece with a power input of 400 *W* at different speeds. The width and depth of melting zone are measured. A finite element model is developed for the temperature distribution prediction induced by the moving laser heat source on the workpiece. The power distribution of the laser beam follows the Gaussian distribution

$$q(x,y) = \frac{2Q}{\pi r^2}\exp(-\frac{2(x^2+y^2)}{r^2}) \qquad (60)$$

where Q is the total laser power input, r is the radius of the laser beam. To get the material heat absorption ratio, an iterative produce is conducted by matching the melting zone in the finite element model with the experimental measurement. The material absorption ratio is determined to be 0.3 in the current study. The temperature distribution induced by a moving laser heat source on the workpiece is shown in Fig. 56. The temperature of the interface between the solid/liquid is defined by the melting temperature of the Inconel 718, which is about 1300 ^oC. The measured temperature contour is in good agreement with the predicted temperature contour, as shown in Fig. 57. Also, the melting zone shape at different cutting speed is measured as plotted in Fig. 58, 59. Both the width and depth of the predicted melting zone shape is slight larger than experimental measurement data. This could be explained by the ignoring of the latency heat of Inconel 718 in the finite element model.

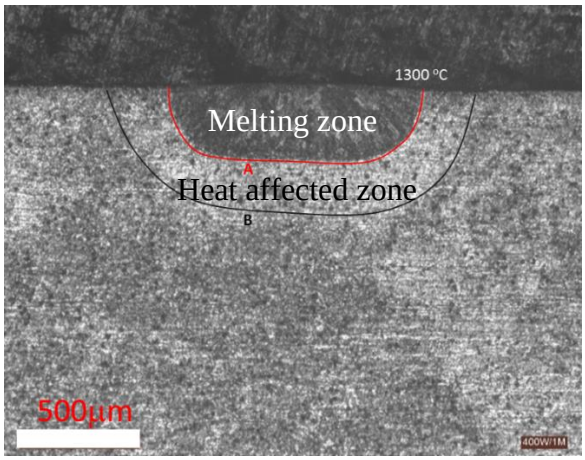

Figure 56 The measured temperature contour of Inconel 718 workpiece with 400 *W* laser power input and 1000 *m/min* moving speed with a laser spot size of 0.6 *mm*.

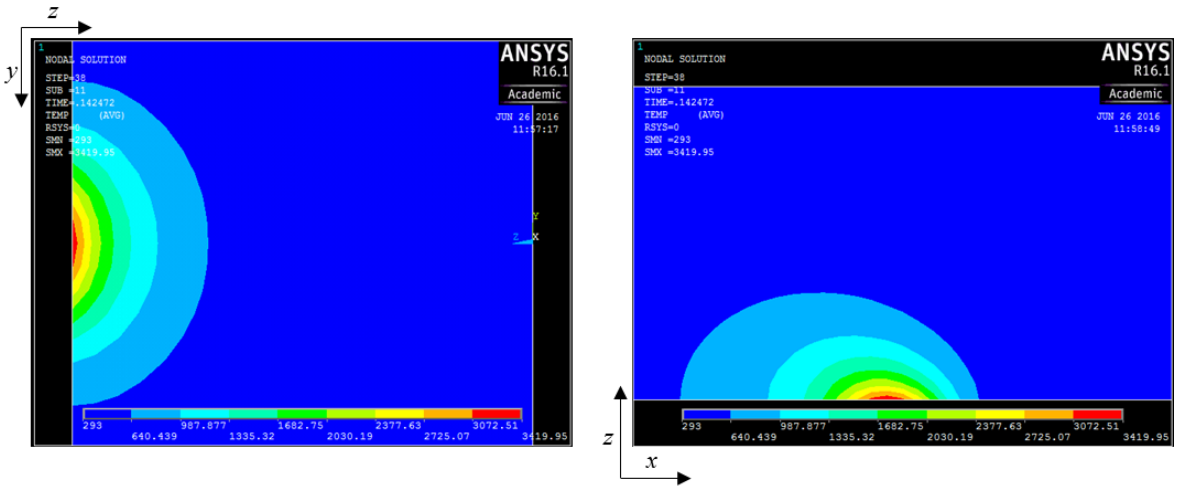

Figure 57 Project views of the temperature distribution of Inconel 718 workpiece with 400 *W* laser power input and 1000 *m/min* moving speed with a laser spot radius of 0.6 *mm*.

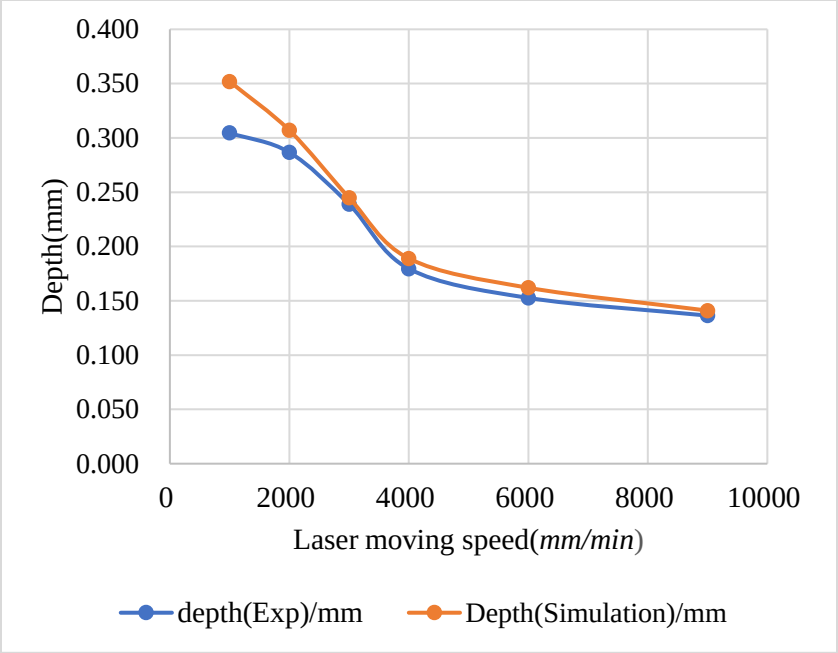

Figure 58 The melting zone depth as a function of laser moving speed.

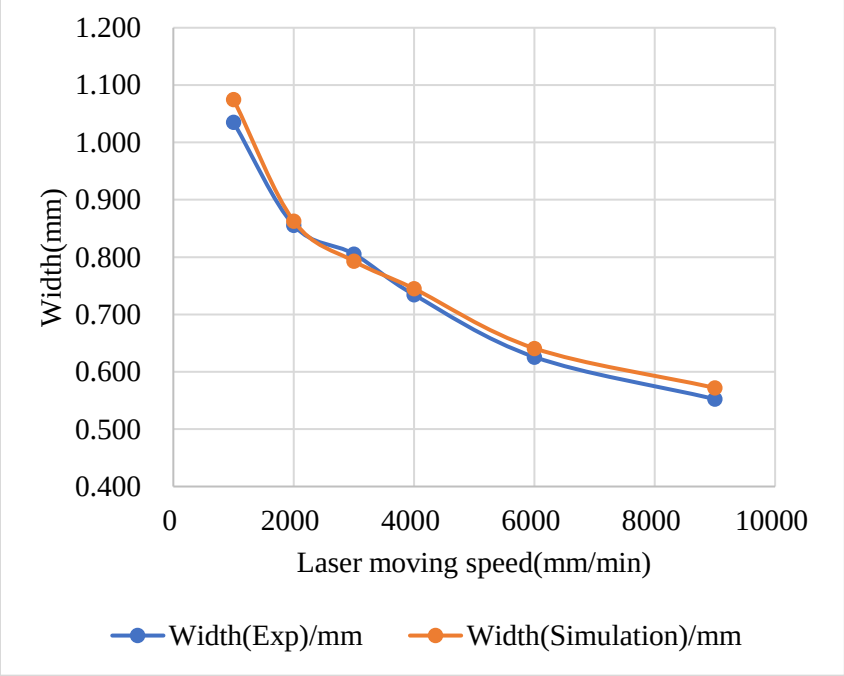

Figure 59 The melting zone width as a function of laser moving speed.

In the actual milling environment, the laser power input is selected as 200 *W*, the radius of the laser spot is 0.7 *mm*. With the validated temperature field prediction model, the temperature

field is predicted at a different laser power input and scanning speed for the machining force calculation. At the laser power input of 400 *W*, the softened workpiece material strongly adhered to the tool. The measured force did not correctly reflect the machining forces and showed large fluctuation. So, the laser power input was reduced to 200 *W* in our milling force measurement experiment. Since our temperature field predicted model was validated by different laser scanning speed and spindle speed. The predicted temperature field at a different laser power input and scanning speed is still believed to be reliable. The laser is rotating with the tool at the angular speed of 3500 *rpm*. A secondary translational movement along the *x*- direction at the speed of 250 *mm/min* are applied. In our current milling experiment, the axial depth of cut is around 30 μm. So, we can simply assume a uniform temperature distribution along the depth direction in the workpiece. With the above developed model, the preheating temperature is determined to be 300 ^oC at the tool cut edge area.

6.2.3.2 Milling forces

After the preheating temperature field is determined, the milling force model takes the temperature field as input for the milling forces prediction. The tool rotational speed is selected as 3500 *rpm*. The axial depth of cut is 35.7 μm. The radial depth of cut is 3 *mm*, which means half of the tool is immersed into the workpiece. The tool is moving along the *x*- direction at a constant speed of 250 *mm/min*. This would give an average feed of 50 μm per flute. The milling forces measurements from experiments are listed in Fig. 60. The milling force prediction for the single period is plotted, as shown in Fig. 61. The largest milling forces in the *x*- direction with and without laser preheating both are around 5 *N*. The laser effect on the *x*- directional force reducing is not obvious. When it comes to the force in the *y*- direction, the largest force reduces from 14 *N* to 5 *N*.

In the *z*- direction, the largest milling force without laser is around 20 *N*. There is a sharp decrease from 20 *N* to 10 *N* when the laser is added. The magnitude and shape of the predicted milling forces profile in three different directions are in good agreement with the measured forces. Also, at the same milling conditions, the milling forces without laser preheat are measured. The forces in all three directions have significant decrease with an appropriate preheating procedure.

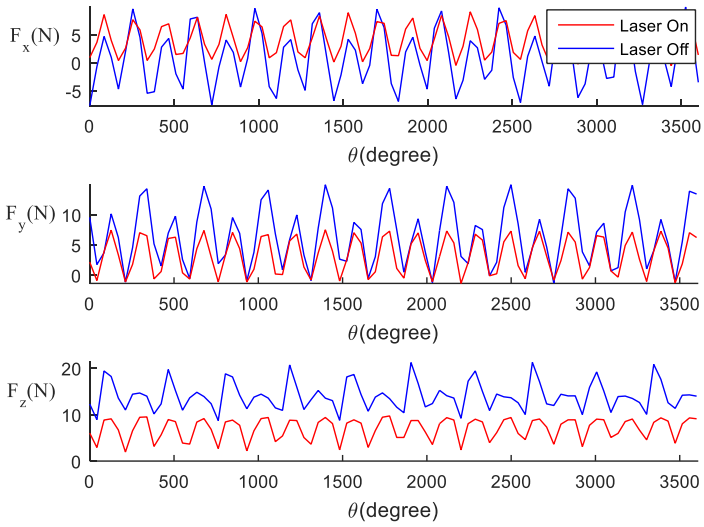

Figure 60 The milling forces at feed speed 250 *mm/min*, spindle speed = 3500 *rpm*, radial depth of cut = 3 *mm*, axial depth of cut = 0.0357 *mm*.

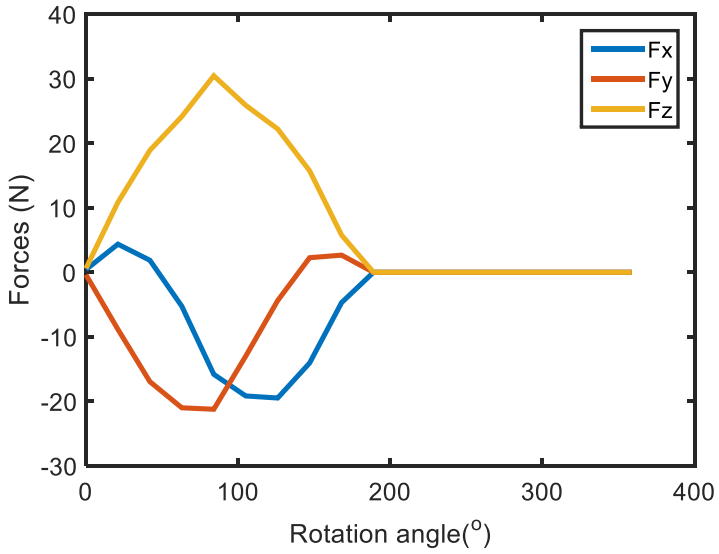

Figure 61 The predicted laser assisted milling forces at the *x*- direction moving speed 250 *mm/min*, spindle speed = 3500 *m/min*, radial depth of cut = 3 *mm*, axial depth of cut = 0.0357 *mm*.

Table 12 Johnson-Cook parameters for Inconel 718

A(MPa)	B(MPa)	C	m	n	T_{melt} (^{o}C)
980	1370	0.02	1.03	0.164	1300

Table 13 Mechanical properties of Inconel 718

Young's modulus (*GPa*)	211.97- 0.0624*T*
Poisson's ratio	0.28

To further investigate the temperature effect on the milling process, the specific cutting energy at different cutting conditions are analyzed. Compared with the conventional milling process, the specific cutting energy drops by more than 20%. The effect of feed speed and depth of milling on specific cutting energy is negligible.

6.2.4 Conclusion

An analytical model is developed for the forces prediction in the laser assisted milling processes. The calculation is performed by transforming the milling configuration into an inclined 3D turning condition. The modified Oxley's contacting theory is used for the shear stress distribution calculation on the chip. An iterative procedure is implemented for the shear angle determination. Laser preheating induced temperature distribution is obtained by finite element simulation in *ANSYS*. The temperature field and milling conditions are taken as the input for the force calculations. Experimental measurements are conducted for the model validation. Good agreement is found between the predicted milling force and the experimental data. The imposed preheating temperature field could help to significantly reduce the cutting force and specific cutting energy in milling process. The proposed forces prediction model provides a cost-effective way for the laser assisted milling process optimization.

CHAPTER 6. CONCLUSION AND FUTURE WORK

6.1 Conclusion

The detailed implementation of the material microstructure affected machining modeling framework has been summarized in the above work. The model takes the material properties, machine tool configuration and process parameters into consideration. The direct output could be machine tool related tool wear, material removal rate, and the end-product surface integrity properties, such as residual stress, microstructure states, surface roughness, and microhardness. The empirical model is capable of the machining induced microstructure evolution prediction based on extensive experimental data, where the regression analysis could be conducted to establish this relationship. However, this empirical model suffers from the inflexibility, which requires repeated experimental data given any slight change on the machining conditions or material system. Staring from the basic mechanics and microstructure evolution principles, the physical model could serve as a universal modelling method. The physical based model which quantitatively calculates the microstructure evolution in the machining process has been numerically implemented for the grain size and phase transformation calculation. Challenges still exist in terms of more microstructure attributes inclusion, such as dislocation density, texture information. Complicated material system, such as steel alloys, requires more comprehensive model. The physical based model bears more physical meanings which provide the insights on the material microstructure, mechanics and thermal interactions in the machining process.

The material microstructure property is an important consideration in the machining process. Both the material mechanical properties and machined surface integrity are directly related to the material microstructure attributes. This research work reviews the recent

development of machining process with a material microstructural consideration. A comprehensive computational modeling framework could be developed to predict the machined part microstructural related properties by taking the cutting parameters, machine tool configuration and raw material selection as the input. On the other hand, given the machined part application with a specific material microstructure requirement, a reverse modeling approach would be necessary to trace back to all possible combinations of the process parameters, raw material selection and machining tool configuration. Previous machining process optimization work mainly focuses on the design of experimental based regression analysis. The current work aims to review the machining process modeling approach with material microstructure consideration and point out some useful guidelines for the physical based inverse modeling method for the machining process design. The following conclusions are given in the thesis.

- The microstructure evolution in the primary shear zone includes elongated grain structure and phase transformation. The chip morphology dominated by the phase transformation and micro-crack propagation in the shear zone.
- The microstructure change in the shear zone is typically modeled as strain softening or high temperature softening, which will help to reduce the machining forces.
- Modified JC model is developed to include the microstructure attributes (grain size, dislocation, phase composition) in the material flow stress model.
- The residual stress profile is influenced by machining process parameters. The stress-free surface could be generated by appropriate selection of machining process parameters.
- The co-axial laser assisted milling setup could achieved an improved energy efficiency with the local preheating method. The FEA model could accurately predict the temperature field and heat affected zone induced by the rotational laser preheating.

- The laser assisted milling could help to significantly reduce the milling force in the axial direction and milling tool feeding transverse direction. The analytical milling force model for laser assisted milling gives a good approximation to the experimental force measurement, which could be applied for the laser assisted milling process design and optimization.

6.2 Future work

In addition to the grain size and phase composition, the material microstructure evolution in the machining process covers a wide range of microstructure properties, such as grain morphology, dislocation density, grain boundary et al. As noted in the current study, the precision machining simulation framework only consider the average grain size, and volume fraction of the phase composition. More advanced microstructure prediction modeling would be required to more accurate prediction. Another limitation for the grain size evolution is that, the JMAK model is based on the isotheral assumption. In the really machining condition, temperature gradient might exist on the shear zone, which would induce errors for the grain size calculation. Possible research work could be addressed to develop a universal dynamical recrystallization model without an isothermal assumption.

The proposed microstructure sensitive flow stress model is the current thesis is a constitutive model, which correlates the material mechanical behavior with respect to the grain size and phase composition. However, the flow stress model parameters are essentially obtained from the regression analysis given a specific form. The underlying physics why the microstructure would have influenced the material flow stress is not clearly stated. Microscale based material

flow stress model, such as visco-plasticity, dislocation density model, would provide more insight into the physics behind.

The milling process modeling still imposes great challenges due to the complexity of multiple cutter workpiece interactions. The current FEA method utilize the moving mesh window along the tool/workpiece interface area. For the milling process, multiple tool/workpiece interfaces are involved, which make the FEA solution hard to converge. So more efficient FEA modeling and meshing scheme would be required to solve the issue. The residual stress on the workpiece surface after milling is not uniformly distribution as turning. Different tool path would also change the residual stress states after milling. In the current thesis, the analytical model for the milling force prediction is well established, the residual stress model still requires extensive investigation.

The whole thesis is focused on the machining process simulation. The ultimate goal is for the machining process design, which requires an inverse modeling framework given the workpiece material, machining tool and end-product functionality requirements. The physical based inverse modeling for machining process design would leverage a process window instead of a single process parameter. So, statistics-based process model would be required for the inverse model development. Another promising avenue is the machine learning based machining process design method. By taking the extensive machining process data, either from the literature experimental data or predictive modeling data, the process design could be achieved through the enhanced learning scheme.

REFERENCES

1. Ulutan, D. and T. Ozel, *Machining induced surface integrity in titanium and nickel alloys: A review.* International Journal of Machine Tools and Manufacture, 2011. **51**(3): p. 250-280.

2. Pan, Z., et al., *Analytical model for force prediction in laser-assisted milling of IN718.* The International Journal of Advanced Manufacturing Technology, 2017. **90**(9-12): p. 2935-2942.

3. Fergani, O., et al., *Microstructure Texture Prediction in Machining Processes.* Procedia CIRP, 2016. **46**: p. 595-598.

4. Ghosh, S. and V. Kain, *Microstructural changes in AISI 304L stainless steel due to surface machining: Effect on its susceptibility to chloride stress corrosion cracking.* Journal of nuclear materials, 2010. **403**(1): p. 62-67.

5. Barbacki, A., M. Kawalec, and A. Hamrol, *Turning and grinding as a source of microstructural changes in the surface layer of hardened steel.* Journal of materials processing technology, 2003. **133**(1): p. 21-25.

6. Pan, Z., et al., *The effects of dynamic evolution of microstructure on machining forces.* Proceedings of the Institution of Mechanical Engineers, Part B: Journal of Engineering Manufacture. **0**(0): p. 0954405417703430.

7. Xu, H.H. and S. Jahanmir. *Effect of microstructure on abrasive machining of advanced ceramics*. in *A Collection of Papers Presented at the 96th Annual Meeting and the 1994 Fall Meetings of the Materials & Equipment/Whitewares/Refractory Ceramics/Basic Science: Ceramic Engineering and Science Proceedings, Volume 16, Issue 1*. 1995. Wiley Online Library.

8. Chou, Y.K. and C.J. Evans, *White layers and thermal modeling of hard turned surfaces.* International Journal of Machine Tools and Manufacture, 1999. **39**(12): p. 1863-1881.

9. Swaminathan, S., et al., *Severe plastic deformation of copper by machining: Microstructure refinement and nanostructure evolution with strain.* Scripta materialia, 2007. **56**(12): p. 1047-1050.

10. Baufeld, B., O. Van der Biest, and R. Gault, *Additive manufacturing of Ti–6Al–4V components by shaped metal deposition: microstructure and mechanical properties.* Materials & Design, 2010. **31**: p. S106-S111.

11. Baufeld, B., E. Brandl, and O. Van der Biest, *Wire based additive layer manufacturing: comparison of microstructure and mechanical properties of Ti–6Al–4V components fabricated by laser-beam deposition and shaped metal deposition.* Journal of Materials Processing Technology, 2011. **211**(6): p. 1146-1158.

12. Thijs, L., et al., *A study of the microstructural evolution during selective laser melting of Ti–6Al–4V.* Acta Materialia, 2010. **58**(9): p. 3303-3312.

13. Araujo, D., et al., *Microstructural study of CO 2 laser machined heat affected zone of 2024 aluminum alloy.* Applied Surface Science, 2003. **208**: p. 210-217.

14. El-Wardany, T., H. Kishawy, and M. Elbestawi, *Surface integrity of die material in high speed hard machining, Part 1: Micrographical analysis.* Journal of manufacturing science and engineering, 2000. **122**(4): p. 620-631.

15. Popov, K.B., et al., *Micromilling: Material microstructure effects.* Proceedings of the Institution of Mechanical Engineers, Part B: Journal of Engineering Manufacture, 2006. **220**(11): p. 1807-1813.

16. Axinte, D. and R. Dewes, *Surface integrity of hot work tool steel after high speed milling-experimental data and empirical models.* Journal of Materials Processing Technology, 2002. **127**(3): p. 325-335.

17. Griffiths, B., *White layer formations at machined surfaces and their relationship to white layer formations at worn surfaces.* J. Tribology(Trans. ASME), 1985. **107**(2): p. 165-171.

18. Han, S., et al., *White layer formation due to phase transformation in orthogonal machining of AISI 1045 annealed steel.* Materials Science and Engineering: A, 2008. **488**(1): p. 195-204.

19. Barbacki, A. and M. Kawalec, *Structural alterations in the surface layer during hard machining.* Journal of Materials Processing Technology, 1997. **64**(1-3): p. 33-39.

20. Ramesh, A. and S.N. Melkote, *Modeling of white layer formation under thermally dominant conditions in orthogonal machining of hardened AISI 52100 steel.* International Journal of Machine Tools and Manufacture, 2008. **48**(3): p. 402-414.

21. Umbrello, D. and L. Filice, *Improving surface integrity in orthogonal machining of hardened AISI 52100 steel by modeling white and dark layers formation.* CIRP Annals-Manufacturing Technology, 2009. **58**(1): p. 73-76.

22. Poulachon, G., et al., *An experimental investigation of work material microstructure effects on white layer formation in PCBN hard turning.* International Journal of Machine Tools and Manufacture, 2005. **45**(2): p. 211-218.

23. Duan, C., et al., *Modeling of white layer thickness in high speed machining of hardened steel based on phase transformation mechanism.* The International Journal of Advanced Manufacturing Technology, 2013. **69**(1-4): p. 59-70.

24. Barry, J. and G. Byrne, *TEM study on the surface white layer in two turned hardened steels.* Materials Science and Engineering: A, 2002. **325**(1): p. 356-364.

25. Bosheh, S. and P. Mativenga, *White layer formation in hard turning of H13 tool steel at high cutting speeds using CBN tooling.* International Journal of Machine Tools and Manufacture, 2006. **46**(2): p. 225-233.

26. Che-Haron, C. and A. Jawaid, *The effect of machining on surface integrity of titanium alloy Ti–6% Al–4% V.* Journal of Materials Processing Technology, 2005. **166**(2): p. 188-192.

27. Velásquez, J.P., et al., *Sub-surface and surface analysis of high speed machined Ti–6Al–4V alloy.* Materials Science and Engineering: A, 2010. **527**(10): p. 2572-2578.

28. Daymi, A., et al., *Surface integrity in high speed end milling of titanium alloy Ti–6Al–4V.* Materials Science and Technology, 2011. **27**(1): p. 387-394.

29. Ranganath, S., C. Guo, and P. Hegde, *A finite element modeling approach to predicting white layer formation in nickel superalloys.* CIRP Annals-Manufacturing Technology, 2009. **58**(1): p. 77-80.

30. Chou, Y.K. and H. Song, *Thermal modeling for white layer predictions in finish hard turning.* International Journal of Machine Tools and Manufacture, 2005. **45**(4): p. 481-495.

31. Umbrello, D., et al., *Modeling of white and dark layer formation in hard machining of AISI 52100 bearing steel.* Machining Science and Technology, 2010. **14**(1): p. 128-147.

32. Wan, Z., et al., *Microstructure evolution of adiabatic shear bands and mechanisms of saw-tooth chip formation in machining Ti6Al4V.* Materials Science and Engineering: A, 2012. **531**: p. 155-163.

33. Shivpuri, R., et al., *Microstructure-mechanics interactions in modeling chip segmentation during titanium machining.* CIRP Annals-Manufacturing Technology, 2002. **51**(1): p. 71-74.

34. Vogler, M.P., R.E. DeVor, and S.G. Kapoor, *On the modeling and analysis of machining performance in micro-endmilling, Part I: Surface generation.* Journal of Manufacturing Science and Engineering, 2004. **126**(4): p. 685-694.

35. Derep, J., *Microstructure transformation induced by adiabatic shearing in armour steel.* Acta Metallurgica, 1987. **35**(6): p. 1245-1249.

36. Duan, C. and L. Zhang, *Adiabatic shear banding in AISI 1045 steel during high speed machining: mechanisms of microstructural evolution.* Materials Science and Engineering: A, 2012. **532**: p. 111-119.

37. Bayoumi, A. and J. Xie, *Some metallurgical aspects of chip formation in cutting Ti-6wt.% Al-4wt.% V alloy.* Materials Science and Engineering: A, 1995. **190**(1-2): p. 173-180.

38. Velásquez, J.P., et al., *Metallurgical study on chips obtained by high speed machining of a Ti–6wt.% Al–4wt.% V alloy.* Materials Science and Engineering: A, 2007. **452**: p. 469-474.

39. Ye, G., et al., *Modeling periodic adiabatic shear band evolution during high speed machining Ti-6Al-4V alloy.* International journal of plasticity, 2013. **40**: p. 39-55.

40. Campbell, C., et al., *Microstructural characterization of Al-7075-T651 chips and work pieces produced by high-speed machining.* Materials Science and Engineering: A, 2006. **430**(1): p. 15-26.

41. Shankar, M.R., et al., *Characteristics of aluminum 6061-T6 deformed to large plastic strains by machining.* Materials Science and Engineering: A, 2005. **410**: p. 364-368.

42. Yuan, Z., L. Geng, and S. Dong, *Ultraprecision Machining of SiCw/Al Composites11The Project Supported by National Natural Science Foundation of China.* CIRP Annals-Manufacturing Technology, 1993. **42**(1): p. 107-109.

43. Furukawa, Y. and N. Moronuki, *Effect of material properties on ultra precise cutting processes.* CIRP Annals-Manufacturing Technology, 1988. **37**(1): p. 113-116.

44. Chou, Y.K., *Hard turning of M50 steel with different microstructures in continuous and intermittent cutting.* Wear, 2003. **255**(7): p. 1388-1394.

45. DeVor, R., S. Kapoor, and D. Bammann, *Microstructure-level modeling of ductile iron machining.* 2002.

46. DeVor, R.E., *On the modeling and analysis of machining performance in micro-endmilling, Part II: Cutting force prediction.* Urbana, 2004. **51**: p. 61801-2906.

47. Pan, Z., et al., *Modeling of Ti-6Al-4V machining force considering material microstructure evolution.* The International Journal of Advanced Manufacturing Technology, 2017: p. 1-8.

48. Molinari, A., C. Musquar, and G. Sutter, *Adiabatic shear banding in high speed machining of Ti–6Al–4V: experiments and modeling.* International journal of Plasticity, 2002. **18**(4): p. 443-459.

49. Recht, R., *Catastrophic thermoplastic shear.* J. appl. Mech, 1964. **31**(2): p. 186-193.

50. Xu, Y., et al., *Shear localization in dynamic deformation: microstructural evolution.* Metallurgical and materials transactions A, 2008. **39**(4): p. 811.

51. Meyers, M., et al., *Microstructural evolution in adiabatic shear localization in stainless steel.* Acta Materialia, 2003. **51**(5): p. 1307-1325.

52. R. Ebrahimi, E.S., *Mathematical Modeling of Single Peak Dynamic Recrystallization Flow Stress Curves in Metallic Alloys.* Recrystallization, 2012.

53. Guo, Y., Q. Wen, and M. Horstemeyer, *An internal state variable plasticity-based approach to determine dynamic loading history effects on material property in manufacturing processes.* International journal of mechanical sciences, 2005. **47**(9): p. 1423-1441.

54. Calamaz, M., D. Coupard, and F. Girot, *A new material model for 2D numerical simulation of serrated chip formation when machining titanium alloy Ti–6Al–4V.* International Journal of Machine Tools and Manufacture, 2008. **48**(3): p. 275-288.

55. Zhang, X., R. Shivpuri, and A. Srivastava, *Role of phase transformation in chip segmentation during high speed machining of dual phase titanium alloys.* Journal of Materials Processing Technology, 2014. **214**(12): p. 3048-3066.

56. Venkatachalam, S., et al., *Microstructure effects on cutting forces and flow stress in ultra-precision machining of polycrystalline brittle materials.* Journal of Manufacturing Science and Engineering, 2015. **137**(2): p. 021020.

57. Arısoy, Y.M. and T. Özel, *Prediction of machining induced microstructure in Ti–6Al–4V alloy using 3-D FE-based simulations: Effects of tool micro-geometry, coating and cutting conditions.* Journal of Materials Processing Technology, 2015. **220**: p. 1-26.

58. Zhipeng Pan, A.T., Donald S. Shih, Hamid Garmestani, Steven Y. Liang, *The Effects of Dynamic Evolution of Microstructure on Machining Forces.* Proceedings of the Institution of Mechanical Engineers, Part B: Journal of Engineering Manufacture, 2017. DOI:10.1177/0954405417703430.

59. Gourdin, W. and D. Lassila, *Flow stress of OFE copper at strain rates from 10− 3 to 104s− 1: Grain-size effects and comparison to the mechanical threshold stress model.* Acta Metallurgica et Materialia, 1991. **39**(10): p. 2337-2348.

60. Atmani, Z., et al., *Multi-physics modelling in machining OFHC copper–coupling of microstructure-based flow stress and grain refinement models.* Procedia CIRP, 2015. **31**: p. 545-550.

61. Fergani, O. and S.Y. Liang, *Materials-affected manufacturing.* Manufacturing Letters, 2013. **1**(2): p. 74-77.

62. Andrade, U., et al., *Dynamic recrystallization in high-strain, high-strain-rate plastic deformation of copper.* Acta metallurgica et materialia, 1994. **42**(9): p. 3183-3195.

63. Nemat-Nasser, S., et al., *Dynamic response of conventional and hot isostatically pressed Ti–6Al–4V alloys: experiments and modeling.* Mechanics of Materials, 2001. **33**(8): p. 425-439.

64. Zerilli, F.J. and R.W. Armstrong, *Dislocation - mechanics - based constitutive relations for material dynamics calculations.* Journal of Applied Physics, 1987. **61**(5): p. 1816-1825.

65. M'Saoubi, R., et al., *A review of surface integrity in machining and its impact on functional performance and life of machined products.* International Journal of Sustainable Manufacturing, 2008. **1**(1-2): p. 203-236.

66. Devillez, A., et al., *Dry machining of Inconel 718, workpiece surface integrity.* Journal of Materials Processing Technology, 2011. **211**(10): p. 1590-1598.

67. Pawade, R., S.S. Joshi, and P. Brahmankar, *Effect of machining parameters and cutting edge geometry on surface integrity of high-speed turned Inconel 718.* International Journal of Machine Tools and Manufacture, 2008. **48**(1): p. 15-28.

68. Arunachalam, R., M. Mannan, and A. Spowage, *Residual stress and surface roughness when facing age hardened Inconel 718 with CBN and ceramic cutting tools.* International Journal of Machine Tools and Manufacture, 2004. **44**(9): p. 879-887.

69. Sharman, A., J. Hughes, and K. Ridgway, *An analysis of the residual stresses generated in Inconel 718™ when turning.* Journal of Materials Processing Technology, 2006. **173**(3): p. 359-367.

70. Outeiro, J., et al., *Analysis of residual stresses induced by dry turning of difficult-to-machine materials.* CIRP Annals-Manufacturing Technology, 2008. **57**(1): p. 77-80.

71. Thakur, D., B. Ramamoorthy, and L. Vijayaraghavan, *Study on the machinability characteristics of superalloy Inconel 718 during high speed turning.* Materials & Design, 2009. **30**(5): p. 1718-1725.

72. Pawade, R. and S.S. Joshi, *Mechanism of chip formation in high-speed turning of Inconel 718.* Machining Science and Technology, 2011. **15**(1): p. 132-152.

73. Ginting, A. and M. Nouari, *Surface integrity of dry machined titanium alloys.* International Journal of Machine Tools and Manufacture, 2009. **49**(3): p. 325-332.

74. Sun, J. and Y. Guo, *A comprehensive experimental study on surface integrity by end milling Ti–6Al–4V.* Journal of Materials Processing Technology, 2009. **209**(8): p. 4036-4042.

75. Sharman, A., et al., *Workpiece surface integrity considerations when finish turning gamma titanium aluminide.* Wear, 2001. **249**(5): p. 473-481.

76. Mhamdi, M., et al., *Surface integrity of titanium alloy Ti-6Al-4V in ball end milling.* Physics Procedia, 2012. **25**: p. 355-362.

77. Özel, T. and D. Ulutan, *Prediction of machining induced residual stresses in turning of titanium and nickel based alloys with experiments and finite element simulations.* CIRP Annals-Manufacturing Technology, 2012. **61**(1): p. 547-550.

78. Chen, H.-C., A.J. Pinkerton, and L. Li, *Fibre laser welding of dissimilar alloys of Ti-6Al-4V and Inconel 718 for aerospace applications.* The International Journal of Advanced Manufacturing Technology, 2011. **52**(9-12): p. 977-987.

79. Anderson, M., R. Patwa, and Y.C. Shin, *Laser-assisted machining of Inconel 718 with an economic analysis.* International Journal of Machine Tools and Manufacture, 2006. **46**(14): p. 1879-1891.

80. Dudzinski, D., et al., *A review of developments towards dry and high speed machining of Inconel 718 alloy.* International Journal of Machine Tools and Manufacture, 2004. **44**(4): p. 439-456.

81. Sun, S., M. Brandt, and M. Dargusch, *Thermally enhanced machining of hard-to-machine materials—a review.* International Journal of Machine Tools and Manufacture, 2010. **50**(8): p. 663-680.

82. Garcí, V., et al., *Mechanisms involved in the improvement of Inconel 718 machinability by laser assisted machining (LAM).* International journal of machine tools and manufacture, 2013. **74**: p. 19-28.

83. Skvarenina, S. and Y. Shin, *Laser-assisted machining of compacted graphite iron.* International Journal of Machine tools and manufacture, 2006. **46**(1): p. 7-17.

84. Rashid, R.R., et al., *An investigation of cutting forces and cutting temperatures during laser-assisted machining of the Ti–6Cr–5Mo–5V–4Al beta titanium alloy.* International Journal of Machine Tools and Manufacture, 2012. **63**: p. 58-69.

85. Bass, M., D. Beck, and S.M. Copley. *Laser assisted machining*. in *Fourth European Electro-Optics Conference*. 1979. International Society for Optics and Photonics.

86. Chang, C.-W. and C.-P. Kuo, *An investigation of laser-assisted machining of Al 2 O 3 ceramics planing.* International Journal of Machine Tools and Manufacture, 2007. **47**(3): p. 452-461.

87. Ding, H. and Y.C. Shin, *Laser-assisted machining of hardened steel parts with surface integrity analysis.* International Journal of Machine tools and manufacture, 2010. **50**(1): p. 106-114.

88. Niinomi, M., *Mechanical properties of biomedical titanium alloys.* Materials Science and Engineering: A, 1998. **243**(1): p. 231-236.

89. Seshacharyulu, T., et al., *Hot working of commercial Ti–6Al–4V with an equiaxed α–β microstructure: materials modeling considerations.* Materials Science and Engineering: A, 2000. **284**(1): p. 184-194.

90. Majorell, A., S. Srivatsa, and R. Picu, *Mechanical behavior of Ti–6Al–4V at high and moderate temperatures—Part I: Experimental results.* Materials Science and Engineering: A, 2002. **326**(2): p. 297-305.

91. Hong, S.Y., I. Markus, and W.-c. Jeong, *New cooling approach and tool life improvement in cryogenic machining of titanium alloy Ti-6Al-4V.* International Journal of Machine Tools and Manufacture, 2001. **41**(15): p. 2245-2260.

92. Hong, S.Y. and Y. Ding, *Cooling approaches and cutting temperatures in cryogenic machining of Ti-6Al-4V.* International Journal of Machine Tools and Manufacture, 2001. **41**(10): p. 1417-1437.

93. Nalla, R., et al., *On the influence of mechanical surface treatments—deep rolling and laser shock peening—on the fatigue behavior of Ti–6Al–4V at ambient and elevated temperatures.* Materials Science and Engineering: A, 2003. **355**(1): p. 216-230.

94. Zuo, J., Z. Wang, and E. Han, *Effect of microstructure on ultra-high cycle fatigue behavior of Ti–6Al–4V.* Materials Science and Engineering: A, 2008. **473**(1): p. 147-152.

95. Suárez, A., et al., *Modeling of phase transformations of Ti6Al4V during laser metal deposition.* Physics Procedia, 2011. **12**: p. 666-673.

96. Charles, C., *Modelling microstructure evolution of weld deposited Ti-6Al-4V*. 2008: Luleå University of Technology.

97. Malinov, S., W. Sha, and J. McKeown, *Modelling the correlation between processing parameters and properties in titanium alloys using artificial neural network.* Computational materials science, 2001. **21**(3): p. 375-394.

98. Ducato, A., L. Fratini, and F. Micari, *Prediction of phase transformation of Ti-6Al-4V titanium alloy during hot-forging processes using a numerical model.* Proceedings of the Institution of Mechanical Engineers, Part L: Journal of Materials Design and Applications, 2013: p. 1464420713477344.

99. Fanfoni, M. and M. Tomellini, *The Johnson-Mehl-Avrami-Kohnogorov model: A brief review.* Il Nuovo Cimento D, 1998. **20**(7-8): p. 1171-1182.

100. Kugler, G. and R. Turk, *Modeling the dynamic recrystallization under multi-stage hot deformation.* Acta Materialia, 2004. **52**(15): p. 4659-4668.

101. Quan, G.-z., et al., *Modelling for the dynamic recrystallization evolution of Ti–6Al–4V alloy in two-phase temperature range and a wide strain rate range.* Computational Materials Science, 2015. **97**: p. 136-147.

102. Pan, Z., et al., *Prediction of machining-induced phase transformation and grain growth of Ti-6Al-4 V alloy.* The International Journal of Advanced Manufacturing Technology, 2016. **87**(1-4): p. 859-866.

103. Malinov, S., et al., *Differential scanning calorimetry study and computer modeling of $\beta \Rightarrow \alpha$ phase transformation in a Ti-6Al-4V alloy.* Metallurgical and Materials Transactions A, 2001. **32**(4): p. 879-887.

104. Umbrello, D., *Finite element simulation of conventional and high speed machining of Ti6Al4V alloy.* Journal of materials processing technology, 2008. **196**(1): p. 79-87.

105. Pan, Z., et al., *Modeling of Ti-6Al-4V machining force considering material microstructure evolution.* The International Journal of Advanced Manufacturing Technology, 2017. **91**(5-8): p. 2673-2680.

106. Cockcroft, M.G. and D.J. Latham, *A simple criterion of fracture for ductile metals*. 1966.

107. Gente, A., H.-W. Hoffmeister, and C. Evans, *Chip formation in machining Ti6Al4V at extremely high cutting speeds.* CIRP Annals-Manufacturing Technology, 2001. **50**(1): p. 49-52.

108. Balasundar, I., T. Raghu, and B. Kashyap, *Modeling the hot working behavior of near-α titanium alloy IMI 834.* Progress in Natural Science: Materials International, 2013. **23**(6): p. 598-607.

109. Elmer, J., et al., *Phase transformation dynamics during welding of Ti–6Al–4V.* Journal of applied physics, 2004. **95**(12): p. 8327-8339.

110. Liu, X., P.K. Chu, and C. Ding, *Surface modification of titanium, titanium alloys, and related materials for biomedical applications.* Materials Science and Engineering: R: Reports, 2004. **47**(3): p. 49-121.

111. Boyer, R., *An overview on the use of titanium in the aerospace industry.* Materials Science and Engineering: A, 1996. **213**(1): p. 103-114.

112. Leyens, C. and M. Peters, *Titanium and titanium alloys*. 2003: Wiley Online Library.

113. Ezugwu, E. and Z. Wang, *Titanium alloys and their machinability—a review.* Journal of materials processing technology, 1997. **68**(3): p. 262-274.

114. Arrazola, P.-J., et al., *Machinability of titanium alloys (Ti6Al4V and Ti555. 3).* Journal of Materials Processing Technology, 2009. **209**(5): p. 2223-2230.

115. Zhang, D.-N., et al., *A modified Johnson–Cook model of dynamic tensile behaviors for 7075-t6 aluminum alloy.* Journal of Alloys and Compounds, 2015. **619**: p. 186-194.

116. Huang, Y. and S.Y. Liang, *Force modelling in shallow cuts with large negative rake angle and large nose radius tools—application to hard turning.* The International Journal of Advanced Manufacturing Technology, 2003. **22**(9-10): p. 626-632.

117. Umbrello, D., J. Hua, and R. Shivpuri, *Hardness-based flow stress and fracture models for numerical simulation of hard machining AISI 52100 bearing steel.* Materials Science and Engineering: A, 2004. **374**(1): p. 90-100.

118. Seward, G., et al., *In situ SEM-EBSD observations of the hcp to bcc phase transformation in commercially pure titanium.* Acta Materialia, 2004. **52**(4): p. 821-832.

119. Lee, W.-S. and C.-F. Lin, *Plastic deformation and fracture behaviour of Ti–6Al–4V alloy loaded with high strain rate under various temperatures.* Materials Science and Engineering: A, 1998. **241**(1): p. 48-59.

120. Andrade, U., M. Meyers, and A. Chokshi, *Constitutive description of work-and shock-hardened copper.* Scripta metallurgica et materialia, 1994. **30**(7): p. 933-938.

121. Asaro, R.J., *Crystal plasticity.* Journal of applied mechanics, 1983. **50**(4b): p. 921-934.

122. Hill, R., *A self-consistent mechanics of composite materials.* Journal of the Mechanics and Physics of Solids, 1965. **13**(4): p. 213-222.

123. Sima, M. and T. Özel, *Modified material constitutive models for serrated chip formation simulations and experimental validation in machining of titanium alloy Ti–6Al–4V.* International Journal of Machine Tools and Manufacture, 2010. **50**(11): p. 943-960.

124. Picu, R. and A. Majorell, *Mechanical behavior of Ti–6Al–4V at high and moderate temperatures—Part II: constitutive modeling.* Materials Science and Engineering: A, 2002. **326**(2): p. 306-316.

125. Xueping Zhang, R.S., Anil K. Srivastava, *Microstructure sensitive flow stress based on self consistent method.* Proceedings of the ASME 2016 International Manufacturing Science and Engineering Conference, 2016.

126. Tansel, I., et al., *Tool wear estimation in micro-machining.: Part I: tool usage–cutting force relationship.* International Journal of Machine Tools and Manufacture, 2000. **40**(4): p. 599-608.

127. Barry, J. and G. Byrne, *Cutting tool wear in the machining of hardened steels: Part I: Alumina/TiC cutting tool wear.* Wear, 2001. **247**(2): p. 139-151.

128. Kumar, K.K. and S. Choudhury, *Investigation of tool wear and cutting force in cryogenic machining using design of experiments.* Journal of Materials Processing Technology, 2008. **203**(1): p. 95-101.

129. Saffar, R.J., et al., *Simulation of three-dimension cutting force and tool deflection in the end milling operation based on finite element method.* Simulation Modelling Practice and Theory, 2008. **16**(10): p. 1677-1688.

130. Pan, Z., et al., *Analytical model for force prediction in laser-assisted milling of IN718.* The International Journal of Advanced Manufacturing Technology, 2016: p. 1-8.

131. Strenkowski, J.S. and J. Carroll, *A finite element model of orthogonal metal cutting.* Journal of Engineering for Industry, 1985. **107**(4): p. 349-354.

132. Shao, Y., et al., *Physics-based analysis of minimum quantity lubrication grinding.* The International Journal of Advanced Manufacturing Technology, 2015. **79**(9-12): p. 1659-1670.

133. Shao, Y., et al., *Residual stress modeling in minimum quantity lubrication grinding.* The International Journal of Advanced Manufacturing Technology, 2016. **83**(5-8): p. 743-751.

134. Semiatin, S. and T. Bieler, *The effect of alpha platelet thickness on plastic flow during hot working of Ti–6Al–4V with a transformed microstructure.* Acta materialia, 2001. **49**(17): p. 3565-3573.

135. Shell, E. and S. Semiatin, *Effect of initial microstructure on plastic flow and dynamic globularization during hot working of Ti-6Al-4V.* Metallurgical and Materials Transactions A, 1999. **30**(12): p. 3219-3229.

136. Su, J.-C., *Residual stress modeling in machining processes.* 2006.

137. Komanduri, R. and B. Von Turkovich, *New observations on the mechanism of chip formation when machining titanium alloys.* Wear, 1981. **69**(2): p. 179-188.

138. Jaffery, S.H.I. and P.T. Mativenga, *Wear mechanisms analysis for turning Ti-6Al-4V—towards the development of suitable tool coatings.* The International Journal of Advanced Manufacturing Technology, 2012. **58**(5-8): p. 479-493.

139. Sun, S., M. Brandt, and M. Dargusch, *Characteristics of cutting forces and chip formation in machining of titanium alloys.* International Journal of Machine Tools and Manufacture, 2009. **49**(7): p. 561-568.

140. Masumura, R., P. Hazzledine, and C. Pande, *Yield stress of fine grained materials.* Acta Materialia, 1998. **46**(13): p. 4527-4534.

141. Jaffery, S.H.I., et al., *Statistical analysis of process parameters in micromachining of Ti-6Al-4V alloy.* Proceedings of the Institution of Mechanical Engineers, Part B: Journal of Engineering Manufacture, 2016. **230**(6): p. 1017-1034.

142. Javidi, A., U. Rieger, and W. Eichlseder, *The effect of machining on the surface integrity and fatigue life.* International Journal of fatigue, 2008. **30**(10): p. 2050-2055.

143. Saı, W.B., N.B. Salah, and J. Lebrun, *Influence of machining by finishing milling on surface characteristics.* International Journal of Machine Tools and Manufacture, 2001. **41**(3): p. 443-450.

144. Wagner, L., *Mechanical surface treatments on titanium, aluminum and magnesium alloys.* Materials Science and Engineering: A, 1999. **263**(2): p. 210-216.

145. Ji, X. and S.Y. Liang, *Model-based sensitivity analysis of machining-induced residual stress under minimum quantity lubrication.* Proceedings of the Institution of Mechanical Engineers, Part B: Journal of Engineering Manufacture. **0**(0): p. 0954405415601802.

146. Yue, C., et al., *Off-line error compensation in corner milling process.* Proceedings of the Institution of Mechanical Engineers, Part B: Journal of Engineering Manufacture, 2016: p. 0954405416666901.

147. Liu, C. and M. Barash, *Variables governing patterns of mechanical residual stress in a machined surface.* Journal of Engineering for Industry, 1982. **104**(3): p. 257-264.

148. Henriksen, E.K. *Residual stresses in machined surfaces*. 1948. ASME.

149. Okushima, K. and Y. Kakino, *Study of the Residual Stress Produced by Metal Cutting.* Mem. Fac. Eng. Kyoto Univ., 1972. **34**(2): p. 234-248.

150. Jang, D., et al., *Surface residual stresses in machined austenitic stainless steel.* Wear, 1996. **194**(1): p. 168-173.

151. Matsumoto, Y., M. Barash, and C. Liu, *Effect of hardness on the surface integrity of AISI 4340 steel.* Journal of Engineering for Industry, 1986. **108**(3): p. 169-175.

152. Hughes, J., A. Sharman, and K. Ridgway, *The effect of tool edge preparation on tool life and workpiece surface integrity.* Proceedings of the Institution of Mechanical Engineers, Part B: Journal of Engineering Manufacture, 2004. **218**(9): p. 1113-1123.

153. Song, H.-W., S.-H. Zhang, and M. Cheng, *Dynamic globularization kinetics during hot working of a two phase titanium alloy with a colony alpha microstructure.* Journal of Alloys and Compounds, 2009. **480**(2): p. 922-927.

154. Komanduri, R. and Z.B. Hou, *Thermal modeling of the metal cutting process: Part I—Temperature rise distribution due to shear plane heat source.* International Journal of Mechanical Sciences, 2000. **42**(9): p. 1715-1752.

155. Waldorf, D.J., R.E. DeVor, and S.G. Kapoor, *A slip-line field for ploughing during orthogonal cutting.* Journal of Manufacturing Science and Engineering, 1998. **120**(4): p. 693-699.

156. Waldorf, D.J., *A simplified model for ploughing forces in turning.* Journal of manufacturing processes, 2006. **8**(2): p. 76-82.

157. Lin, Z.-C., Y.-Y. Lin, and C. Liu, *Effect of thermal load and mechanical load on the residual stress of a machined workpiece.* International Journal of Mechanical Sciences, 1991. **33**(4): p. 263-278.

158. McDowell, D., *An approximate algorithm for elastic-plastic two-dimensional rolling/sliding contact.* Wear, 1997. **211**(2): p. 237-246.

159. Ratchev, S., et al., *Mathematical modelling and integration of micro-scale residual stresses into axisymmetric FE models of Ti6Al4V alloy in turning.* CIRP Journal of Manufacturing Science and Technology, 2011. **4**(1): p. 80-89.

160. Rahman, M., Z.-G. Wang, and Y.-S. Wong, *A review on high-speed machining of titanium alloys.* JSME International Journal Series C Mechanical Systems, Machine Elements and Manufacturing, 2006. **49**(1): p. 11-20.

161. Pan, Z., et al., *Prediction of machining-induced phase transformation and grain growth of Ti-6Al-4 V alloy.* The International Journal of Advanced Manufacturing Technology, 2016. **87**(1): p. 859-866.

162. Pan, Z., et al., *Microstructure-sensitive flow stress modeling for force prediction in laser assisted milling of Inconel 718.* Manufacturing Review, 2017. **4**: p. 6.

163. Pan, Z., Y. Feng, and S.Y. Liang, *Material microstructure affected machining: a review.* Manufacturing Review, 2017. **4**: p. 5.

164. Altin, A., M. Nalbant, and A. Taskesen, *The effects of cutting speed on tool wear and tool life when machining Inconel 718 with ceramic tools.* Materials & design, 2007. **28**(9): p. 2518-2522.

165. Lorentzon, J. and N. Järvstråt, *Modelling tool wear in cemented-carbide machining alloy 718.* International Journal of Machine Tools and Manufacture, 2008. **48**(10): p. 1072-1080.

166. Kuppan, P., A. Rajadurai, and S. Narayanan, *Influence of EDM process parameters in deep hole drilling of Inconel 718.* The International Journal of Advanced Manufacturing Technology, 2008. **38**(1-2): p. 74-84.

167. Jeelani, S. and M. Collins, *Effect of electric discharge machining on the fatigue life of Inconel 718.* International journal of fatigue, 1988. **10**(2): p. 121-125.

168. Wang, Z., et al., *Hybrid machining of Inconel 718.* International Journal of Machine Tools and Manufacture, 2003. **43**(13): p. 1391-1396.

169. Courbon, C., et al., *Investigation of machining performance in high-pressure jet assisted turning of Inconel 718: an experimental study.* International Journal of Machine Tools and Manufacture, 2009. **49**(14): p. 1114-1125.

170. Pan, Z., et al., *Force modeling of Inconel 718 laser-assisted end milling under recrystallization effects.* The International Journal of Advanced Manufacturing Technology, 2017.

171. Pan, Z., et al., *Analytical model for force prediction in laser-assisted milling of IN718.* The International Journal of Advanced Manufacturing Technology, 2017. **90**(9): p. 2935-2942.

172. Chryssolouris, G., N. Anifantis, and S. Karagiannis, *Laser assisted machining: an overview.* Journal of manufacturing science and engineering, 1997. **119**(4B): p. 766-769.

173. Smurov, I.Y. and L. Okorokov, *Laser assisted machining*, in *Laser Applications for Mechanical Industry*. 1993, Springer. p. 151-163.

174. Rozzi, J.C., et al., *Experimental evaluation of the laser assisted machining of silicon nitride ceramics.* Journal of Manufacturing Science and Engineering, 2000. **122**(4): p. 666-670.

175. Chang, C.-W. and C.-P. Kuo, *Evaluation of surface roughness in laser-assisted machining of aluminum oxide ceramics with Taguchi method.* International Journal of Machine Tools and Manufacture, 2007. **47**(1): p. 141-147.

176. Tian, Y. and Y.C. Shin, *Thermal modeling for laser-assisted machining of silicon nitride ceramics with complex features.* Journal of manufacturing science and engineering, 2006. **128**(2): p. 425-434.

177. Rozzi, J.C., et al., *Transient, three-dimensional heat transfer model for the laser assisted machining of silicon nitride: I. Comparison of predictions with measured surface temperature histories.* International Journal of Heat and Mass Transfer, 2000. **43**(8): p. 1409-1424.

178. Kamnis, S., S. Gu, and N. Zeoli, *Mathematical modelling of Inconel 718 particles in HVOF thermal spraying.* Surface and Coatings Technology, 2008. **202**(12): p. 2715-2724.

179. Yang, J., et al., *Experimental investigation and 3D finite element prediction of the heat affected zone during laser assisted machining of Ti6Al4V alloy.* Journal of Materials Processing Technology, 2010. **210**(15): p. 2215-2222.

180. Ricciardi, G. and M. Cantello, *Laser material interaction: absorption coefficient in welding and surface treatment.* CIRP Annals-Manufacturing Technology, 1994. **43**(1): p. 171-175.

181. Pfefferkorn, F.E., et al., *A metric for defining the energy efficiency of thermally assisted machining.* International Journal of Machine Tools and Manufacture, 2009. **49**(5): p. 357-365.

182. Sainte-Catherine, C., et al., *STUDY OF DYNAMIC ABSORPTIVITY AT 10.6 ĩm (CO2) AND 1.06 ĩm (Nd-YAG) WAVELENGTHS AS A FUNCTION OF TEMPERATURE.* Le Journal de Physique IV, 1991. **1**(C7): p. C7-151-C7-157.

183. Brecher, C., et al., *Laser-assisted milling of advanced materials.* Physics Procedia, 2011. **12**: p. 599-606.

184. Oxley, P.L.B. and H. Young, *The mechanics of machining: an analytical approach to assessing machinability.* Ellis Horwood Publisher, 1989: p. 136-182.

185. Su, J.-C., et al., *Modeling of residual stresses in milling.* The International Journal of Advanced Manufacturing Technology, 2013. **65**(5-8): p. 717-733.